Università degli Studi del Piemonte Orientale "Amedeo Avogadro"

Dipartimento di Scienze e Innovazione Tecnologica

Corso di Dottorato di Ricerca in Chemistry & Biology
XXX ciclo a.a. 2016-2017
SSD: CHIM02

Hybrid Organic-Inorganic Materials for CO_2 Capture and Utilization

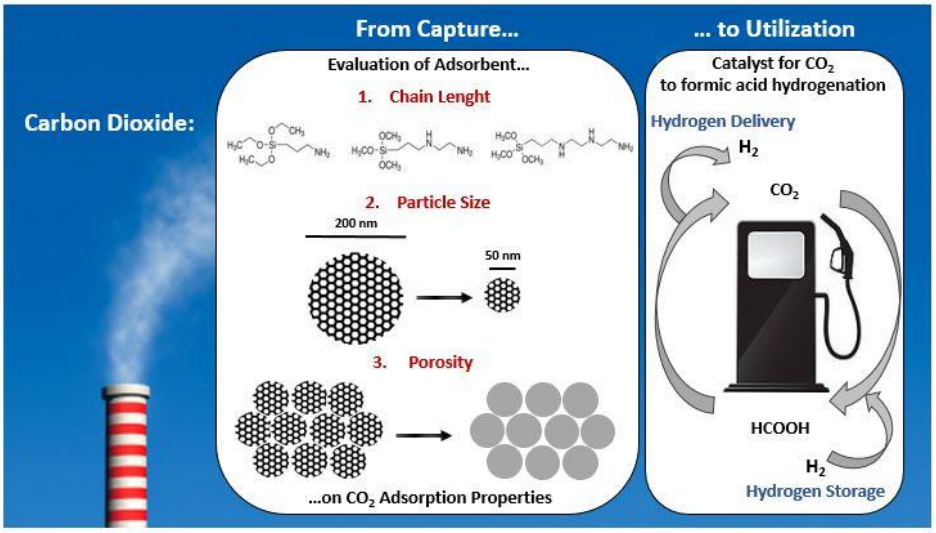

Chiara Vittoni

Supervisor: Prof. Leonardo Marchese

Co-Supervisor: Dr. Chiara Bisio

PhD program coordinator: Prof. Luigi Panza

Università degli Studi del Piemonte Orientale "Amedeo Avogadro"

Dipartimento di Scienze e Innovazione Tecnologica

Corso di Dottorato di Ricerca in Chemistry & Biology
XXX ciclo a.a. 2016-2017
SSD: CHIM02

Hybrid Organic-Inorganic Materials for CO_2 Capture and Utilization

Chiara Vittoni

Supervisor: Prof. Leonardo Marchese

Co-Supervisor: Dr. Chiara Bisio

PhD program coordinator: Prof. Luigi Panza

To Lorenzo,
Thanks for always being by my side.

Contents

Chapter 1

Introduction

In this chapter, the main problems related to environmental pollution caused by carbon dioxide and other greenhouse gases will be discussed. Afterwards, some interesting technologies for the reduction of the CO_2 atmospheric concentration, with particular reference to capture methods, will be treated. In the latter context, particular attention will be given to the most effective solid sorbents for the carbon dioxide capture.

1.1 The Climate Change

1.1.1 Evidences of Climate Changes

The increase of ocean, land and air average temperatures, the melting of glaciers and the rising of the average sea level clearly indicate that a global warming of the climate system is occurring. [1]

All the global temperature reconstructions indicate that Earth has warmed. [2] Each of the last three decades has been progressively warmer than any preceding decade since 1850. In particular, in the last three decades, 15 of the 16 warmest years are since 2001 (with the exception of 1998). *Inter alia*, 2016 holds the record of the warmest year (Figure 1.1, frame A).[3] As far as air heating is concerned, according to satellite temperature measurement, the mean temperature of the troposphere has increased between 0.120 and 0.135 °C per decade since 1979. In February 2017, the mean temperature of land and ocean surfaces was 13.08 °C (*i.e.* 0.98°C above the 20th century average of 12.10°C). This is the second highest temperature recorded in February in the last 138 years, next to the record of +1.20°C set in 2016. The land

and ocean temperature has increased with a mean rate of +0.07°C per decade since 1880; however, starting from 1980, the average rate has doubled. [2]

Oceans represent an important fraction of energy storage due to the global warming: more than 90% of the energy accumulated between 1971 and 2010 is stored in the oceans, while only about 1% is in the atmosphere. The temperature increase owing to this energy supply is however partially tempered due to the high heat capacity of the oceans and the great amount of heat lost by evaporation. Consequently these effects, the top 700 meters of ocean shows a temperature increase of 0.54°C since 1969. [4] As a consequence of the increase in temperatures, snow and ice are melting. For example, the minimum annual value of Arctic sea ice (reached in September) is declining from 7.83 to 4.72 million square kilometres, with a minimum 3.62 occurred in 2012 (Figure 1.1, frame B). In 2017, the maximum annual value (reached in March) of the Arctic sea ice has been 14.42 million square kilometres, the lowest value in the last 38 years. This year's maximum extent is 1220000 km^2 below the 1981-2010 average maximum of 15640000 km^2. [5]

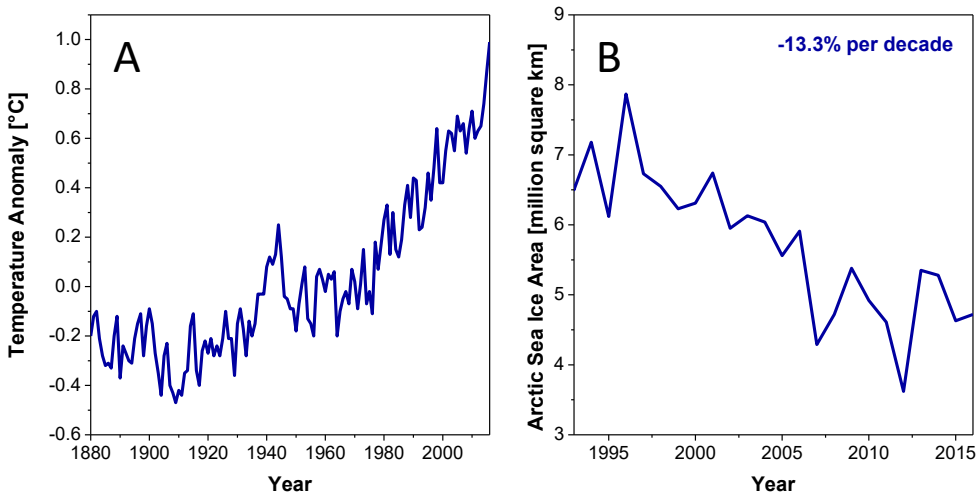

Figure 1.1. Frame A: Temperature anomaly values over global land and oceans surfaces from 1880 to 2016. Data source: NASA's Goddard Institute for Space Studies (GISS). Frame B: Decreasing of Arctic sea ice area from 1993 to 2016 obtained with satellite observations. Data source: Credit: NSIDC/NASA. [3]

Also land ice sheets are losing mass. For example, Antarctica has been losing about 118 gigatonnes of ice per year since 2002, while Greenland has been losing 281 gigatonnes per year. [3]

Another important consequence of the increasing of global temperature is the rise in sea level. In the last century, global sea level rose about 17 cm. However, in the last decade the increasing rate is nearly double that of the previous ones. [6] In particular, from 1993 to 2017, the sea level is increased by 88.2 mm, with a mean increasing rate of 3.4 mm per year (Figure 1.2). [3].

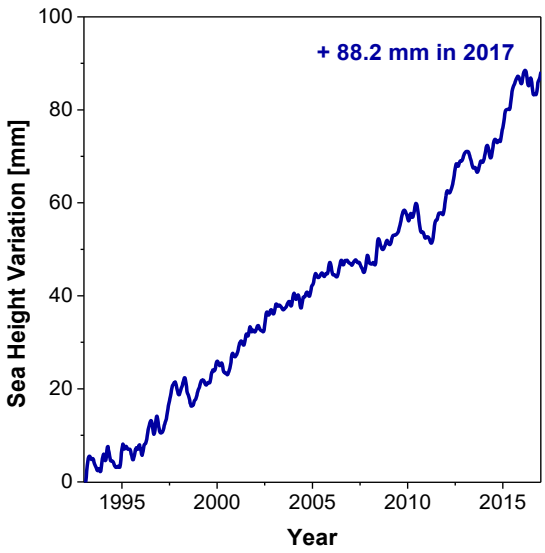

Figure 1.2. Satellite sea level observations. Data are obtained from NASA Goddard Space Flight Centre. [3]

The climate change is also connected to extreme weather events. All over the world, in the last several decades have been changes in some types of extreme weather events. For example, more intense and frequent heat waves and less frequent and intense cold waves, along with an increase in phenomena as extreme rainfall, floods, droughts and wildfires, hurricanes and tornadoes have occurred. [7,8]

For example, 101 tropical cyclones took place across all ocean basins in 2015, far above the 1981-2010 average of 82 storms. [2]

Furthermore, other effects due to climate change are occurring. In many regions, changing in precipitation and melting of snow and ice are affecting hydrological systems, altering quantity and quality of water resources. In addition, many terrestrial and aquatic species have moved their geographic areas, migration patterns and seasonal activities due to the ongoing climate change.

A further climate change will enhance existing effects and create new risks for humanity and environment. Increasing the global warming, negative and irreversible impacts for ecosystems, species and people will happen. For example:

i. risk of food and water insecurity, particularly for poorer populations
ii. risk of severe diseases due to the climate changes
iii. risk of loss of ecosystems and biodiversity (possible extinction of some species)
iv. risks connected to extreme weather events.

1.1.2 Potential Causes of Climate Changes: the Greenhouse Effect

Earth's temperature depends on the balance between the entering energy supplied by sunlight and the energy leaving to space. The solar energy irradiating the Earth (*i.e.* UV-Vis-near IR radiations) has an irradiance of about 342 W/m^2, by averaging over the entire planet, day and night, all year long. Part of this radiation is reflected by the atmosphere and clouds, and a part reaches the Earth's surface, with an irradiance of 198 W/m^2. Excluding a part of the energy reflected from the surface of the Earth, the remaining energy (168 W/m^2) is absorbed by the land and the oceans. This radiation is converted to heat energy, and then a portion is emitted at longer wavelengths respect to the adsorbed ones (*i.e.* in the infrared range). [9] This behaviour is explained by the Wien's law, stating that the radiation curve of a black body has a maximum peak at wavelength inversely proportional to the temperature. Considering that the Earth's surface is colder than the photosphere of the Sun, it radiates at wavelengths

longer than the absorbed ones. This infrared radiation are responsible to the warming of the Earth' surface. However, on this basis, the Earth's average temperature would be near -18°C, while in reality the actual Earth's average temperature is 15 °C. The difference between these two temperatures is due to an effect known as greenhouse effect. Part of the generated infrared radiation is emitted to the atmosphere: a portion of this radiation is directly emitted into the space, and a portion is adsorbed by some radiative gases present in atmosphere, named "greenhouse gases". Then the radiation is re-emitted in all directions including the Earth surface, warming it. This phenomenon allows the planet Earth to reach 15°C, enabling to sustain life. [9]

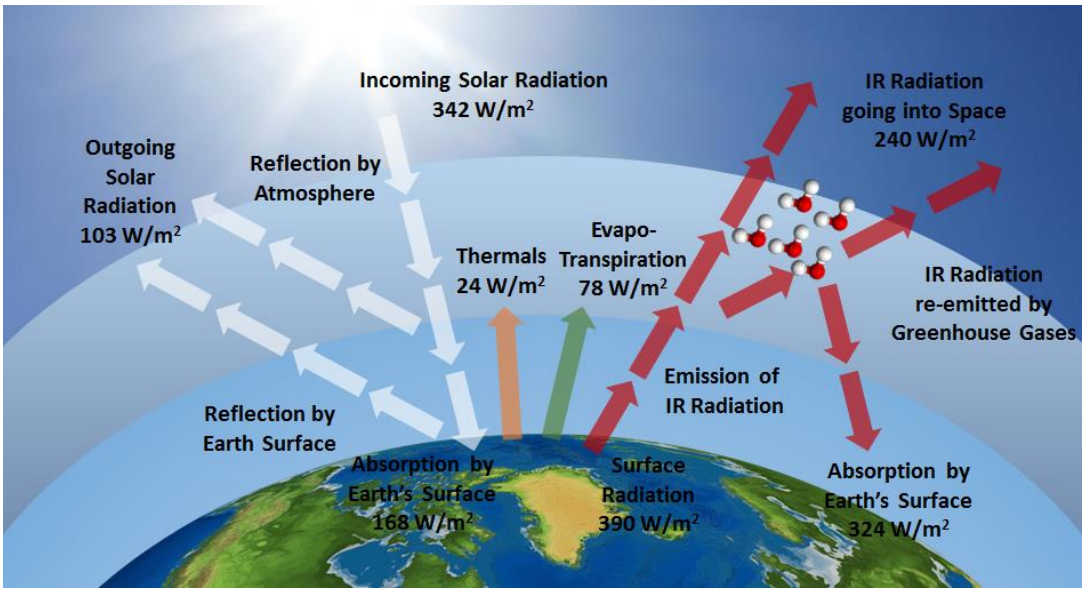

Figure 1.3. Schematic Representation of Greenhouse Effect.

Many greenhouse gases (GHGs), such as carbon dioxide (CO_2), methane (CH_4), nitrous oxide (N_2O), water vapour (H_2O) and ozone (O_3), naturally occur in the atmosphere while others are synthetic, such as chlorofluorocarbons (CFCs), perfluorocarbons (PFCs), hydrofluorocarbons (HFCs) and sulphur hexafluoride (SF_6). The concentrations of both natural and synthetic gases in the atmosphere have been increasing in the last centuries, mainly due to human activities such as burning of fossil fuels (*i.e.* coal, oil and natural gas), deforestation, farming and industrial waste, ever increasing due to the population growth. [10] Actually, the concentrations of GHGs in the atmosphere are at levels never reached in at least 800000 years. In particular, concentrations of CO_2, CH_4 and N_2O are increased since 1750 of 40%, 150% and 20%, respectively. Increasing the concentration of the greenhouse gases, the amount of radiation absorbed and re-emitted increases, and therefore further warms the Earth's surface. This progressive increasing of the Earth's temperature can lead to the effects described in prior paragraph such as desertification, melting of glaciers, rising of the average sea level and extreme weather events, causing irreversible damage to the entire ecosystem. The contribution of each gas to the greenhouse effect is mainly determined by the radiative effect, the abundance, and other indirect effects such as the ability to promote the formation of other greenhouse gases. Taking into account all these variables, water vapour was found the dominant contributor (*ca.* 50% of the effect), followed by clouds (*ca.* 25%) and then carbon dioxide with about 20%. Other greenhouse gases accounting for the remaining 5%. [10] The global radiative forces (*i.e.* the power change per unit area caused by the specific gas) for the main greenhouse gases are reported in Figure 1.4.

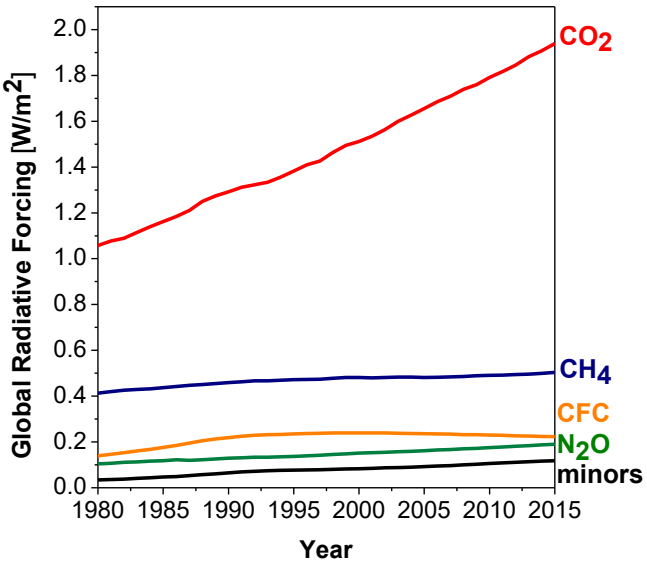

Figure 1.4. Global Radiative Forcing for CO_2, CH_4, CFCs, N_2O and other 15 minor greenhouse gases (CFC-113, CCl_4, CH_3CCl_3, HCFCs 22, 141b and 142b, HFCs 134a, 152a, 23, 143a, and 125, SF_6, and halons 1211, 1301 and 2402). [10]

Carbon dioxide and methane contribute to most of the total radiative forcing, while CFCs are smaller contributors. The four principal greenhouse gases contribute to the 96% of the total direct radiative forcing; the remaining 4% is due to the contribute of the 15 minor halogenated gases. [11]

Another important aspect that merits consideration to determine the danger of a greenhouse gas is the permanence in atmosphere. For example, halocarbons have a low atmospheric concentration, but have an atmospheric lifespan up to 400 years.

1.1.3 Actions to Deal with Climate Change

The first scientific data on the increase of CO_2 atmospheric concentration date back to 1957,[12] but only 31 years later the problem has been considered by the United Nations, with the creation of a special organization, the International Panel on Climate Change (IPCC, winner of the Nobel for Peace in 2007). In 1992, at the United Nations Conference on Environment and Development (UNCED) occurred in Rio de Janeiro, IPCC has produced an agreement (United Nations Framework Convention on Climate Change) with the purpose of "stabilize greenhouse gas concentrations in the atmosphere at a level that would prevent dangerous anthropogenic interference with the climate system". [13] This protocol was later modified and approved in Kyoto in 1997. This document compels its participants to set mandatory targets for emission reductions. Since developed countries are the main responsible of the present worrying levels of greenhouse gases emissions in the atmosphere, the protocol puts more constraints to developed nations following the principle of "common but differentiated responsibilities."[14] However, this agreement has been blocked for a long time due to the refusal to ratify the protocol form United States and Russia. Then it was implemented after the ratification by Russia in 2004. During the first commitment period (until 2012), 37 industrialized nations and the European Community agree to reduce GHGs emissions to 5% against the levels achieved in 1990. During the second commitment period (2013-2020), regulated by Doha amendment, the participant nations agree to reduce greenhouse gases emissions by at least 18% below the standard level reached in 1990 (20 % for the European Union countries). In particular, the concentration of carbon dioxide must be kept below 450 ppm.

In Figure 1.5 are reported the current progress of EU member states, compared to 2005 emission values, toward targets fixed from the European Commission in the so-called Effort Sharing Decision (ESD). This proposal indicated mandatory annual GHGs emission targets for the period 2013–2020, in order to respect Kyoto protocol.

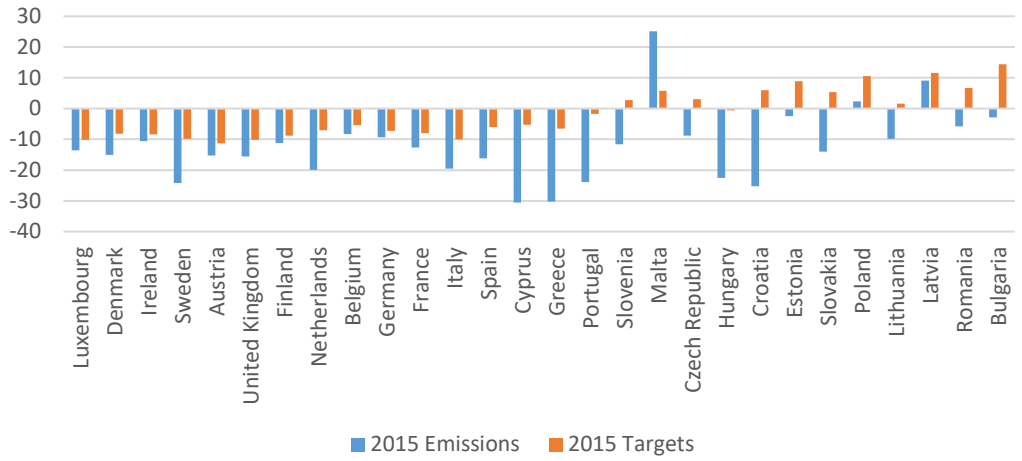

Figure 1.5. Current progress of EU Member States towards their ESD targets. The percentage of change is compared to 2005 base year emissions. [15]

The Kyoto Protocol is an important first step for the reduction of greenhouse emissions and can lay the foundations for future international agreements on climate change. However, the Kyoto Protocol presents some critical issues. First of all, it requires only the intervention of developed countries. In addition, since the United States (*i.e.* the country with the highest CO_2 emissions) has never acceded to the Kyoto Protocol, Canada has withdrawn before the end of the first period and Russia, Japan and New Zealand do not participate to the second period, this agreement is currently applicable to only about 14% of world emissions. [16] With regard to future prospects, at the UN Climate Change Conference (COP21) occurred in Paris in 2015, the delegations of 196 nations adopted a new global climate change agreement, which should come into effect in 2020. The main bullet points of this agreement are: i) the temperature increase must be kept below 2 °C, ii) nations with more polluting emissions (including China and India) must participate to the agreement, iii) a review of the objectives must be carried out every five years, iv) industrialized countries must spread around the world green technologies and decarbonize the economy, and v) repayments to offset the financial losses caused by climate change in the most vulnerable countries are provided. [17]

1.2 Carbon Dioxide

Carbon dioxide is an important greenhouse gas, naturally present in the atmosphere as part of the Earth's carbon cycle. In fact, it is released through natural processes, such as plant and animal respiration and volcanic eruptions. Human activities are influencing the natural carbon cycle both for the addition of more CO_2 to the atmosphere and for the alteration of the plants ability to remove CO_2 from the atmosphere (deforestation). These activities has increased the carbon emissions and thus the CO_2 atmospheric concentration since the mid of 1700, because of the industrial revolution. Global CO_2 emissions from fossil-fuel burning, gas flaring and cement manufacture from 1751 to 2014 are reported in Figure 1.6 A. In 2014, the total amount of carbon dioxide emitted reached 9855 million tons. [18] These emissions have a direct influence on the carbon dioxide concentration in atmosphere. Before the industrial revolution, the CO_2 concentration in atmosphere were about 280 ppm. Today, it is around 407 ppm, with an increase of about 45%. Moreover, the CO_2 growth rate is rapidly increasing: in the1959-1964 period the growth rate was 0.73 ppm/year, while in the 2005-2014 period was 2.11 ppm/year. In Figure 1.6 B is reported the trend of the CO_2 concentration in atmosphere since 1960. [2]

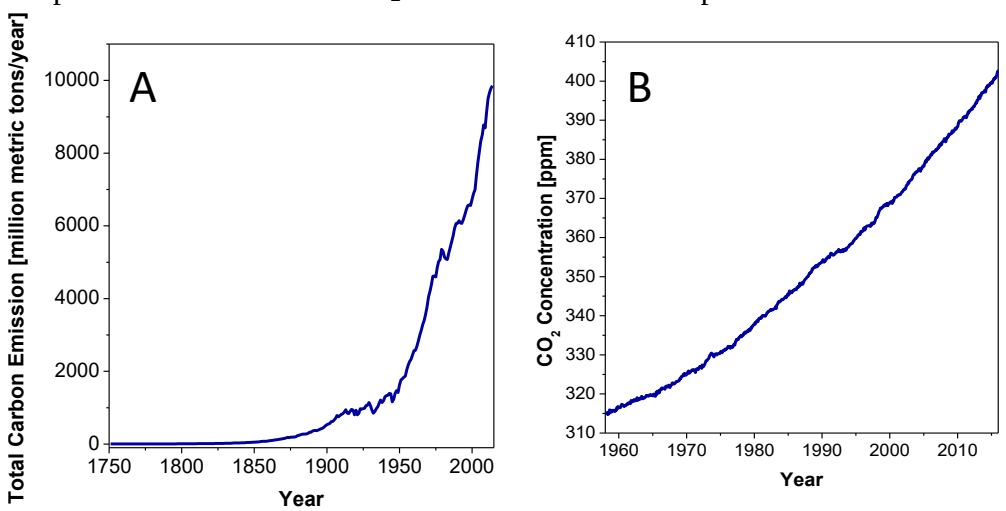

Figure 1.6. Frame A: total carbon emission from 1750. [11] Frame B: CO_2 levels without average seasonal cycle. [2]

In this scenario, the main source of CO_2 emissions is represented by fossil fuels (natural gas, coal and oil) for energy production and transportation, even if some industrial processes also emit CO_2. The principal sources of carbon dioxide emissions are reported in Figure 1.7.

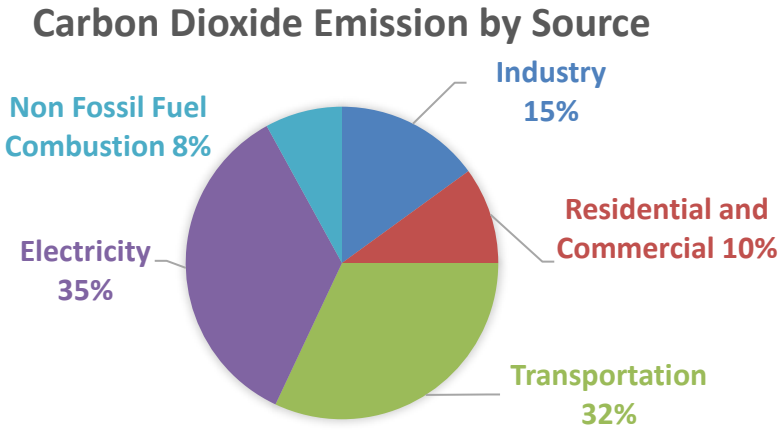

Figure 1.7. 2015 US Carbon Dioxide emission by source. [8]

In 2015, the main source of CO_2 emissions in the United States was the combustion of fossil fuels to produce electricity, accounting for *ca*. 35% of total CO_2 emissions (29% of total US GHGs emissions). For this reason, fossil fuel burning power plants are the main targets of the carbon dioxide reductions. The second main source was related to the combustion of gasoline and diesel for transportation (32% of total United States CO_2 emissions). In addition, various industrial processes emit carbon dioxide both through the combustion of fossil and chemical reactions that do not involve combustion (*i.e.* cement, iron, steel and chemicals production). [8]

Such increase of CO_2 atmospheric concentration has a direct effect on the global warming, as previously described in the Paragraph 1.1. In addition to global warming, ocean acidification is another indirect result of the carbon dioxide emission into the atmosphere. Approximately one third of the carbon dioxide emitted to the atmosphere by anthropogenic activities has been absorbed by the oceans. Without

this absorption, the CO_2 content in atmosphere and consequently the global warming would have been much higher. Once dissolved in oceans, CO_2 can be consumed by photosynthesis and other processes, or can dissolve, generating dramatic changes in sea water chemistry. In particular, CO_2 can react with water molecules forming carbonic acid (H_2CO_3), acidifying the oceans. The average pH of oceanic water is about 8.1 (*ca.*0.1 pH units lower compared to the estimated value of pre-industrial era). [19]

Theoretical calculations have shown that if carbon dioxide continues to be emitted at the actual rate, ocean average pH will achieve 7.8 units by 2100. Oceanic ecosystems may not be able to adapt in time to these rapid changes. Moreover, the dissolution of CO_2 in water cause a decrease in the carbonate ion (CO_3^{2-}). Many marine organisms (*i.e.* molluscs, corals and shellfish) employ CO_3^{2-} ions to form their skeletons or shells. Therefore, the reduction of carbonate ions in the oceanic water can be fatal, as it would decrease the population of organisms fundamental for the food chain and the formation of different habitats, preserving the biodiversity. [19]

1.3 Strategies for the Reduction of Carbon Dioxide Emissions in Atmosphere: Carbon Capture and Storage Methods

The reduction of carbon dioxide emissions, regulated by numerous protocols briefly summarized in the preceding paragraphs, are realized through different strategies, such conservation of energy demand, efficiency improvement, and increasing in the contribution of nuclear and renewable energy. In addition, another way to reduce the CO_2 atmospheric concentration is the Carbon Capture and Storage (CCS). This acronym refers to numerous technologies in which CO_2 capture occurs from power generation, gasification or other industrial processes in which CO_2 is produced (*i.e.* iron and steel production, cement manufacture and natural gas treatment). CCS represents the most promising approach for the long-term emissions reduction of

carbon dioxide. After the capture procedure, CO_2 is then pressurised to about 100 bar, before being transferred to a storage site (usually via pipeline). Here it is injected into stable geological features (*i.e.* deep saline formations, oil and gas depleted wells or deposits of unprofitable coal), trapping it and avoiding its release into the atmosphere. [20] Alternatively, carbon dioxide can be used as it is (for example, to improve oil recovery, or for food and beverage industry) or can be converted into more useful products.

Considering all these steps of a CCS system, it has been estimated that the operating costs of the capture procedure account for 70–90% of the total expense. [21] For that reason, here now mainly the CO_2 capture step will be covered. The carbon dioxide capture technology for fossil fuel fired power plants can be divided mainly into three categories: i) post combustion, ii) pre combustion, iii) oxyfuel combustion methods (Figure 1.8).

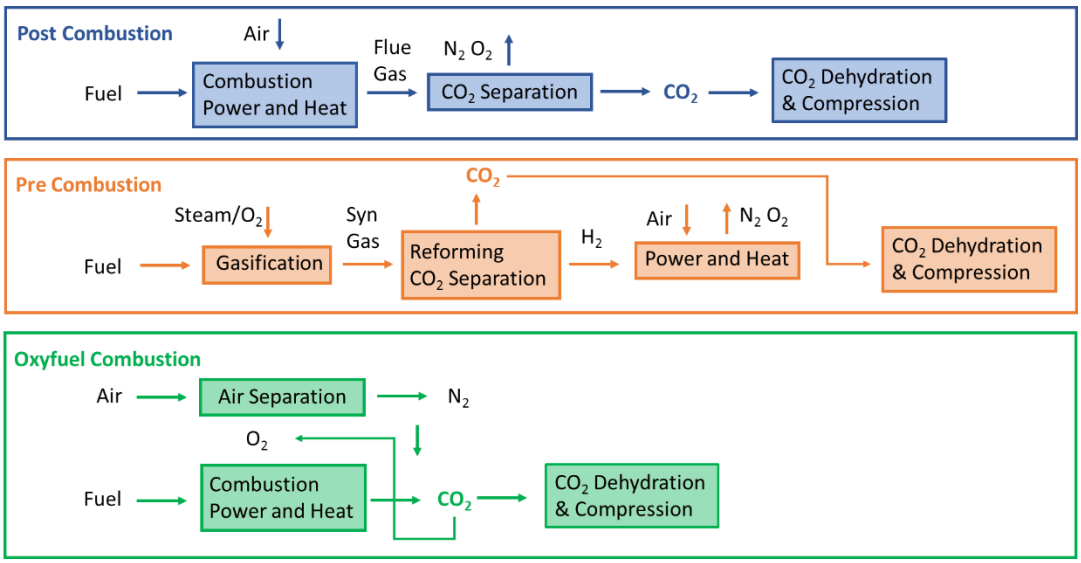

Figure 1.8. Schematic representation of post combustion, pre combustion and oxyfuel combustion processes.

Post combustion capture

Post combustion capture techniques consist in the capture of the carbon dioxide from the flue gases created during the fuel combustion with air.

The reactions involved in the combustion process are reported below:

From coal: $C + ½\ O_2 \rightarrow CO$; $CO + ½\ O_2 \rightarrow CO_2$ (1.1)

From hydrocarbons: $C_mH_n + (m+n)/4\ O_2 \rightarrow m\ CO_2 + n/2\ H_2O$ (1.2)

During the coal combustion, the carbon reacts with the oxygen at temperatures above 1000°C to form carbon monoxide. In this reaction also particulate matter (*i.e.* a combination of unburned coal and ashes) is formed. After, the carbon monoxide reacts with the oxygen forming carbon dioxide.[22] During hydrocarbons combustion instead, fuel reacts with oxygen at relatively low temperatures (between 200 and 600°C), forming CO_2 and water vapor. In these reactions, some impurities are also produced. First of all, water vapour is generated in the reaction between the excess of hydrogen in hydrocarbons and the oxygen. In a typical flue gas steam 6-15% of the total volume is composed by water vapor. In addition, sulphur present in the fuel source can react with the oxygen thus forming SO_2. Finally, molecular nitrogen present in the air and in the fuel can react with atomic oxygen at temperatures above 1200°C to form NO_x. The reactions involved in the formation of impurities are reported below:

$H_2 + ½\ O_2 \rightarrow H_2O$ (1.3)

$S + O_2 \rightarrow SO_2$ (1.4)

$N_2 + O \rightarrow NO_x + N$; $N + O_2 \rightarrow NO_x + O$ (1.5)

The amount of impurities produced during the combustion depends on the type of fuel used. For example, natural gas produces lower amount of carbon dioxide, SO_2

and NO_x respect to coal. The handling of all these impurities is a very important problem to deal with. [22]

In the post combustion capture technology, carbon dioxide is captured from a low pressure (about 1 bar) and low content (about 10%) gas stream. Consequently, the resulting CO_2 pressure is about 0.1 bar. Further details on the various CO_2 capture methods suitable in post combustion capture techniques are reported in Paragraph 1.4.

Pre combustion capture

Pre combustion capture methods consist in the capture of CO_2 from a synthesis gas before the fuel combustion. This method is applicable for Integrated Gasification Combined Cycle power plants (IGCC). In these power plants, the fuel is first gasified with either steam or oxygen at high temperature (1400°C) and pressure (35-55 bar) to produce a synthesis gas, consisting primarily in carbon monoxide and hydrogen.

$$C_xH_y + x\ H_2O \leftrightarrow x\ CO + (x+y/2)\ H_2 \quad (1.6)$$

$$C_xH_y + x/2\ O_2 \leftrightarrow x\ CO + (y/2)\ H_2 \quad (1.7)$$

After, the carbon monoxide reacts with water vapor in a water gas shift reaction, forming a stream gas consisting of CO_2 and H_2 (Reaction 1.8) from which the carbon dioxide must be separated.

$$CO + H_2O \leftrightarrow CO_2 + H_2 \quad (1.8)$$

The CO_2 contents in the stream is about 15-40%, and the pressure of the stream is higher compared to post combustion method (14-40 bar).

The remaining hydrogen gas is combusted for energy production. The carbon dioxide, instead, can be seized by contact with a physical sorbent in a column (Selexol, Rectisol, Fluor, Purisol processes) or by using membranes. [22]

Oxyfuel combustion capture

Oxyfuel combustion concerns the capture of carbon dioxide from flue gases formed during the fuel combustion with pure oxygen (instead of air, used in traditional post combustion systems). The pure oxygen (95-99%) is obtained from the air by separating it from nitrogen by using an Air Separation Unit (ASU). After, the oxygen is mixed with the carbon dioxide coming from a previous combustion reaction (carbon dioxide controls the flame temperature in the furnace), and the gas mixture feed the combustion chamber for the energy production. The stream gas produced with this technology contains a high amount of carbon dioxide (75%-80%), water and trace impurities. Because of the high concentration of CO_2 in the stream gas obtained with this technology, much more efficient capture techniques can be applied with respect to those used in the post combustion systems. [22] In fact, with this methodology the carbon dioxide is simply captured by cooling the gas stream condensing out the water steam.

1.4 Post Combustion CO_2 Capture Methods

Post combustion capture methods are the most applicable in short term as they can be easily adapted to existing fossil fuel power plants. For these reasons, in this PhD thesis only applications to post combustion capture methods will be studied. The post combustion capture technologies most studied are: i) cryogenic distillation, ii) membrane separation, iii) absorption, iv) adsorption. A summary diagram of all these techniques is given Figure 1.9.

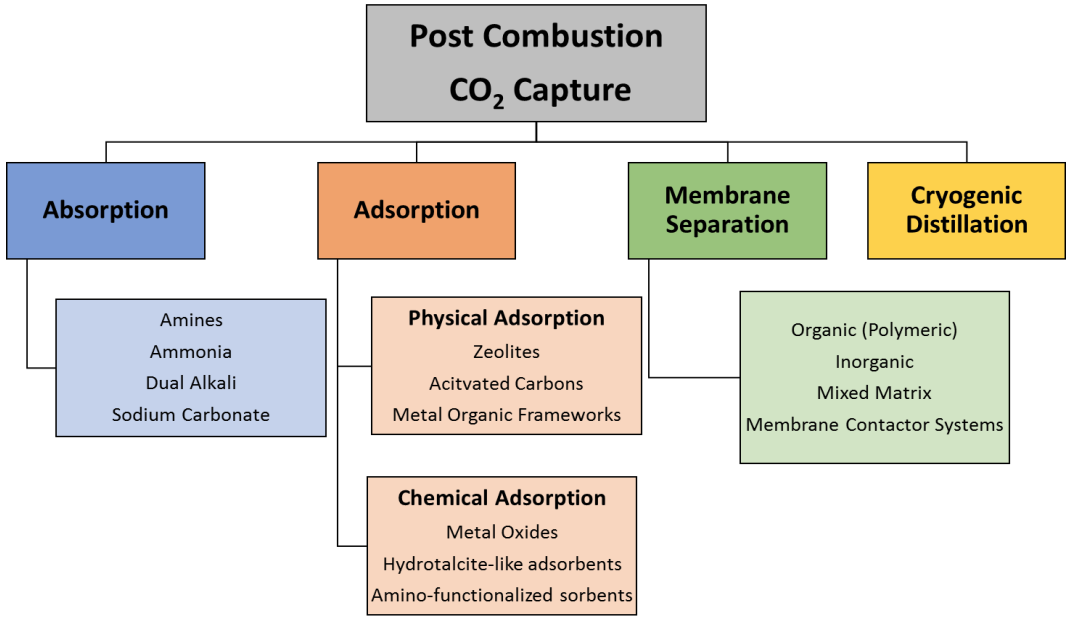

Figure 1.9. Schematic representation of different post combustion capture technologies.

Cryogenic distillation

In cryogenic distillation system, carbon dioxide is physically separated from other gas stream on the basis of sublimation and dew points. In this process, the flue gas containing carbon dioxide is cooled to desublimation temperatures (from -100 to -135 °C); after, solid CO_2 is separated from other gases and compressed to final pressures (100-200 atm). This process presents a series of advantages. First of all the energetic and economic costs seem to be at least 30% lower than the most competing processes. In addition, this technique is solvent free, and provides high efficient removal of most pollutants (*i.e.* SO_x and NO_x). [23]

Membrane separation

In membrane separation process, the membrane acts as a filter, removing carbon dioxide from the CO_2/N_2 gas streams (previously purified removing NO_x and SO_x) and forming a CO_2 rich permeate. Following, the gas stream is cooled below 100°C

in order to avoid the degradation of the membranes, and is compressed to 15-20 bars aiming to create a high driving force for the separation. The driving force in these systems is the difference is the difference in chemical potential.

Many types of membranes are used for the separation process. The main categories are: organic (polymeric) membranes, inorganic membranes, mixed matrix membranes (micro or nanosized inorganic particles incorporated into a polymeric matrix) and membrane contactor systems (a method that combine a membrane with an absorption liquid, as a solution of amines, into a single unit). Membrane separation process expects low capital costs, a compact design and avoids the use of chemicals and solvents. However, high pressure and multiple steps are required for an efficient separation. [22]

Absorption methods

In the absorption methods, carbon dioxide is separated from the gas stream by using a liquid absorbent: CO_2 is contacted with the liquid and is absorbed from the gas to the liquid phase. Since carbon dioxide is an acid gas, it is preferable to use a basic absorbent to form a neutral solution. After a purification step in which NO_x and SO_x are removed, the gas is cooled and then put into contact with the absorbent liquid in a column, to form intermediate compounds. Following, the solution is injected in a stripping column where, after heating, CO_2 is regenerated. In this way, the solvent is regenerated and recycled back to the absorber unit, and a CO_2 concentrated stream is produced. Several types of absorption processes exist. The major are: i) amine adsorption, ii) aqua ammonia absorption, iii) dual alkali absorption and iv) sodium carbonate adsorption. [22]

Amine absorption

Systems based on amine solutions are one of the most widely used technologies. In amine adsorption process, the flue gas is cooled to 40-60°C and is put in contact with the solution of amines by using a packed bed

column. Typically used sorbents are 25/30% acqueous solutions of monoethanol amine (MEA), diethanol amine (DEA) and methyl diethanol amine (MDEA). The absorbed carbon dioxide reacts chemically with the amino group, thus forming carbamate and bicarbonate products. The reactions involved are reported in Reactions 1.9 and 1.10.

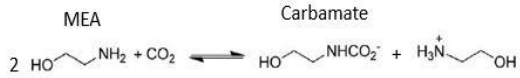

(1.9)

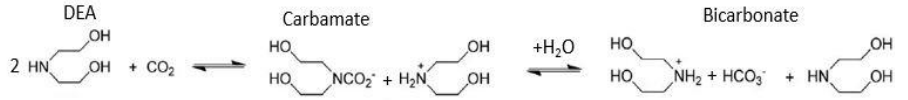

(1.10)

After the absorption, the carbon dioxide solution is sent to a stripping unit, where is heated between 100 and 200°C, regenerating the amine solution and producing a CO_2 concentrated gas stream (99%).

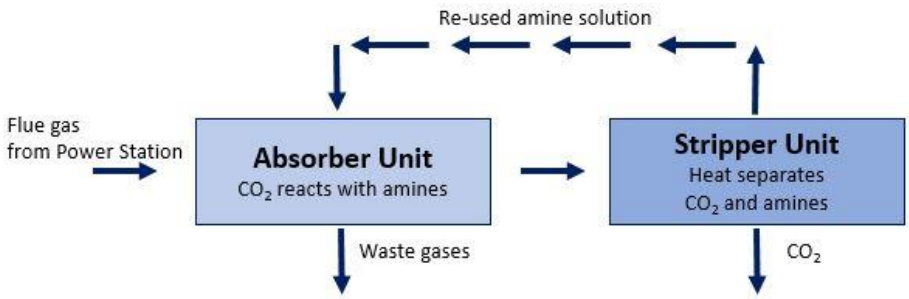

Figure 1.10. Schematic Representation of a CO_2 capture system based on amine solution absorption.

Capture systems based on amine absorption are not only studied in literature, but are also commercially available. The three technology actually marketed are: Kerr-McGee/AGG Lummus Crest (KMALC) process (using 15-20 wt%

of MEA), Fluor Econamine FG Plus^{SM} (EFG+) process (using a 35 wt% of MEA solution and an appropriate inhibitor, that reduces the corrosive nature of the amine solvent) and KM-CDR process (using a line of sterically hindered amines, characterized by low corrosivity and low degradation from O_2). [22]

Although the absorption process with amine solutions is technologically mature, it presents some disadvantages. The amine solvent can not be fully regenerated, corrodes the equipment and degrades from O_2, NO_x and SO_x. In addition, a high energy consumption is required during the solvent regeneration, and the waste stream can be hazardous. Finally, this process has a low CO_2 loading capacity of the solvent (about 0.4g CO_2 /g MEA), and the scale up is problematic: current technologies can have a maximum absorption capacity of 800 tons/day, but a 500 MW power plant emits carbon dioxide about 10 times more. For these reasons, in recent years research is shifting from the use of amines contained in a liquid solvent to the utilization of amines contained in solid adsorbents. [22] These technologies will be described in more detail in Paragraph 1.5.

Aqua ammonia process

In the aqua ammonia process, the flue gas is put in contact with an ammonia solution in the absorption column after being cooled to 15-27°C (low temperatures are required because of the volatility of ammonia). The reactions involved in the chemical absorption are given in Reactions 1.11 and 1.12.

$$2\ NH_{3\ (aq)} + CO_{2\ (g)} + H_2O_{\ (l)} \rightarrow (NH_4)_2CO_{3\ (s)} \quad (1.11)$$

$$NH_{3\ (aq)} + CO_{2\ (g)} + H_2O_{\ (l)} \rightarrow (NH_4)HCO_{3\ (s)} \quad (1.12)$$

The peculiarity of this process is that, together with the capture of CO_2, it can remove pollutants as NO_x and SO_x. In fact, after an oxidation pretreatment in which NO_x and SO_x are oxidized to NO_2 and SO_3, these gases reacts with the ammonia solution directly in the absorption unit, thus forming ammonium nitrate and sulfate, which can then be sold as fertilizers. The reactions involved are reported in Reaction 1.13.

$$NH_{3\,(aq)} + NO_{2\,(g)} + SO_{3\,(g)} \rightarrow NH_4NO_{3\,(s)} + (NH_4)_2SO_{4\,(s)} \quad (1.13)$$

After the capture step, the carbon dioxide solution is sent to a stripping column, where ammonium carbonate and bicarbonate thermally decompose at temperatures between 27 and 92 °C, releasing CO_2 and regenerating the ammonia solution.

The aqua ammonia process present some advantages, such as the high carbon dioxide loading compared to the amine solution absorption process (1.20 g CO_2 /g MEA), the possibility of managing pollutants as NO_x and SO_x, and sell the resulting products ammonium nitrate and sulphate as fertilizers, together with the avoidance of equipment corrosion issues and additives anti degradation from oxygen. However, it is necessary to provide equipment plugging due to the formation of solid products, and the loss of ammonia vapor during the stripping process.

Dual alkali absorption

In the dual alkali absorption process carbon dioxide, after a purification step aimed at remove NO_x and SO_x pollutants and a cooling step up to 25°C, reacts with methylaminoethanol (MAE) and sodium chloride in acqueous solution. The reactions involved are given in Reaction 1.14.

$$CO_{2\,(g)} + NaCl_{\,(aq)} + H_2O_{\,(l)} + HOCH_2CH_2(CH_3)NH_{\,(aq)}$$
$$\rightarrow NaHCO_{3\,(s)} + HOCH_2CH_2(CH_3)NH_2Cl_{\,(aq)} \quad (1.14)$$

Following, a second alkali is needed to regenerate MAE, but has not been identified yet.

The dual alkali absorption process has an absorption capacity of 0.54 g CO_2 /g MAE, but still many investigations are to be carried out, especially regarding the regeneration step.

Sodium carbonate absorption

Concerning sodium carbonate absorption method, the inlet flue gas containing carbon dioxide is treated with Na_2CO_3 to obtain sodium bicarbonate. The reactions involved in this process are reported below.

$$CO_3^{\,2-}{}_{(aq)} + H_2O_{\,(l)} + CO_{2\,(g)} \rightarrow 2\ HCO_3^- \quad (1.15)$$

$$Na^{\,+}{}_{(aq)} + HCO_3^-{}_{(aq)} \leftrightarrow NaHCO_{3\ (s)} \quad (1.16)$$

After the capture step, the CO_2 loaded slurry is sent to the stripping unit, the CO_2 is released and the sodium carbonate is regenerated (temperature and pressure conditions: 121°C, 2 bar). The theoretical CO_2 absorption capacity of the sodium carbonate absorption method is 0.73 g CO_2 /g CO_3^{2-} (higher compared to the amine solution absorption method). In addition, sodium carbonate is non hazardous and non volatile. The major disadvantage instead is the slower absorption rate compared to amine solution absorption systems.

Adsorption method

Adsorption method consists in the capture of carbon dioxide using solid sorbents. Further details on this method are given in Paragraph 1.5.

1.5 CO_2 Capture by Using Gas Adsorption Methods

1.5.1 Introduction

It is believed that the carbon dioxide capture by using solid is one of the most promising technologies for CCS since it requires less energy respect to the liquid absorption, it is not associated with the production of any liquid refuse and is applicable to a wide range of temperatures. For these reasons, many types of solid adsorbents have been investigated in the literature.[24] Ideally, a solid suitable for the carbon dioxide capture should have fast adsorption and desorption kinetics, high adsorption capacity, high surface area (in order to maximize the surface sites for CO_2 adsorption) and good selectivity. In addition, it should be regenerable at mild conditions (low pressure and temperature), stable and durable, usable in a wide range of operative conditions and producible at low costs. Finally should be tolerant toward impurities such as NO_x, SO_x and water vapor. In reality, all practical adsorbents are characterized by only some of these features. [24] Below, the main solid adsorbents will be reported and described.

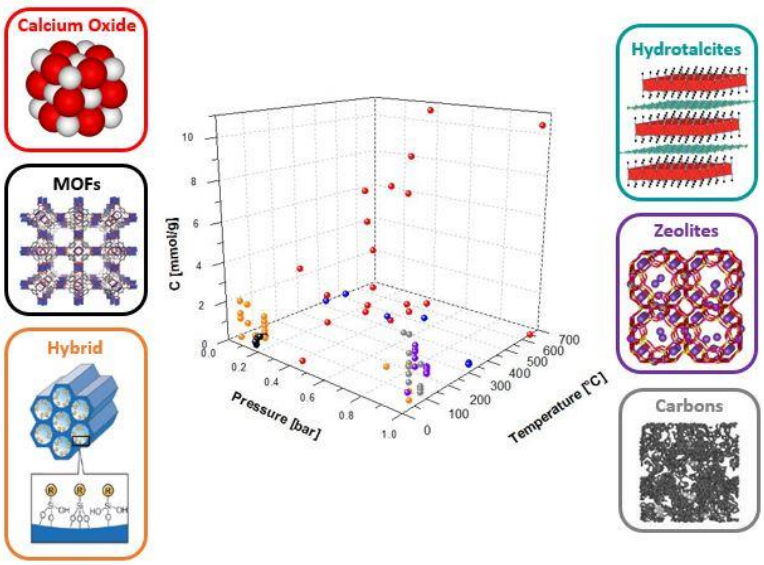

Figure 1.11. Schematic Representation of the main solid adsorbent for CO_2 capture and their performances. The graph is obtained using data reported in reference 24.

1.5.2 Physical Adsorbents

Zeolites

Zeolites are a highly ordered microporous crystalline aluminosilicates, consisting of TO_4 tetrahedra (where T is Si or Al). This class of materials is able to adsorb carbon dioxide due to the presence of aluminium in their structure, as isomorphic substitute of silicon. The aluminium in fact induces a negative charge in the structure that is counterbalanced by cations present in the pore space. If alkali cations are used, zeolites becomes capable to adsorb acid gases as carbon dioxide. The main mechanism by which this class of materials adsorb carbon dioxide is the physisorption. In particular, the physical adsorption is influenced by the electric field created by hydrogen bonding with surface silanol groups and by alkali cations. For this reason, physisorption directly depends on the amount of Al in the framework (and consequently the amount of alkali cations that counterbalance the charge): increasing the aluminium content, the base strength of the zeolites increases. In addition, the physisorption depends on the type of cations. In fact, the basicity of exchanged zeolites increased by decreasing the electronegativity of the cations. For example, Barthomeuf suggested that Cs-exchanged zeolite X present the highest base strength. [25] Finally, the physisorption properties of zeolites are influenced by the porosity. For example, Siriwardane et al. reported that the highest CO_2 adsorption capacities were observed in zeolite 13X, the material with the highest pore diameter and pore volume among those considered.[26] Even though the main adsorption mechanism is the physisorption, zeolites are able to adsorb carbon dioxide also by chemisorption, forming carbonate and carboxylates. This phenomenon is due to the interaction with surface oxide ions adjacent to exchangeable cations that bind irreversibly the CO_2. For this reason, in order to completely regenerate the zeolite a temperature swing system until 350°C (energy and time intensive) is used.

Zeolites are characterized by relatively high adsorption capacities at mild conditions (0-100 °C, 0.1-1 bar of CO_2), varying in a range from 0.004 to 0.216 g CO_2/g zeolite. A summary of performances obtained from different zeolites is given in Table 1.1.

It's important to note that data resumed in the following table are not fully comparable because are obtained in different experimental conditions. Unfortunately, there is an objective difficulty to find in literature adsorption capacity values achieved at similar conditions. For this reason, the comparison between the adsorbent materials must be done with caution. The same considerations apply to all the comparison tables given in this chapter.

Material	**T [°C]**	**p CO_2 [bar]**	**p tot [bar]**	**q [mmol/g]**	**REF**
Natural	25	0.15*	1	1.25	25
13X	120	0.15*	1	0.70	26
5A	120	0.15*	1	0.38	26
4A	120	0.15*	1	0.50	26
WE-G592	120	0.15*	1	0.60	26
APG-II	120	0.15*	1	0.38	26
Na-Y	0	0.1	-	4.9	28
Na-X	50	1	-	2.70	29
Na-X	100	1	-	1.24	29
Na-X-h	50	1	-	2.52	29
Na-X-h	100	1	-	1.37	29
Na-X-c	50	1	-	2.14	29
Na-X-c	100	1	-	1.41	29
Cs-X-h	50	1	-	2.42	29
Cs-X-h	100	1	-	1.48	29
Cs-X-c	50	1	-	1.76	29
Cs-X-c	100	1	-	1.15	29

Table 1.1 CO_2 adsorption capacity values (q) of different zeolites from literature at different temperature and pressure conditions. * indicates presence of water. [26]

The adsorption capacities of zeolite adsorbents summarized in Table 1.1 illustrate that zeolites generally presents adsorption capacity values higher than 1 mmol/g at temperatures lower than 100°C. However, a substantial decrease in CO_2 adsorption capacities at higher temperatures is observable.

In addition, this class of materials show significant decreases in adsorption capacity in presence of water, which competes with the CO_2 for the adsorption. The presence of water, however, can be favourable at low carbon dioxide partial pressure. In fact, Habgood et al. reported that, in these conditions, the presence of pre-adsorbed water could accelerate the CO_2 adsorption in NaX zeolite by decreasing the activation energy for the carbon dioxide diffusion, or by accelerating the formation of bicarbonate compounds on the surface. [30]

Compared to other inorganic adsorbents, zeolites can be easily regenerated, and never degrade even after different cycles of adsorption and desorption.

In zeolites, kinetics of carbon dioxide adsorption are extremely fast: often the maximum adsorption capacity is reached within few minutes. The adsorption kinetics of zeolites are influenced by operating conditions: increasing temperature or pressure, the adsorption kinetics accelerate. [22] [24]

Due to the favourable capture capacities in mild conditions and rapid kinetics, zeolites are particularly suitable for CO_2 adsorption in post combustion conditions.

Activated carbons

Activated carbons can be derived from different materials, as coals, industrial products (*i.e.* wastes of polymeric materials, petroleum and coke pitch), wood and other biomass sources (*i.e.* coconut shells and olive kernels). For these reasons are producible with low costs. Depending on the deriving materials, carbons with different distribution, structure and size of the pores (and consequently different adsorption properties) can be obtained. Activated carbons from raw materials typically can be prepared by using a two steps procedure: carbonization (*i.e.* heating and pyrolysis of raw precursors in inert atmosphere) and physical/chemical

activation, in which the pre-formed materials are modified in order to produce porosity and active sites, increasing the specific surface area. Adsorption on activated carbons occurs via physisorption. Adsorption capacity values of activated carbons at mild operating conditions (25–75 °C, 0.1-1 bar of CO_2), varying in a range from 0.003 to 0.154 g CO_2/g activated carbon, slightly lower compared to zeolites in similar conditions. A summary of performances obtained from different carbons is given in Table 1.2.

Material	**T [°C]**	**p CO_2 [bar]**	**p tot [bar]**	**q [mmol/g]**	**REF**
Carbon	25	1	1.5	3.3	31
Carbon	2	1	2	3.5	32
Carbon	2	1*	2	1	32
Carbon	25	1	1	2.5	33
C	25	1	1	1.59	33
C	75	1	1	0.45	34
CN800	25	1	1	1.91	34
CN800	75	1	1	0.61	34
R	25	1	1	2.07	34
R	75	1	1	0.73	34
C35N000	25	1	1	1.23	34
C35N000	75	1	1	1.73	34

Table 1.2. CO_2 adsorption capacity values (q) from literature at different temperature and pressure conditions. * indicates presence of water. Nomenclature: C: wood-based granular carbon activated by phosphoric acid; R: peat-based steam activated extruded carbon; N800: modified under N_2 atmosphere at 800°C; C35N000: commercially available activated carbon; C35N400: sample treated with ammonia at 400°C. [24]

As can be seen in Table 1.2, by increasing the temperature, the CO_2 adsorption capacity decreases. This behaviour is similar to that of zeolites, as is typical of a physisorbent material.

In addition, similarly to zeolites, also activated carbons are sensible to water (even though they are more hydrophobic) because of water may competitively be adsorbed on the carbon surface and because of the aging effect due to a gradual oxidation of the carbons

Concerning the regeneration step, activated carbons can be easily regenerated with pressure swing system, due to the low heat of adsorption (lower compared with that of zeolites). For these reasons, activated carbons are considered one of the most regenerable materials used for the CO_2 capture.

Some studies have found that, even if in mild conditions activated carbons and zeolites have similar adsorption capacities, at higher pressure (*i.e.* 10 bar) activated carbons presents higher adsorption capacities compared to zeolites. These pressure conditions, however, are present in pre combustion systems, and therefore will not be deepened in this paragraph. [35]

The absorption kinetics of activated carbons are fast, similarly to zeolites: the equilibrium is reached in few minutes. [22] [24]

Recently, activated carbons with basic and/or hydrophobic surface properties have been studied in order to improve the adsorption properties of these materials. Modification of the activated carbons surface can be carried out introducing on the surface other constituents, such as amino groups. [36]

Due to low material and regenerative costs, activated carbons are competitive with other carbon dioxide adsorbents.

Metal Organic Framework (MOF)

Metal Organic Framework are microporous materials composed by central cations linked together with organic ligands, thus forming a 3D structure. Different networks

can be created by varying the metal–ligand combination, or by using metals with multiple coordination sites or multidentate ligands.

MOF materials show CO_2 adsorption capacity values in some cases higher compared to zeolites and activated carbons. In Table 1.3 the CO_2 adsorption capacity values of some MOF present in literature are reported.

Material	**T [°C]**	**p CO_2 [bar]**	**p tot [bar]**	**q [mmol/g]**	**REF**
Mg-MOF-74, Mg-CPO-27	30	0.15	-	0.45	37
Mg-MOF-74, Mg-CPO-27	40	0.15	-	0.43	37
Mg-MOF-74, Mg-CPO-27	50	0.15	-	0.38	37
Mg-MOF-74, Mg-CPO-27	60	0.15	-	0.33	37
Mg-MOF-74	23	0.15	-	5.30	38
Co-MOF-74	23	0.15	-	2.70	38
Zn-MOF-74	23	0.15	-	1.30	38
Ni-MOF-74	23	0.15	-	2.70	38
CuDDQ	25	1.00	-	8.00	39
CPM-200-Fe/Mg	25	1.00	-	5.07	40

Table 1.3. CO_2 adsorption capacity values (q) of MOF from literature at different temperature and pressure conditions. * indicates presence of water. [41]

Studies performed at higher CO_2 partial pressures show that in these conditions MOFs show adsorption capacity values even higher, owing to their high surface area. These conditions, however, are typical of pre combustion systems, and therefore this aspect is not treated in detail in this section. In order to increase the adsorption capacities at low CO_2 pressures, amine functionalities can be incorporated into the ligands of MOFs. In this way, chemical adsorption sites are provided, making MOFs excellent for low partial pressure CO_2 capture applications. [42]

As all physisorbent material, the adsorption capacity of traditional MOFs decrease by increasing the temperature (Table 1.3).

The presence of water, however, represents a particularly important problem for the CO_2 adsorption. In fact, water molecule can displace the MOF ligands, creating structural defect in the crystal lattice.

1.5.3 Chemical Adsorbents

Metal Oxides

The CO_2 adsorption can be promoted by using basic sites of some metal oxides, as alkaline (Na_2O, K_2O) or alkaline earth (CaO, MgO) metal oxides. Considering for example calcium oxide (one of the most used oxide for this application), it can react with an equivalent of CO_2 to form calcium carbonate (Reaction 1.17).

$$CaO\ (s) + CO_2\ (g) \leftrightarrow CaCO_3\ (s) \qquad (1.17)$$

Following, CO_2 can be regenerated with the inverse reaction (decomposition).

On the basis of the stoichiometry of the reaction reported above, the maximum theoretical amount of adsorbed CO_2 is 17.8 mmol/g. Capacity values reported in literature are lower compared to theoretical value, but they are still higher with respect to those of other inorganic chemisorbents (Table 1.4). Metal oxides, as well as hydrotalcites (derscribed below), are identified as high tempearature adsorbents, and they are often treated as a separate class of adsorbents compared to low temperature chemisorbents and physisorbents. This is also evident in the high temperatures reported in Tables 1.4 and 1.5.

Material (Precursor)	T [°C]	p CO_2 [bar]	p tot [bar]	q [mmol/g]	REF
CaO	450	0.41	1	4.5	43
$Ca(OH)_2$	450	0.25	1	6.7	43
$Ca(OH)_2$	450	0.25*	1	9.5	43
$Ca(OH)_2$	450	0.41	1	7.2	43
$Ca(OH)_2$	550	0.41	1	8.5	43
$Ca(OH)_2$	650	0.41	1	10.7	43
$CaCO_3$	600	0.34	1	6.3	43
$CaCO_3$	300	0.2	1	1.5	44
$CaCO_3$	500	0.2	1	4.8	44
CaO	650	0.05	1	2.3	45
Limestone	650	1	-	10.5	46

Table 1.4. CO_2 adsorption capacity values (q) from literature at different temperature and pressure conditions. * indicates presence of water. [24]

As can be observed from the results reported in Table 1.4, the type of precursors affects the adsorption capacity of calcium oxide-based materials. For example, adsorbents obtained by calcining precursors, present different adsorption capacities compared to those derived from the pure calcium carbonate. In addition, the carbon dioxide adsorption capacity values can depend to both particle sizes and surface areas of calcium oxides. For example, the adsorption capacity in a pure carbon dioxide stream after 24 h of carbonation of micrometeric-size particles (10 μm) was 13.4 mmol/g, whereas that of the nanometric particles (10 nm) reached 16.6 mmol/g. [47] In addition, after a compression procedure of the nanosized particles, in which the surface area fell from 38.4 to 0.5 m^2/g, the CO_2 capture capacity decreased to 8.9 mmol/g. [48]

Concerning the adsorption kinetic, that in many cases controls the overall kinetics of the process, it is controlled by the speed of the carbonation process. The adsorption kinetic in these materials is much slower compared to that of physisorbent solids (*i.e.* zeolites or activated carbons): several hours of adsorption may be required in order to achieve *ca.* 70% of the total CO_2 adsorption capacity.

Regenerability of calcium oxide-based adsorbers can be influenced by morphological and textural factors, such as particle size, porosity and surface area. In general, their adsorption capacity may decrease by 25% after carbonation / calcination cycles due to pore closure and particles sintering.

Metal oxide-based materials are preferable with respect to other adsorbents due to their low cost and wide availability, together with their high adsorption capacities. However, their practical use is hindered by kinetic factors.

Hydrotalcite-like compounds

Hydrotalcite-like compounds are anionic clays represented by the generic formula $[(M^{2+}_{1-x}\ M^{3+}_{x}\ (OH_2)]^{x+}\ (A^{m-}_{x/m}\cdot nH_2O)^{x-}$, where M^{2+} = Mg^{2+}, Ni^{2+}, Zn^{2+}, Cu^{2+}, Mn^{2+} or others, M^{3+} =Al^{3+}, Fe^{2+}, Cr^{3+} or others, and A^{m-} =CO_3^{2-}, SO_4^{2-}, NO_3^{-}, Cl^{-}, OH^{-} or others.[49] This structure is composed by hydroxide layers, in which trivalent cations, located at the centre of octahedral sites, partially substitute divalent cations, generating an excess of positive charge. This positive charge is counterbalanced by $A^{m-}_{x/m}$ anions or water molecules located in the interlayer space.

The CO_2 capture capacity values of hydrotalcites are in general lower compared to those of other chemical adsorbents (typically <1.0 mmol/g). Values of CO_2 capture capacity of some hydrotalcites-like materials are reported in Table 1.5.

Material	T [°C]	p CO_2 [bar]	p tot [bar]	q [mmol/g]	REF
HTIcs	400	0.45	-	0.59	50
HTIcs	480	0.58	-	0.48	50
HTIcs	400	0.44*	-	0.62	50
HTIcs	480	0.27*	-	0.50	50
HTIcs	208	1*	-	0.9	51
HTIcs	302	1*	-	0.8	51
HTIcs	400	0.05	1	0.33	52
HTIcs	450	0.05	1	0.32	52
HTIcs	500	0.05	1	0.27	52
HTIcs	300	1	-	0.42	53
HTIcs	300	1	1	0.5	54
HTIcs	300	1	1	0.4	54

Table 1.5. CO_2 adsorption capacity values (q) from literature of hydrotalcites-like adsorbents at different temperature and pressure conditions. * indicates presence of water. [24]

As it can be seen in Table 1.5, some variations in the adsorption capacities can be observed by modifying the type and the amounts of framework components. The maximum amount of adsorbed CO_2 was obtained with a Mg^{2+} and Al^{3+} cations ratio of 1: 1.[53] [54]

The presence of water contributes positively to the CO_2 adsorption properties of hydrotalcites. In fact, water allows a faster activation of adsorption sites, prevents the site poisoning and favours the formation of bicarbonates following the reaction:

$$M_2CO_3 + CO_2 + H_2O \rightarrow 2MHCO_3 \quad (1.18)$$

where M indicates a small amount of sodium or potassium present in the material.

The adsorption kinetics of hydrotalcites is generally faster than that of calcium oxides. In general, the maximum adsorption capacity is reached in about 10 minutes. As all chemisorbents, the adsorption process is composed by an initial quick step, followed by a slower step leading to the reaching of the equilibrium.
The regeneration of these materials can lead be more or less effective depending on the operating conditions used. In general, however, in both anhydrous and wet conditions, the adsorption capacity of hydrotalcite-based materials decreases during the first adsorption-desorption cycle and then remain approximately constant.
Due to the adsorption capacity, their high surface area and the framework stability, hydrotalcytes-like materials are still competitive for the carbon dioxide adsorption.

Amino-functionalized adsorbents

CO_2 absorption by using liquid solutions of amines is actually one of the most advanced technologies used in CCS, but presents significant disadvantages described Paragraph 1.4. In order to overcome these problems, solid adsorbents containing amino groups, (working with similar principle to the liquid solutions of amines) are largely studied in literature. For example, the large energy cost needed to heat H_2O in the amine solution during the regeneration step can be avoided by replacing water with a solid support with lower heat capacity (for example 0.8 kJ/kgK in the case of SBA-15 silica vs. 4.2 kJ/kgK for H_2O). In addition, for amino-based adsorbers, degradation due to evaporation and vessel corrosion are not an issue.
Since the adsorbents studied during this PhD thesis belong to this class of materials, organic-inorganic hybrid adsorbents will be described in detail in the next paragraph.

1.6 Amino-functionalized Materials for CO_2 Capture

Amino-functionalized solid adsorbers consist of a support on which amino groups are present. Among other materials, silica is often used as support. This class of materials is promising for practical applications of the CO_2 capture, thanks to the easier and less expansive (in term of energy and costs) regeneration step compared to the amino-solution method, the rapid achievement of the equilibrium and the possibility of work between 20 and 100 °C. However, their use is still hindered by their low adsorption capacity and low selectivity towards carbon dioxide in the presence of other gases, as nitrogen [55].

In order to better understand the carbon dioxide adsorption process by amino-functionalized materials, the chemisorption mechanisms are described below.

1.6.1 Chemisorption Mechanisms

The reaction between CO_2 and amino groups may occur by many different mechanisms. Primary and secondary amines may react with carbon dioxide producing ammonium carbamates through the formation of zwitterionic intermediates. [56] The zwitterionic mechanism is reported in Equations 1.19 and 1.20.

$$CO_2 + RNH_2 \leftrightarrow RNH_2^+CO_2^- \quad (1.19)$$

$$RNH_2^+CO_2^- + B \rightarrow RNHCO_2^- + BH^+ \quad (1.20)$$

In the first step, the electron pair of the amino group attacks the carbon from CO_2 to form the zwitterion. Following, a base (*i.e.* another amine, H_2O or OH^-) deprotonates the zwitterion thus forming the ammonium carbamate. Under dry conditions, where H_2O and OH^- are absent, the maximum amine efficiency obtainable for an amino-functionalized adsorbent is 0.5 mol CO_2 /mol N, while under humid conditions,

where H_2O can participate as a base, the maximum amine efficiency is 1.0 mol CO_2 /mol N. In the case of dry condition, nitrogen acting in the second step can belong to the same chain (intermolecular mechanism) or to an adjacent chain (intramolecular mechanism).

Another proposed mechanism for primary and secondary amines involves the formation of carbamic acid. According to this mechanism, the zwitterion formed during the amine attack to the carbon of CO_2 can re-arrange forming carbamic acid (Equation 1.21). [57]

$$RNH_2^+CO_2^- \rightarrow RNHCOOH \quad (1.21)$$

In this mechanism, only one nitrogen is necessary to obtain the carbamic acid, thus indicating that the maximum amine efficiency is 1.0 mol CO_2/ mol N.

An additional mechanism proposed in literature involves the CO_2 capture by amine interactions with silanols on the surface. [58] In particular, this mechanism involves the formation of a surface-bound carbamate formed by the reaction of the intermediate zwitterion with a surface silanol. [59] The reaction is given in Equation 1.22.

$$RNH_2^+CO_2^- + SiOH \rightarrow RNHCO_2Si + H_2O \quad (1.22)$$

Tertiary amines can react with CO_2 through a different mechanism, reported in Equations 1.23, 1.24 and 1.25. [60]

$$R_3N + H_2O \rightarrow R_3NH^+ + OH^- \quad (1.23)$$

$$CO_2 + OH^- \rightarrow CO_2^-OH \quad (1.24)$$

$$R_3NH^+ + CO_2^-OH \rightarrow R_3NH^+CO_2^-OH \quad (1.25)$$

In the first step, the tertiary amine dissociates water forming quaternary cationic species and hydroxide ion (Eq. 1.23). Following, the OH^- species reacts with the carbon dioxide to form the bicarbonate anion (Eq. 1.24). Finally, protonated amine and bicarbonate associate (Eq. 1.25). Primary and secondary amines, in addition to the zwitterionic mechanism, can react with water and carbon dioxide through this mechanism. While the activation energy for this mechanism is lower compared to that of the zwitterionic one, the constant rate is smaller. Consequently, initially the zwitterionic mechanism occurs forming carbamates, which are then eventually converted into carbonates and bicarbonates. This mechanism occurs only when high amounts of water is present (*i.e.* at conditions in which capillary condensation of water occurs). [61]

1.6.2 Amino-functionalized Supports

The first study of amino-supported silica for the CO_2 capture was realized by Tsuda et al. in 1992. [62] In their work, amorphous silica gels were synthesized by co-condensing different amine-containing silanes and tested for CO_2 capture applications. Following, different siliceous materials of different nature, on which amino groups are inserted, were studied. The first use of a mesoporous (amorphous) silica functionalized with amino groups for the carbon dioxide adsorption was performed by Leal et al. [63] Following, ordered mesoporous silica were widely studied as solid supports thanks to their high surface area, high volume of pores, reproducible synthesis and good mechanical and thermal stability. Ordered mesoporous silica can be divided into several families including MCM-n (Mobil Crystalline Materials), SBA (Santa Barbara Amorphous materials), MCF (Mesocellular Silica Foams) and HMS (Hierarchical Mesoporous Silica).

The hybrid materials based on silica can be divided mainly in two classes: amines physically impregnated into the pore space of the siliceous support and amines covalently bound to the silica support.

Amines physically impregnated on siliceous supports

One method of supporting amine on a silica surface consist in suspending the siliceous support in a solution containing the desired amine to allow it to spread on the surface (wet impregnation). Solvent is subsequently removed by evaporation [64]. Hydroxyls groups on the silica surface bind through hydrogen bond the amino groups, promoting the distribution of the amino chains.

In 2002, Song et al. [64] report for the first time the use of a mesoporous silica (MCM-41) impregnated with polyethyleneimine (PEI) for the carbon dioxide capture. Following, a large number of amines, from monoamines to aminopolymers, were studied for impregnation on siliceous materials with the intent of maximize the percentage of nitrogen in the sample in order to maximize the capture capacity. For example diethanolamine (DEA), ethylenediamine (EDA), diethylenetriamine (DETA), tetraethylenepentamine (TEPA), pentaethylenehexamine (PEHA), chloropropylamine, urea, melamine, 1,8-diazabicyclo[5.4.0]undec-7-ene (DBU) and 1,5-diazabiciclo-[3.4.0]non-5-en (DBN) were investigated. However, the most commonly used amine for impregnation is the polyethyleneimine, in the form of branched aminopolymer (containing primary, secondary, and tertiary amines) or a linear aminopolymer (composed by secondary amines with primary amine termini), because of its high nitrogen contents (33% w/w).

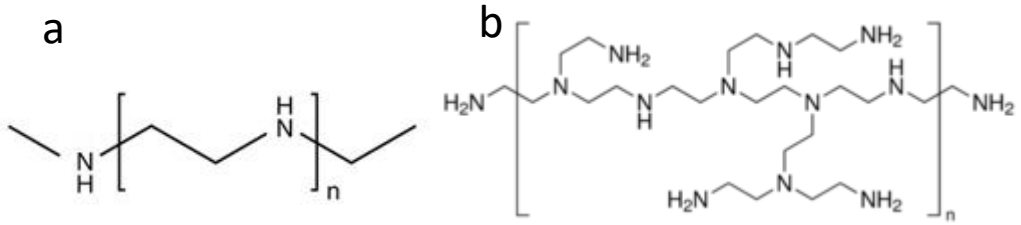

Figure 1.12. Structure of linear (a) and branched (b) polyethyleneimine.

Among the various possibilities, the most frequent used PEI have low molecular weight, because of the easier impregnation into the silica porosity (longer polymer chains can block the pore entrance and prevent a complete penetration into the pores).

Not only the type and the amount of physisorbed amine, but also the nature of the support can affect many adsorbent properties of these materials. For example, the amount of hydroxyl groups present on the surface of the support can affect the amine efficiency: since the amino groups can interact with surficial silanols, they will not all be available to react with carbon dioxide, and therefore the maximum efficiency obtainable will always be less than ideal (< 0.5 mol CO_2/mol N in anhydrous conditions).[24]

The most used porous siliceous support is the amorphous silica, but its disordered structure and porosity makes difficult the CO_2 access to the adsorption sites. This means that ordered mesoporous silicas are preferred for their high specific surface area and high volume of pores. In mesoporous structured supports, the pores dimension affect heavily the amount of adsorbed CO_2. For example, Ahn et al. evaluated the adsorption properties of various mesoporous silica supports impregnated with 50 wt% of PEI.[65] The authors found that the adsorption capacities increased following the order MCM-41<MCM-48<SBA-16~SBA-15<KIT-6, corresponding to the order of average pore diameter of the support (2.8, 3.1, 4.1, 5.5, and 6.5 nm respectively).

The adsorption capacity of ordered porous materials is also influenced by the ratio between the amount of impregnated amine and the size of the pores. In fact, an excessive increase in amount of organic chains (> 50 wt.%) causes a decrease in the adsorption properties due to the complete occupation of the pores, that make more difficult the spread of the gas inside [66] [64]. Adsorption capacity values obtained from different siliceous support impregnated with amine are given in Table 1.6.

Material	T [°C]	p CO_2 [bar]	q [mmol/g]	REF
PE-MCM-41/DEA	25	0.05	2.93	67
MCM-41/PEI	75	1	3.02	64
MCM-41/PEI	75	0.15	2.02	68
MCM-41/PEI	75	0.15*	2.97	68
KIT-6/PEI	75	1	3.07	65
MCM-41/PEI	75	1*	2.55	69
SBA-15/TEPA	75	1	3.93	70
SBA-17/DEA-TEPA	75	1	4	71
SBA-17/DEA-TEPA	75	1*	3.18	71
MCM-41/TEPA	35	1	5.02	72

Table 1.6. CO_2 adsorption capacity values (q) from literature at different temperature and pressure conditions. * indicates presence of water. [24]

From data reported in Table 1.6, the effect of the presence of water on the adsorption capacity of amino impregnated siliceous materials can be evaluated. The presence of water should increase the amine efficiency from 0.5 to 1.0 mol CO_2/mol N, because water molecules can act as a base, replacing an amine during the formation of carbamates (Equation 1.20). However, water can compete with carbon dioxide for the adsorption sites, causing a reduction of 20% in the adsorption capacity. [73] In addition, water can favour the release of amines, reducing the amount of amine available for chemisorption.

Since water may have both negative and positive effects on adsorption, Song et al. performed a adsorption experiments at different carbon dioxide and water ratio.[69] They found that a 1:1 concentration of carbon dioxide and water may be ideal to achieve the maximum equilibrium capacity.

Materials containing physically adsorbed amines are regenerated by blowing an inert gas and increasing the temperature in order to activate the desorption process. The degradation temperature depends widely on the type and the amount of the amine that can be used.

Concerning the kinetic, the adsorption rate of amino impregnated silicas is controlled by the gas diffusion inside the material, and thus is influenced by the pores diameter the support, together with the type and the amount of the amine: an excessive load of amine, or an amine with high steric hindrance, hampers the gas diffusion inside the pores, thus slowing the kinetics. [74]

Amines covalently bonded on siliceous supports

Trying to solve the main problem of the physically impregnated materials, that is mainly the possibility of amines release, new materials have been developed, in which the amino group is introduced by using amino silanes covalently bonded to the support. In this way hybrid organic-inorganic materials that can be potentially regenerated by numerous adsorption-desorption cycles are obtained.

Two different methods to obtain a covalent bond between the organic silane and the support are available. In the first approach, the siliceous support is first synthesized, and the anchorage of the silane is performed in a secondary step (post synthesis grafting method). In the second method, instead, the material is synthesized introducing the amino functionalities in one step (one-pot reactions) [75].

Post synthesis grafting method

In this method, the siliceous support is first synthesized, and then the amino groups are inserted by condensation between the organo-silane and the silanol groups on the surface, forming Si-O-Si bonds. Trialkoxysilanes are typically used to create as many bond with the silica surface as possible.

In Figure 1.13 a general scheme of the post synthesis grafting method is reported.

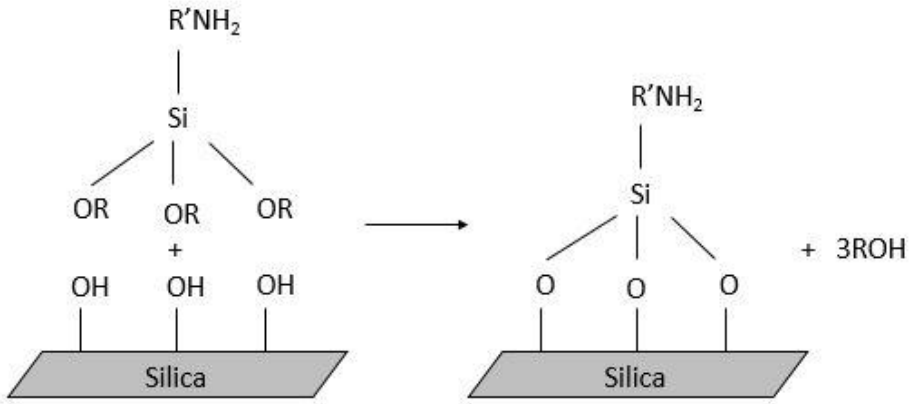

Figure 1.13. Schematic representation of post synthesis grafting reaction.

The organic loading achieved from the reaction between the organosilanes and the silica support is limited by the specific surface area and the number of accessible silanol groups. The density of SiOH groups on the silica surface depends on the synthesis method, but it is generally between 1 and 5 OH groups/nm^2.

Nitrogen content of supported amines is an important factor that influences the CO_2 capture capacity: for a high capture efficiency, a maximum amount of accessible primary and secondary amines should be present. The highest number of amines in a commercially available silane is 3, as for example in 3-[2-(2-aminoethyl) aminoethyl] aminopropyltrimethoxysilane (PAPTS). Other amino silanes widely used in literature are 3-aminopropyltriethoxysilane (APTS) and 3-(2-aminoethyl) aminopropyltrimethoxysilane (EAPTS), containing respectively 1 and 2 amino groups per chain. Also other amino silane, such as 3-(methyl)aminopropyltrimethoxysilane (MAPS), 3-(dimethyl)aminopropyltrimethoxysilane (DMAPS) and 3-(phenyl)aminopropyltrimethoxysilane (PAPS) are used in literature for the post synthesis grafting of siliceous supports. The parameters that must be considered synthesizing this hybrid organic-inorganic materials are the

proximity of the amino groups (as described before two amino groups are needed to capture a CO_2 molecule in anhydrous conditions) and pores volume after the functionalization, that influences the propagation rate of the carbon dioxide molecules. In the literature, different studies regarding CO_2 adsorption on silica grafted with APTS, EAPTS and PAPTS are present. However, these studies are not easily comparable because of the different amount of amine, the siliceous support and operative conditions (pressure and temperature). In Table 1.7 the adsorption capacities of some post-synthesis grafted silicas reported in the literature are summarized.

Material	T [°C]	p CO_2 [bar]	q [mmol/g]	REF
SBA-15/APTS	25	0.1	2.01	76
SBA-15/APTS	25	0.1*	2.01	76
SBA-15/APTS	60	0.15	0.52	77
SBA-15/APTS	60	0.15	0.25	78
SBA-15/APTS	25	0.04	0.33	79
SBA-15/APTS	25	0.04*	0.36	79
SBA-12/APTS	25	0.1	1.04	63
HMS/APTS	20	0.9	1.59	71
Davison62/APTS	27	1	0.41	81
Davison62/APTS	27	1*	0.93	81
MCM-48/APTS	25	0.05	1.14	82
MCM-48/APTS	25	1	0.8	83
PE-MCM-41/APTS	25	0.05	2.05	80
SBA-15/EAPTS	22	0.15	0.57	84
SBA-15/EAPTS	30	0.1*	0.79	85
SBA-15/EAPTS	60	0.15	0.87	77
SBA-15/EAPTS	60	0.15*	0.65	78
SBA-16/EAPTS	27	1	0.8	86
SBA-16/EAPTS	60	0.15	0.59	87
SBA-15/PAPTS	60	0.15	1.1	77
SBA-15/PAPTS	60	0.15	1.36	78
HMS/PAPTS	25	0.9	1.34	88
PE-MCM-41/PAPTS	25	0.05	2.65	89

Table 1.7. CO_2 adsorption capacity values (q) from literature of post synthesis grafted silica at different temperature and pressure conditions. * indicates presence of water. [24]

From Table 1.7 it can be noted that the highest reported equilibrium CO_2 at modest CO_2 partial pressures (≤0.15 bar) were 2.05 mmol/g for APTS (on pore-expanded MCM-41 support), 0.87 mmol/g for EAPTS (on SBA-15 silica support) and 2.65 mmol/g for PAPTS (on pore-expanded MCM-41 support). In general, materials functionalized with PAPTS show the highest adsorbent capacity, due to the higher amount of nitrogen present in the samples.

Concerning the adsorption capacity in presence of water, the amine efficiency should increase from 0.5 to 1.0 mol CO_2/ mol N, since water acts as a base (replacing one amino group) and helps the formation of carbamates. However, in literature, conflicting data are reported: some studies as that of Yogo et al. show that in the presence or absence of water the CO_2 adsorption capacity is comparable [90], while in other cases adsorption capacity value can increase by 15% in the presence of water.

Concerning the adsorption rate, achieving equilibrium is quite fast (< 60 min, unlike materials obtained through impregnation) and this makes them promising for practical applications. However, the real application is still hampered by the low adsorption capacity at low pressure and low selectivity towards CO_2 in the presence of other gases such as nitrogen [75].

One-pot method

The second approach to obtain a covalent bond between silane and support is the direct synthesis, in which the co-condensation of precursors (in general tetralkoxysilanes) occurs in presence of an organic structure-directing agent, which ensures the ordered mesoporous structure of the material [75]. The surfactant is finally removed by acid extraction.

Different studies on the use APTS to functionalize a siliceous material by one-pot method are present in literature, but no one refers to EAPTS and PAPTS.

One-pot method is advantageous respect to the post synthesis grafting method as it allow introducing more amine groups. In addition, since the organic functionalities are directly introduced in the formation of the silica matrix, pore blocking is not an issue. Finally, the organic chains are generally more homogeneously distributed with respect to materials synthesized with post synthesis grafting process. However, during the synthesis procedures, acid environment is used, promoting the protonation of the amino groups, which become not suitable to react with CO_2 [75].

References

[1] IPCC Climate Change 2007: Synthesis Report.

[2] https://www.ncdc.noaa.gov

[3] https://climate.nasa.gov

[4] S. Levitus, J. I. Antonov, T. P. Boyer, R. A. Locarnini, H. E. Garcia and A. V. Mishonov, *Geophys. Res. Lett*., **2009**, 36, 7, 1-5.

[5] http://nsidc.org

[6] J.A. Church, and N.J. White, *Surveys in Geophysics*, **2006**, 32, 4-5, 585-602.

[7] J.M. Melillo, T. Richmond, G.W. Yohe, *Eds*, **2014**, 841.

[8] https://epa.gov

[9] http://www.environment.gov.au

[9] IPCC, Climate Change 2014: Synthesis Report.

[10] G.A. Schmidt, R. Ruedy, R. L. Miller; A. A. Lacis, *J. Geophys. Res.*, **2010**, 115, 1-6.

[11] http://esrl.noaa.gov

[12] R. Revelle, H. E. Suesses, *Tellus* , **1957**, 9, 1, 18-27.

[13] United Nations Framework Convention on Climate Change, 1992.

[14] http://unfccc.int

[15] http://www.eea.europa.eu

[16] http://www.consilium.europa.eu

[17] http://www.un.org/sustainabledevelopment/cop21/

[18] http://cdiac.ornl.gov

[19] http://www.epoca-project.eu

[20] M. E. Boot-Handford, J. C. Abanades E. J. Anthony M. J. Blunt S. Brandani, N. Mac Dowell, J. R. Fernàndez, M.-C. Ferrari, R. Gross, J. P. Hallett, R. S. Haszeldine, P. Heptonstall, A. Lyngfelt, Z. Makuch, E. Mangano, R. T. J. Porter, M. Pourkashanian, G. T. Rochelle, N. Shah, J. G. Yao and P. S. Fennell, *Energy Environ. Sci*, **2014**, 7, 130.

[21] H. Herzog, D. Golomb, *Encyclopedia Energy*, **2004**, 1, 1–11.

[22] B. P. Spigarelli, S. K. Kawatra, *Journal o CO_2 Utilization*, **2013**, 1, 69-87.

[23] S. Burt, A. Baxter, L. Baxter, "Cryogenic CO_2 Capture to Control Climate Change Emissions", *Conference on Clean Coal & Fuel Systems*, **2009**.

[24] S. Choi, J. H. Drese, C, W. Jones, *ChemSusChem*, **2009**, 2, 796-854.

[25] D. Barthomeuf, *J. Phys. Chem*., **1984**, 88, 42.

[26] R. V. Siriwardane, M. S. Shen, E. P. Fisher, *Energy Fuels*, **2005**, 19, 1153.

[27] R. V. Siriwardane, M. S. Shen, E. P. Fisher, *Energy Fuels*, **2003**, 17, 571.

[28] J. A. Michelena, G. Peeters, E. F. Vansant, P. De Bievre, *Recl. Trav. Chim. Pays-Bas*, **1977**, 96, 121.

[29] E. Diaz, E. Munoz, A. Vega, S. Ordonez, *Ind. Eng. Chem. Res*., **2008**, 47, 412.

[30] L. Bertsch, H. W. Habgood, *J. Phys. Chem*., **1963**, 67, 1621.

[31] B. K. Na, K. K. Koo, H. M. Eum, H. Lee, H. K. Song, *Korean J. Chem. Eng*., **2001**, 18, 220.

[32] Y. X. Wang, Y. P. Zhou, C. M. Liu, L. Zhou, *Colloids Surf. A*, **2008**, 322, 14.

[33] R. V. Siriwardane, M. S. Shen, E. P. Fisher, J. A. Poston, *Energy Fuels*, **2001**, 15, 279.

[34] C. Pevida, M. G. Plaza, B. Arias, H. Fermoso, F. Rubiera, J. J. Pis, *Appl. Sur. Sci*., **2008**, 254, 7165.

[35] S. Sircar, T. C. Golden, M. B. Rao, *Carbon*, **1996**, 34, 1.

[36] J. A. Menèndez, J. Phillips, B. Xia, L. R. Radovic, *Langmuir*, **1996**, 12, 4404.

[37] J.A. Mason, K. Sumida, Z.R. Herm, R. Krishna, J.R. Long, *Energy Environ. Sci.*, **2011**, 4, 3030.

[38] S. R. Caskey, A. G. Wong-Foy, A. J. Matzger, *J. Am. Chem. Soc.* **2008**, 130, 10870. [39] J. Kim, S-T. Yang, S.B. Choi, J. Sim, J. Kim, W-S. Ahn, *J. Mater. Chem*., **2011**, 21, 3070.

[39] S.-J. Bao, R. Krishna, Y.-B. He, J.-S. Qin, Z.-M. Su, S.-L. Li, W. Xie, D.-Y. Du, W.-W. He, S.-R. Zhang, Y.-Q. Lan, *J. Mate. Chem. A*, **2015**, 3, 7361.

[40] Q.-G. Zhai, X. Bu, C. Mao, X. Zhao, P. Feng, *J. Am. Chem. Soc*., **2016**, 138, 2524.

[41] K. Sumida, D. L. Rogow, J. A. Mason, T. M. McDonald, E. D. Bloch, Z. R. Herm, T-H. Bae, J. R. Long, *Chem. Rev*., **2012**, 112, 724–781.

[42] B. Arstad, H. Fjellvag, K. O. Kongshaug, O. Swang, R. Blom, *Adsorption*, **2008**, 14, 755.

[43] S. F. Wu, T. H. Beum, J. I. Yang, J. N. Kim, *Ind. Eng. Chem. Res*., **2007**, 46, 24.

[44] K. Kuramoto, S. Fujimoto, A. Morita, S. Shibano, Y. Suzuki, H. Hatano, S. Y. Lin, M. Harada, T. Takarada, *Ind. Eng. Chem. Res*., **2003**, 42, 975.

[45] J. A. Satrio, B. H. Shanks, T. D. Wheelock, *Ind. Eng. Chem. Res*., **2005**, 44, 3901.

[46] Z. S. Li, N. S. Cai, Y. Y. Huang, *Ind. Eng. Chem. Res*., **2006**, 45, 1911.

[47] R. Barker, *J. Appl. Chem. Biotechnol*., **1973**, 23, 733.

[48] R. Barker, *J. Appl. Chem. Biotechnol*., **1974**, 24, 221.

[49] Z. Yong, A. E. Rodrigues, *Energy Convers. Manage*, **2002**, 43, 1865.

[50] Y. Ding, E. Alpay, *Chem. Engi. Sci*., **2000**, 55, 3461.

[51] Y. Ding, E. Alpay, *Process Saf. Environ. Prot*., **2001**, 79, 45.

[52] H. T. J. Reijers, S. E. A. Valster-Schiermeier, P. D. Cobden, R. W. van den Brink, *Ind. Eng. Chem. Res*., **2006**, 45, 2522.

[53] Z. Yong, V. Mata, A. E. Rodrigues, *Sep. Purif. Rev*., **2002**, 26, 195.

[54] Z. Yong, V. Mata, A. E. Rodriguez, *Ind. Eng. Chem. Res*. **2001**, 40, 204.

[55] C. Yu, C. Huang, C, Tan, *Aerosol and Air Quality Reaserch*, **2012**, 12,745-769.

[56] M. Caplow, *J. Am. Chem. Soc*., **1968**, 90, 6795.

[57] M.W. Hahn, M. Steib, A. Jentys, J. A. Lercher, *J. Phys. Chem. C*, **2015**, 119, 4126−4135.

[58] Chun-Jae Yoo, Li-Chen Lee, and Christopher W. Jones, *Langmuir*, **2015**, 31, 13350−13360.

[59] A. Danon, P.C. Stair, E.Weitz, *J. Phys. Chem. C*, **2011**, 115, 23, 11540−11549.

[60] P. D. Vaidya, E. Y. Kenig, *Ind. Eng. Chem. Res.*, **2007**, 30, 1467.

[61] N. Hedin, L. Chen, A. Laaksonen, *Nanoscale*, **2010**, 2, 1819–1841.

[62] T. Tsuda, T. Fujiwara, Y. Taketani, T. Saegusa, *Chem. Lett.*, **1992**, 2161.

[63] C.O.B. Leal, C. Ovalles, J.J. Garcia, Y. Espidel, *Inorg. Chem. Acta*, **1995**, 240, 183.

[64] X. C. Xu, C. S. Song, J. M. Andresen, B. G. Miller, A. W. Scaroni, *Energy Fuels*, **2002**, 16, 1463.

[65] W. J. Son, J. S. Choi, W. S. Ahn, *Microporous Mesoporous Mater*., **2008**, 113, 31.

[66] M. B. Yue, Y. Chun, Y. Cao, X. Dong, J. H. Zhu, *Adv. Funct. Mater*, **2006**, 16, 1717.

[67] R. S. Franchi, P. J. E. Harlick, A. Sayari, *Ind. Eng. Chem. Res.*, **2005**, 44, 8007.

[68] X. C. Xu, C. S. Song, B. G. Miller, A. W. Scaroni, *Ind. Eng. Chem. Res.*, **2005**, 44, 8113.

[69] X. C. Xu, C. S. Song, B. G. Miller, A. W. Scaroni, *Fuel Process. Technol.*, **2005**, 86, 1457.

[70] M. B. Yue, Y. Chun, Y. Cao, X. Dong, J. H. Zhu, *Adv. Funct. Mater*., **2006**, 16, 1717.

[71] M. B. Yue, L. B. Sun, Y. Cao, Z. J. Wang, Y. Wang, Q. Yu, J. H. Zhu, *Microporous Mesoporous Mater*., **2008**, 114, 74.

[72] M. B. Yue, L. B. Sun, Y. Cao, Y. Wang, Z. J. Wang, J. H. Zhu, *Chem. Europ. J.*, **2008**, 14, 3442.

[73] M. B. Yue, Y. Chun, Y. Cao, X. Dong, J. H. Zhu, *Adv. Funct. Mater*., **2006**, 16, 1717.

[74] G. P. Curran, C. E. Fink, E. Gorin, *Adv. Chem. Ser*, **1967**, 31, 141.

[75] C. Yu, C. Huang, C, Tan, *Aerosol and Air Quality Research*, **2012**, 12, 745-769.

[76] M. L. Gray, Y. Soong, K. J. Champagne, H. Pennline, J. Baltrus, *Int. J. Environ. Technol. Manage.*, **2004**, 4, 82.

[77] N. Hiyoshi, K. Yogo, T. Yashima, *Chem. Lett*., **2004**, 33, 510.

[78] N. Hiyoshi, K. Yogo, T. Yashima, *Microporous Mesoporous Mater*., **2005**, 84, 357.

[79] A. C. C. Chang, S. S. C. Chuang, M. Gray, Y. Soong, *Energy Fuels*, **2003**, 17, 468.

[80] V. Zelenak, D. Halamova, L. Gaberova, E. Bloch, P. Llewellyn, *Microporous Mesoporous Mater.*, **2008**, 116, 358.

[81] G. P. Knowles, J. V. Graham, S. W. Delaney, A. L. Chaffee, *Fuel Process. Technol.*, **2005**, 86, 1435.

[82] H. Y. Huang, R. T. Yang, D. Chinn, C. L. Munson, *Ind. Eng. Chem. Res*., **2003**, 42, 2427.

[83] S. Kim, J. Ida, V. V. Guliants, J. Y. S. Lin, *J. Phys. Chem. B*, **2005**, 109, 6287.

[84] F. Zheng, D. N. Tran, B. J. Busche, G. E. Fryxell, R. S. Addleman, T. S. Zemanian, C. L. Aardahl, *Ind. Eng. Chem. Res*., **2005**, 44, 3099.

[85] R. A. Khatri, S. S. C. Chuang, Y. Soong, M. Gray, *Ind. Eng. Chem. Res*., **2005**, 44, 3702.

[86] C. Knofel, J. Descarpentries, A. Benzaouia, V. Zelenak, S. Mornet, P. L. Llewellyn, V. Hornebecq, *Microporous Mesoporous Mater*., **2007**, 99, 79.

[87] J. Wei, J. Shi, H. Pan, W. Zhao, Q. Ye, Y. Shi, *Microporous Mesoporous Mater.*, **2008**, 116, 394.

[88] G. P. Knowles, S. W. Delaney, A. L. Chaffee, *Ind. Eng. Chem. Res*., **2006**, 45, 2626.

[89] P. J. E. Harlick, A. Sayari, *Ind. Eng. Chem. Res*., **2007**, 46, 446.

[90] N. Hiyoshi, K. Yogo, T. Yashima, *Chemistry Letters*, **2004**, 33, 510–511.

Chapter 2

Outline of the Thesis

In this PhD thesis, different types of hybrid organic inorganic materials were studied as solid sorbents for the carbon dioxide capture, in order to give additional hints to the comprehension of phenomena playing an important role in CO_2 adsorption processes. In addition, the possible use of silica-based materials as catalyst for the carbon dioxide transformation into more useful products was studied. The different aspects considered are depicted in Figure 2.1.

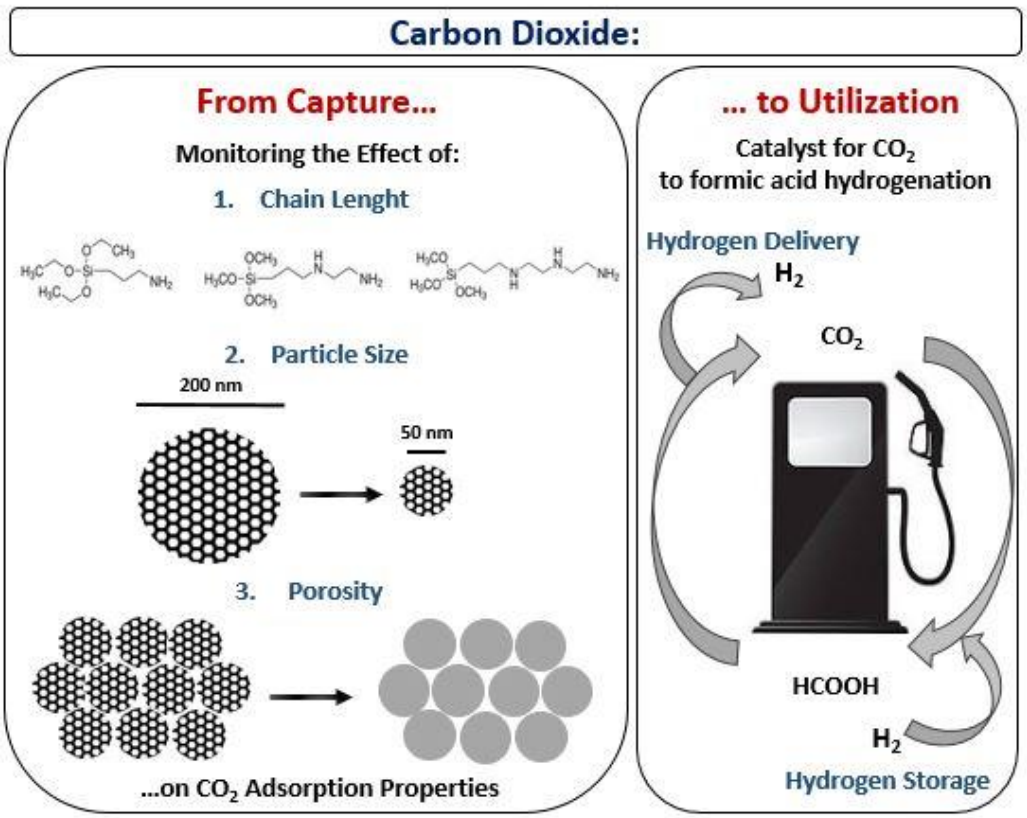

Figure 2.1. Schematic representation of the aspects related to the CO_2 capture and utilization investigated in this PhD thesis.

In the first part of the PhD, hybrid organic-inorganic SBA-15 silicas functionalized with variable amount of amino groups were studied aiming to evaluate the influence of the different basic species on CO_2 capture ability (Chapter 3). The support was chosen on the basis of its interesting performances reported in the literature.

Three different amino-silane species, with increasing amount of amino groups per chain, were used: 3-aminopropyltriethoxysilane (APTS), 3-(2-aminoethyl) aminopropyltrimethoxysilane (EAPTS) and 3-[2-(2-aminoethyl)aminoethyl] aminopropyltrimethoxysilane (PAPTS).

The obtained hybrid materials were characterized by a multidisciplinary experimental and computational approach, in order to clarify their structural, textural and surface properties. In addition, the interactions occurring on the surface of the different hybrid organic-inorganic materials were investigated by coupling IR and SS-NMR spectroscopy. Particular attention in this context was devoted to the study of the interactions between amine and surface silanol groups aiming to give additional information concerning the evaluation of the mobility of the organic chains on the SBA-15 surface. Despite this parameter strongly influences the adsorption performances, a detailed study on the interaction between amino groups and silanols is not reported in literature. Moreover, the carbon dioxide adsorption process was studied by different experimental techniques, in order to obtain both qualitative and quantitative information. In this approach, techniques classically used for the study of carbon dioxide adsorption have been compared with new ones, such as the Zero Length Column Chromathography. This technique allows a quantitative analysis for the determination of the CO_2 adsorption of hybrid organic-inorganic samples, and represents a relevant screening method for prototype adsorbers, since it requires small amount of samples and very short time of analysis.

After assessing the effect of the basic species of the hybrid materials on CO_2 adsorption, it was decided to study the influence of siliceous support properties on the adsorption process.

In the literature, many investigations concerning different types of solid supports for the heterogeneization of basic species are reported. Unfortunately, these studies are conducted at different experimental conditions (*i.e.* different temperature, pressure, adsorption gas composition, presence of water, etc…), and therefore it is difficult to compare them. For this reason, silica-based materials with different structure, morphology and particle size were selected and tested in the same experimental conditions, aiming to understand the effect of their physico-chemical properties on the CO_2 adsorption. In order to evaluate the effect of the siliceous support alone, hereafter all the materials were functionalized with PAPTS species. This silane was chosen on the basis of the results obtained on SBA-15 functionalized silica.

MCM-41 silica-based materials with different particle diameter, passing from micrometric to nanometric scale, were considered, in order to study the size effect of the support on the adsorption properties (Chapter 4). The study of nanometric MCM-41 silica as solid sorbent for CO_2 capture is an aspect of absolute novelty, as well as the comparison of silica supports with different particle size.

In this chapter, particular attention has also been given to the qualitative and semi-quantitative distinction between CO_2 physical and chemical adsorption processes on the different MCM-41-based hybrid samples, by coupling for the first time FTIR and SS-NMR spectroscopies.

Moreover, the temperature dependence of MCM-41 based hybrid materials has been evaluated by studying the CO_2 adsorption process at temperatures between 20°C and 90°C from both qualitative and quantitative point of view.

Subsequently, the effect of the porosity was evaluated by using as adsorbent a non-porous material (Stöber silica) and comparing the obtained results with those of MCM-41-based materials (Chapter 5). MCM-41 silica was chosen as it is characterized by micrometric dimensions, comparable to the Stober silica particle size. The idea of testing the CO_2 adsorption properties of a non-porous material arises from the need to find solids adsorbents cheaper than mesoporous ordered materials based sorbents, widely studied in the literature. Until now, among other siliceous

materials, Stöber silica has never been tested as solid sorbent for the carbon dioxide capture.

The adsorption properties of the hybrid materials were studied during the stage at the University of Edinburgh's School of Engineering under the supervision of Dr. Enzo Mangano and Prof. Stefano Brandani.

Finally, a study on the possible use of silica-based materials as catalyst for the carbon dioxide transformation into more useful products is given in Chapter 6. More in detail, heterogeneous Cu-based catalyst supported on SiO_2 have been studied as for the promotion of hydrogenation reaction of CO_2 to formic acid. This reaction is interesting not only as it transforms CO_2 into a product widely used in many industrial fields, but also because is a promising hydrogen storage technique.

In the literature, the mainly used catalysts for the hydrogenation-dehydrogenation reactions are expensive homogeneous complexes or heterogeneous catalyst based on noble metals. Therefore, in this thesis, it was decided to study cheaper heterogeneous copper-based catalysts.

The catalysts were fully characterized by using different experimental techniques, especially focusing con the copper dispersion and oxidation state. Finally, the catalytic properties of the catalysts have been studied in collaboration with Dr. Nicola Scotti and Dr. Nicoletta Ravasio from the Institute of Molecular Science and Technologies of CNR.

Chapter 3

CO_2 Adsorption on Organo-modified SBA-15 Silicas: Effect of the Basic Surface Groups on the Adsorption Performances

Introduction

Ordered porous siliceous materials such as SBA-12, SBA-15, SBA-16, MCM-41, MCM-48, KIT-6, mesoporous silica spheres and mesocellular silica foams have been largely investigated as solid sorbent for CO_2 capture[1]. In fact, these materials are good candidates for CO_2 capture due to their structural and textural properties, such as high specific surface area, large pore size and high pore volume. All these properties enable a good dispersion of basic amino-groups on the surface, which should be incorporated in order to react chemically with CO_2, thus increasing the adsorption capacity [2]. Compared to the other mesoporous materials, SBA-15 was found to be one of the most interesting substrates for CO_2 capture, primarily thanks to its large pore diameter and high pore volume [3]. Moreover, the intra-wall pores of the SBA-15 silica form a continuous network that connects adjoining channels, which favour the mass transfer during the adsorption. For these reasons, SBA-15 has been widely studied as support for CO_2 capture. Even if several studies in the literature reported the use of SBA-15 containing basic amino-groups [4], the CO_2 capture performances of these materials are difficult to be compared, because in many cases different conditions of pressure and temperature have been adopted. Therefore, in this PhD work, the following post combustion conditions, *i.e.* 35 °C, CO_2 partial pressure = 0.1 bar, have been selected for all samples, in order to make the obtained results fully comparable.

Specifically, the study of SBA-15 silicas, functionalized with increasing amounts of amino groups, as supporting material for the carbon dioxide capture, is reported in this Chapter especially focusing on the influence of basic surface groups on the CO_2 adsorption properties.

Three different amino-silane species were introduced on SBA-15 silica in order to introduce basic amino groups (Fig. 3.1): 3-aminopropyltriethoxysilane (APTS), 3-(2-aminoethyl) aminopropyltrimethoxysilane (EAPTS) and 3-[2-(2-aminoethyl)aminoethyl] aminopropyltrimethoxysilane (PAPTS).

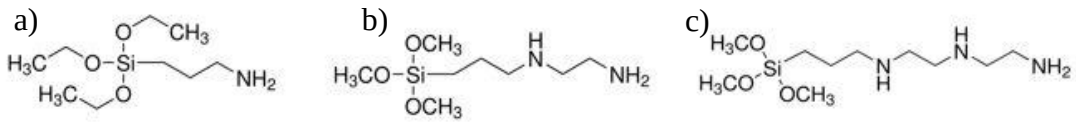

Figure 3.1. Amino-silane species introduced on SBA-15 silica: a) APTS, b) EAPTS and c) PAPTS.

The introduction of amino-silane species occurred by both post-synthesis grafting method. This method was preferred compared to the one-pot procedure, in order to avoid the protonation of the amino groups, making them not suitable to react with CO_2 (see Paragraph 1.6.2).

In the following Paragraphs will be described:

- the starting point from recent literature and the elements of novelty of this work (Paragraph 3.1);
- the synthetic procedures of the SBA-15 and derived organic-inorganic hybrid materials (Paragraphs 3.2 and 3.3);
- the physico-chemical properties of the mesoporous silica SBA-15 and related functionalized solids (Paragraph 3.4);
- a multidisciplinary study of the CO_2 adsorption process on the hybrid materials (Paragraphs 3.5 and 3.6).

3.1 From the Starting Point to the Goals

The CO_2 adsorption processes on SBA-15 grafted sorbents is widely described in literature for the reasons remarked in the introduction. For example, Wang et al. grafted SBA-15 silica with 3-aminopropyltrimethoxysilane in order to obtain an adsorbent with CO_2 adsorption capacity of ca. 1.59 mol/kg at 25 °C and 0.15 atm[5], while Chang et al. used 3-trimethoxysilylpropyl diethylenetriamine as a grafting agent on SBA-15 silica, obtaining a CO_2 uptake of 2.41 mol/kg at 60 °C and 0.15 atm. [6]

Even though several other studies on SBA-15 grafted materials containing different amount of basic species are reported in literature, the CO_2 capture performances of these materials are difficult to be compared because in many cases different conditions of pressure and temperature have been adopted.

Recently, Calleja et al. studied the effect of the distribution of the amino groups contained in the hybrid SBA-15 based materials. [7] In their work they compared SBA-15 functionalized with amino silanes with different chain lengths (*i.e.* 3-aminopropyltrimethoxysilane (APTS), 3-(2-aminoethyl)aminopropyltrimethoxysilane (EAPTS) and 3-[2-(2-aminoethyl)aminoethyl]aminopropyltrimethoxysilane (PAPTS)), containing different amount of organic compounds. They found a dissimilar behaviour in CO_2 capture of their materials, related to the specific position of amino groups in the siliceous structure of SBA-15 and to the amount of amino groups present in the adsorbers.

Also Yoo et al. compared the CO_2 adsorption properties of SBA-15 materials grafted with APTS, EAPTS and PAPTS, with low loading of silane adsorbents (about 0.45 mmol silane per g). Their work was focused on the determination of the CO_2 adsorption mechanism. In particular, they proposed the occurrence of an intramolecular mechanism for carbon dioxide adsorption on EAPTS and PAPTS chains, whereas for samples grafted with APTS (*i.e.* the shorter silane species,

containing only one amino group) an intermolecular mechanism was proposed. The role of silanol groups in CO_2 interactions was also explained. [8]

Despite the large number of studies on the carbon dioxide adsorption phenomenon on SBA-15 grafted materials are reported in literature, some information are missing. On these basis, the purpose of this chapter is to provide additional hints for understanding the carbon dioxide adsorption phenomenon from the physico-chemical point of view.

The mobility of organic chains anchored to the surface of SBA-15 is a very important aspect for the comprehension of the reactivity of these systems toward carbon dioxide. In fact, the mobility is related to the interaction of the organic chains with the surface silanols, which plays a crucial role in the adsorption mechanism, as mentioned before. This aspect, however, is not investigated in literature. For this reason, in this PhD thesis, the mobility of the organic chains is studied for the first time by using SS-NMR spectroscopy. To corroborate this aspect, some computational models are also proposed.

Moreover, in this Chapter a coupling of IR spectroscopy of adsorbed CO_2 with a non-conventional solid state NMR spectroscopy of adsorbed $^{13}CO_2$ is applied for the first time to monitor the interactions of the basic probe with the surface of hybrid samples.

Another point of novelty is the comparison of classical volumetric measurements (already present in literature) with those derived by Zero Length Column analysis. This technique is a new type of screening analysis for hybrid organic-inorganic adsorbents, which requires low amount of sample and short time of analysis. This specific comparison has never been proposed in the literature and allowed to propose the ZLC method as a valid rapid screening of the materials capacity to adsorb CO_2.

3.2 SBA-15 Silica

Santa Barbara Amorphous silica n ° 15 (SBA-15) is a mesoporous material synthesized for the first time in 1998 at the University of Santa Barbara (California). [9] SBA-15 silica presents a highly ordered structure, high specific surface area (about 690-1040 m^2/g) and a large pore size. This material is characterized by the presence of cylindrical mesopores with an ordered hexagonal arrangement. The size of the mesopores varies between 6.5 and 15 nm, while the thickness of the pore walls is between 3.1 and 4.8 nm[10, 11]. In the SBA-15 structure, are also present pores with a 1-2 nm diameter that interconnect the adjacent mesoporous channels. [12]
The structure of the SBA-15 silica is represented in Figure 3.2.

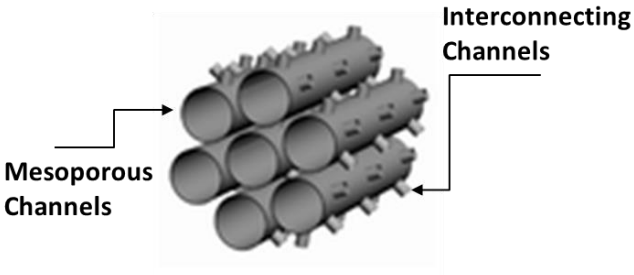

Figure 3.2. Schematic view of the structure of SBA-15 silica.[13]

Another important property of SBA-15 silica are the thermal and hydrothermal stability: Zhang et al. reported that this material, after a steam exposition at 600°C for 24 h, maintains its hexagonal structure, without undergoing a complete amorphization.[14] All these properties render SBA-15 silica interesting for different technological applications, such as drug delivery[15], catalysis[156], seizure of organic pollutants [17] and, as studied in the frame of this PhD thesis, CCS technologies.

3.2.1 Synthesis Method of SBA-15 Silica

The synthesis procedure of SBA-15 silica occurs by sol-gel process. With this methodology, the silica is formed through condensation of an inorganic precursor (*i.e.* tetraethyl orthosilicate) at low temperature (< 100°C). [18] In a typical sol-gel process, the alkoxide precursor is hydrolyzed to the corresponding hydroxide and a colloidal suspension (sol) is formed. After the sol preparation, condensation reactions are promoted to form the gel. Finally, further processing of the gel leads to materials in different forms, such as thin films, wet gel, aerogel, etc. [19]

The hydrolysis and condensation reactions that occur in the sol-gel process to form a siliceous material are summarized below (R: ethyl group):

$$(OR)_3SiOR + H_2O \rightarrow (OR)_3SiOH + ROH \quad (3.1)$$

$$(OR)_3SiOH + (OR)_3SiOR \rightarrow (OR)_3Si\text{-}O\text{-}Si(OR)_3 + ROH \quad (3.2)$$

$$(OR)_3SiOH + (OR)_3SiOH \rightarrow (OR)_3Si\text{-}O\text{-}Si(OR)_3 + H_2O \quad (3.3)$$

Many factors (*i.e.* precursor, solvent, catalyst, pH, temperature, etc.) influence the hydrolysis and condensation rates, and consequently affect the structure of the gel network [19].

In order to obtain an ordered mesoporous structure by sol-gel technique, surfactant molecules, acting as templates, must be introduced during the synthesis. Numerous templates can be used to fabricate mesoporous structures (*i.e.* cationic, anionic, non-ionic and polymeric surfactants). All of these surfactants are bifunctional molecules containing hydrophilic head and hydrophobic tails. When the surfactant concentration is greater than the critical micellization concentration (CMC), the amphiphilic structure of the template is responsible of the formation of micelles [20].

In the synthesis of SBA-15 silica Pluronic P123 sufactant is used. This template consist of poly(ethylene oxide)–poly(propylene oxide)–poly(ethylene oxide) (PEO–PPO–PEO) copolymers. The surfactant is characterized by a terminal PEO segment, representing the hydrophilic shell, and a PPO part, that represent the hydrophobic

core.[21] In the micelle, the hydrophilic groups form the external part (corona), while the hydrophobic groups are in the centre (core).

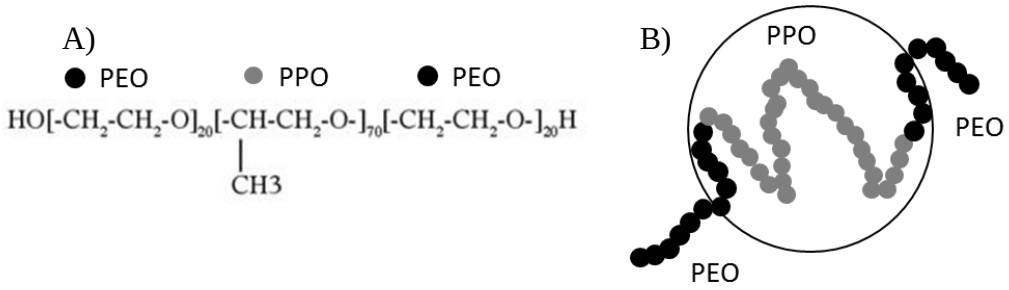

Figure 3.4. A) Schematic representation of Pluronic P123 and B) Schematic representation of the micelle formation in Pluronic P123.

The micelles in water are surrounded by a corona of hydrated polyethylene oxide chains protruding by about 1 nm from the average micelle surface. [22] When an isotropic micellar solution is formed, the repulsion between PEO chains of adjacent micelles keeps them to a distance of at least 3–4 nm, thus indicating that the micelles are well separated. Increasing the surfactant concentration, an intermicellar attraction arises from PEO parts of adjacent micelles. At a certain point, micelles interact strongly enough to form aggregates, which separate from the diluted solution. These aggregates can exist in different phases (*i.e.* cubic or hexagonal), depending on the temperature and the concentration of the surfactant in water. The phase diagram of the Pluronic P123 is reported in Figure 3.5.

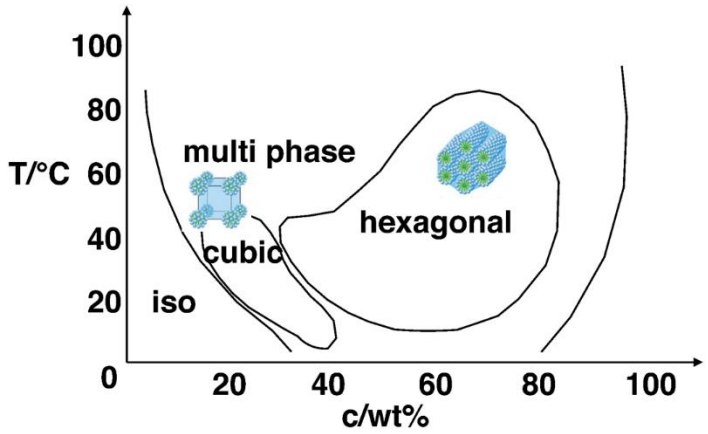

Figure 3.5. Phase diagram of Pluronic P123 in aqueous solution [23]

One proposed formation mechanism of SBA-15 silica is called liquid crystal templating mechanism. In this mechanism, the surfactant in solution forms lyotropic liquid crystal phase (LC). The inorganic precursor (*i.e.* tetraethyl orthosilicate) is condensed on the micelle rods of the preformed liquid crystalline phase. A subsequent polymerization of the inorganic precursors leads to the formation of an organic-inorganic mesostructure. In particular, an hexagonal array of surfactant micellar rods embedded in a silica matrix is formed. The following removal of the surfactant produces an open mesoporous framework.[24] In addition, it was proposed a different mechanism, in which the ordering of the surfactant molecule into hexagonal liquid crystal phase is influenced by the inorganic precursors, indicating that a "cooperative self-assembly" between the templates and the precursors occurs, yielding to the organized SBA-15 architecture [25].

The wall thickness of the materials formed at 35°C (about 4 nm), corresponds to the minimum distance between hydrated micelles in water. This effect supports the cooperative self-assembly mechanism, in which an impregnation of the intermicellar space by the silica precursors occurs. In addition, following this theory, the formation of 1-2 nm diameter porosity connecting the adjacent mesoporous channels is explained: these porosity are templated by the PEO chains that protrude from the micelle. [23]

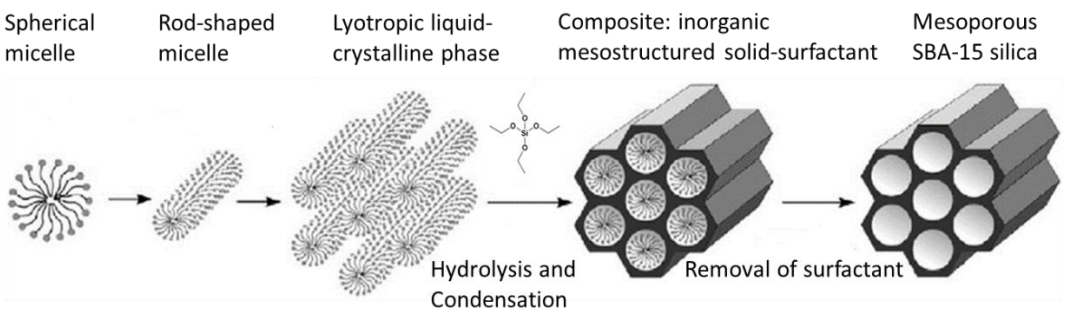

Figure 3.6. Scheme of SBA-15 formation according to cooperative self-assembly method. [24]

In this PhD thesis, SBA-15 was prepared by following the synthetic method of Zhao et al [9].

The mesoporous solid was then functionalized with basic amino-groups in order to make it chemically reactive toward carbon dioxide.

3.3 Materials Preparation

3.3.1 Synthesis of SBA-15 Silica

Pure SBA-15 silica was synthesized following the method reported by Zhao et al. [9] In detail, 4.0 g of Pluronic P123 triblock copolymer (Sigma Aldrich, 435465-250ML, Mn=5800 g/mol) was dissolved in 30 mL of deionized water in a thermostated bath at 35°C. The obtained gel was mixed with a Teflon rod and a mechanical stirrer for 24 h. After this time, 120 g of 2M HCl solution was added to the gel. 1 h later, 8.5 g of tetraethyl orthosilicate (TEOS, $Si(OC_2H_5)_4$, Sigma-Aldrich, 131903-25ML, M.W=208.33 g/mol) were added. Then, after 1 h, the gel was introduced in a Teflon cup of an autoclave (Anton PAAR 4748) and heated in an oven at 100°C for 24 h. After the hydrothermal treatment, samples were filtered, washed with deionized water and dried in an oven for 36 h at 120°C. Then the material was finally calcined under air flow (100 mL/min) at 550°C for 5 h (ramp rate:1°C/min) to remove the organic template.

3.3.2 Synthesis of Post-synthesis Hybrid Materials Based on SBA-15

Before the functionalization procedure, three aliquots of 1.0 g of SBA-15 silica were treated in vacuum at 200°C for 2 h in order to remove physisorbed water. After this treatment, the samples were kept under N_2 flow and then dispersed in 100 mL of anhydrous toluene containing the organo-silane, added drop-by-drop. In one case, 0.53 mL of 3-aminopropyltriethoxysilane (APTS, $H_2N(CH_2)_3Si(OCH_3)_3$, Sigma-Aldrich, M.W.= 221.37 g/mol) were added, and then the suspension was left for 20h at 50°C under magnetic stirring. After this time, the sample was filtered, the powder was washed with toluene and ethyl ether to remove the unreacted silane, and finally dried for 1 night at 80°C [25]. This sample was hereafter named A-SBA15. For the other two hybrid SBA-15 samples, 0.49mL of N-[3-(trimethoxysilyl)propyl]-ethylenediamine (EAPTS, $H_2N(CH_2)_2NH(CH_2)_3Si(OCH_3)_3$, Sigma-Aldrich, M.W.=222.36 g/mol) and 0.48 mL of N-[3-(trimethoxysilyl)propyl]-diethylenetriamine (PAPTS, $(H_2N(CH_2)_2NH(CH_2)_2NH(CH_2)_3Si(OCH_3)_3$, Sigma-Aldrich, M.W.=265.43 g/mol) were added. The same preparation protocol adopted for A-SBA-15 was followed for these samples. The obtained materials are hereafter named E-SBA-15 and P-SBA-15, respectively.

3.4 Physico-chemical Characterization

3.4.1 Structural and Textural Analysis

The structural properties of hybrid organic-inorganic SBA-15 samples prepared by post-synthesis grafting method were studied by XRD analysis (Figure 3.7).

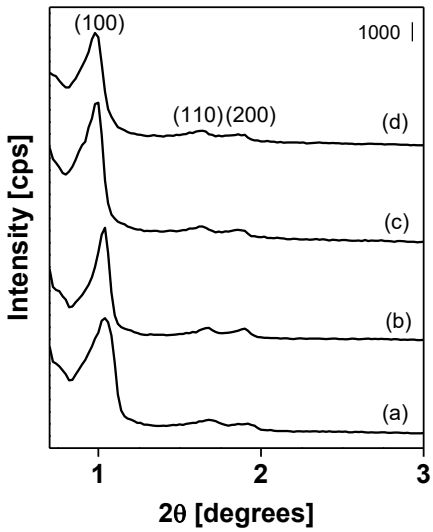

Figure 3.7. XRD pattern of pure SBA-15 material (curve a) and post-synthesis grafted samples: A-SBA-15 (curve b), E-SBA-15 (curve c) and P_SBA-15 (curve d). [26]

SBA-15 silica sample (Figure 3.7, curve a) shows Bragg reflections located at 0.9, 1.5 e 1.8° 2θ, corresponding to (100), (110) and (200) planes. These reflections are typical of hexagonally ordered mesoporous silica.[27] All post-synthesis grafted samples in Figure 3.7 show the same reflections of pure SBA-15, indicating that the process of grafting did not modify the ordered structure typical of this material.

In order to collect information on the textural properties of grafted and one-pot prepared samples, N_2 physisorption analysis at 77K was carried out. Nitrogen adsorption and desorption isotherms (Frame A) and the pore size distributions (Frame B) are reported in Figure 3.8.

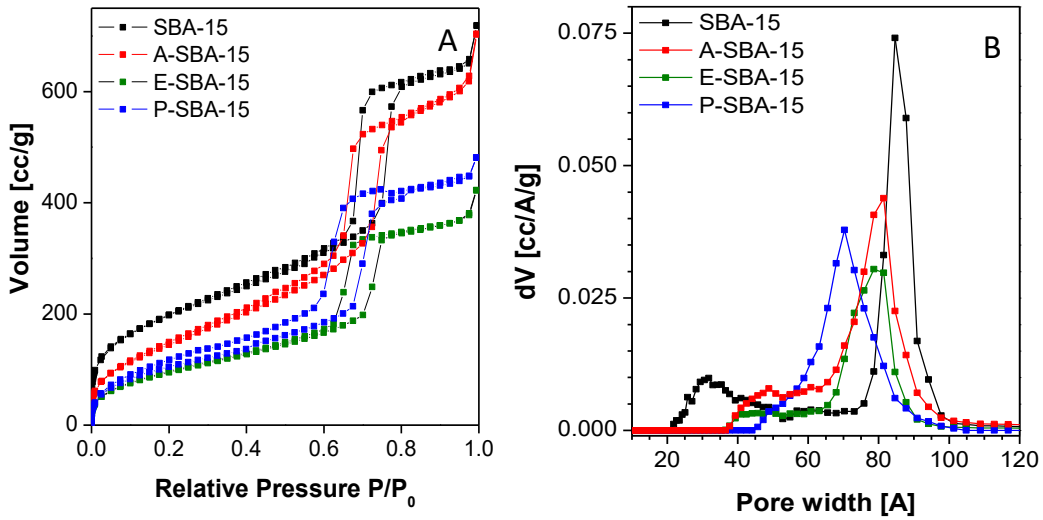

Figure 3.8. Frame A: N_2 adsorption–desorption isotherms at 77 K of functionalized SBA-15 samples prepared by grafting procedure. Frame B: Pore size distribution determined by N_2 physisorption at 77K applying NLDFT methods of SBA-15 silica and grafted samples. [26]

Pure SBA-15 silica sample (Figure 3.8, frame A) shows type IV adsorption isotherm based on the IUPAC classification, [28] typical of materials containing mesoporosity. Also the related hybrid samples show type IV adsorption isotherms. For all grafted samples an H1 hysteresis loop, typical of materials with cylindrical pore, can be observed. [28] The Brunauer–Emmett–Teller (BET) method was used to estimate the specific surface area (S.S.A.) of the solids. The pure SBA-15 silica shows a S.S.A. value of 720 m^2/g, whereas for the grafted silica samples a progressive decrease of S.S.A. was observed with increasing the silane chain length. In particular, the S.S.A values are 563, 360 and 236 m^2/g, respectively for A-SBA-15, E-SBA-15 and P-SBA-15 samples (Table 1). The reduction of specific surface area is attributed to the presence of the organic chains that limits the access to the pores: the longer is the length of the silane chain, the greater is the pore blocking effect.[29, 26] The pore size distribution (Figure 3.8, frame B) was determined by the NLDFT model using a kernel based on a cylindrical pore model related to the desorption branch of the isotherms.

SBA-15 sample presents two families of pores: the first one with a maximum centred at ca. 85 Å corresponding to the mesopores, and the second with dimensions between 20 and 40 Å, attributed to the pores interconnecting adjacent mesopores. [31]
After the post-synthesis grafting procedure, for A-SBA-15 sample, the pore located at 85 Å shifts to ca. 80 Å. In addition, the family of smaller pores located between 20 and 40 Å disappears, when a new family of pores with larger dimension (40-60 Å) appears. The same behaviour is observable for E-SBA-15 and P-SBA-15 samples, even if the pores located at 85 Å are shifted at 80 and 70 Å respectively, and the pores with dimension between 40 and 60 Å are less numerous than in A-SBA-15 sample.[26] Pore volume values of the prepared samples are reported in Table 3.1.

Sample	**S. S. A. [m^2/g]**	**V_p [cc/g]**
SBA-15	720	0.98
A-SBA-15	563	0.94
E-SBA-15	360	0.57
P-SBA-15	236	0.41

Table 3.1. Specific surface area and total pore volume values of SBA-15 and hybrid related samples.

The concentration of nitrogen introduced in the samples by the different preparation procedures was estimated with elemental analysis. In addition, the concentration of silane molecules in the hybrid samples was also calculated by dividing the total amine loading by the number of nitrogen atoms in each silane chain (1, 2 and 3 respectively for A-SBA-15, E-SBA-15 and P-SBA-15 samples). These data are reported in Table 3.2.

Sample	Conc. N [mmol/g]	Conc. Silane [mmol/g]
A-SBA-15	1.05	1.05
E-SBA-15	2.60	1.30
P-SBA-15	3.50	1.16

Table 3.2. N_2 content estimed with elemental analysis and silane concentration of hybrid materials.

In Table 3.2 is possible to observe that the silane concentration is similar for all hybrid samples (about 1 mmol/g). This fact reflects the introduction of the same molar concentration of organic species (Paragraph 3.2). This data also suggests that steric hindrance problems between the organic chains of the silane are not significant.

3.4.2 Surface Properties of SBA-15 Hybrid Materials

In order to estimate the concentration of surface silanol species, thermogravimetric analysis (TGA) of SBA-15 sample was performed (Figure 3.9).

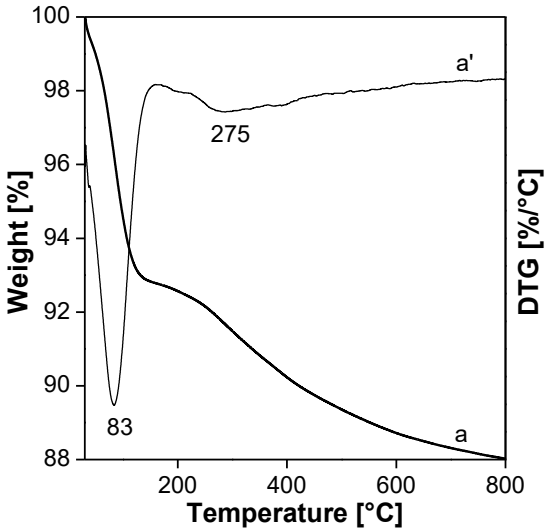

Figure 3.9. Thermogravimetric analysis of SBA-15 sample (curve a) and relative derivative (curve a'). Analysis conditions: Ar flow: 20ml/ min, heating ramp: 5 ° C/min.

In thermogravimetric analysis (Figure 3.9) SBA-15 sample shows a first weight loss of about 7% between room temperature and 175°C, with a maximum at 85°C, corresponding to the elimination of water weakly bound on the surface. The curve has a further weight loss of 5% between 180 and 1200 ° C, due to the condensation of silanols. Knowing the percentage of silanols present in SBA-15 is possible to derive the concentration of surface silanol species ($SiOH/nm^2$) by using Equation 3.4, where:

- %OH = TGA weight loss due to the condensation of silanols group;
- 2 = number of SiOH needed to form a water molecule by condensation;
- N_A= Avogadro number ($6.022*10^{23}$);
- $M.W._{H_2O}$ = molecular weight of water (18.01 g/mol);
- S.S.A= Specific Surface Area of the sample, estimated by N_2 Physisorption Analysis.

$$\frac{SiOH}{nm^2} = \frac{\%OH}{100-\%OH} * \frac{2* N_A}{M.W._{H_2O}*S.S.A} \quad (3.4)$$

The concentration of surface silanols in SBA-15 silica calculated by using Equation 3.4 is ca. 5 $SiOH/nm^2$. After the grafting procedure, assuming a complete reaction between the organo silane and the surficial silanol groups, is possible to estimate the silanols density ($SiOH/nm^2$) condensed during the amino-silane grafting to form tridentate complexes by using Equation 3.5, where:

- N Conc = Nitrogen concentration estimed with elemental analysis [mmol/g];
- N_A= Avogadro number ($6.022*10^{23}$);
- 3= number of silanols in each silane;
- 10^{18} = conversion factor m^2/nm^2;
- S.S.A = Specific Surface Area of the sample, estimated by N_2 Physisorption Analysis.

$$\frac{\mathrm{SiOH}}{\mathrm{nm^2}} = \frac{\mathrm{N\ Conc.}}{10^{18}} * \frac{\mathrm{N_A}}{\mathrm{S.S.A}} * 3 \qquad (3.5)$$

This approximation overestimates the number of silanols involved in this condensation reaction, because also bidentate complexes may be produced during the grafting procedure. Finally, by subtracting the surficial silanol concentration to the concentration of silanols present in the organo silane, is possible to estimate the number of remaining silanols on the surface of the functionalized samples. The concentration of silanols consumed in the condensation reaction and the concentration of silanols remaining on the surface of the hybrid materials are reported in Table 3.3.

Sample	**SiOH/nm^2 condensed**	**SiOH/nm^2 Remaining**
A-SBA-15	2.6	2.4
E-SBA-15	3.2	1.8
P-SBA-15	2.9	2.1

Table 3.3. Concentration of silanols involved in condensation reactions during the introduction of the organic species and final silanol concentration in hybrid samples.

The presence of organic species grafted on the SBA-15 surface silica was also evaluated qualitatively by FT-IR spectroscopy. The FT-IR spectra of pure SBA-15 and grafted materials are reported in Figure 3.10.

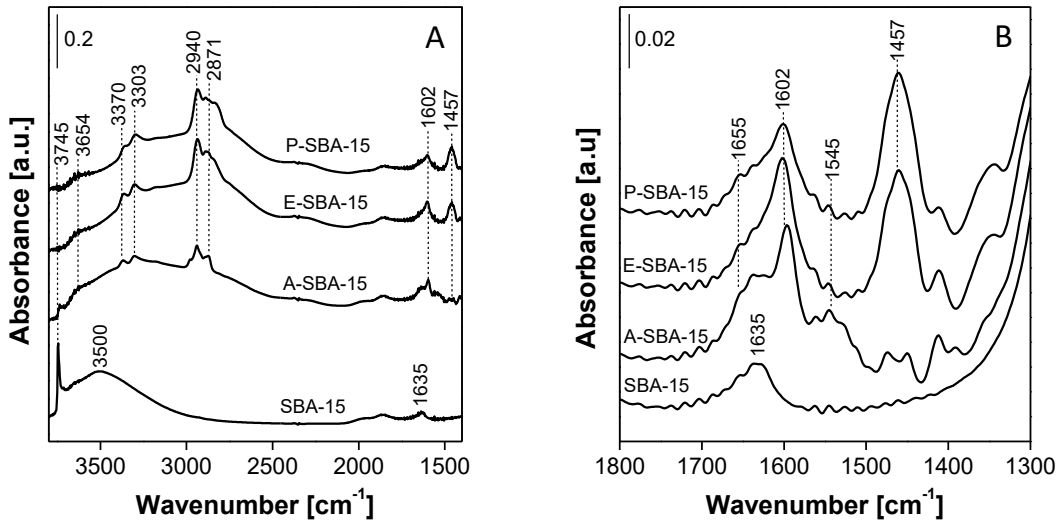

Figure 3.10. Frame A: FT-IR spectra of SBA-15 and grafted samples. Frame B: enlargement of the FT-IR spectra in the 1800-1300 cm^{-1} range. Spectra were recorded after outgassing the samples at r.t. for 30 minutes. [26]

In the high frequency range, the FT-IR spectrum of SBA-15 silica sample (Figure 3.10, frame A) presents a sharp band located at 3745 cm^{-1} and a broad band at *ca*. 3500 cm^{-1}. The first band is attribute to the stretching mode of isolated silanol groups [32], whereas the broader absorption at 3500 cm^{-1} is due to the stretching mode of hydroxyl species interacting each other through hydrogen bonding. [25]

After the grafting procedure, the bands due to surface SiOH species appear strongly decreased in intensity, especially for E-SBA-15 and P-SBA-15 sample, due to the condensation of the SiOH species with the organo-silane during the grafting procedure. A residual amount of isolated silanol species is still present only in A-SBA-15 sample. In addition, for the grafted materials, the formation of a broad band in the 3600-2500 cm^{-1} range is visible. This new band can be attributed to the formation of hydrogen-bonding interactions between surfacial silanols and the amino groups of silane species introduced with the functionalization. At lower frequencies, the FT-IR spectra of grafted samples are characterized by complex absorptions in the 3500–2500 cm^{-1} range, in which bands at 3370, 3303, 2940 and 2871 cm^{-1} can be

observed. Furthermore, in the low frequency region (Figure 3.10, frame B) bands at 1600 cm^{-1}, due to the scissoring mode of NH_2 groups, and at 1457 cm^{-1}, ascribed to the bending modes of CH_2 groups, are visible. [25] Finally A-SBA-15 sample presents bands at 1655 and 1545 cm^{-1}, attributed to vibrations of NH_3^+ species. [25, 26]

The presence of the organic species grafted on the SBA-15 silica surface was also evaluated by solid state NMR spectroscopy. In particular, ^{29}Si MAS NMR and ^{13}C CPMAS NMR analysis were performed (Figure 3.11, frame A and B, respectively).

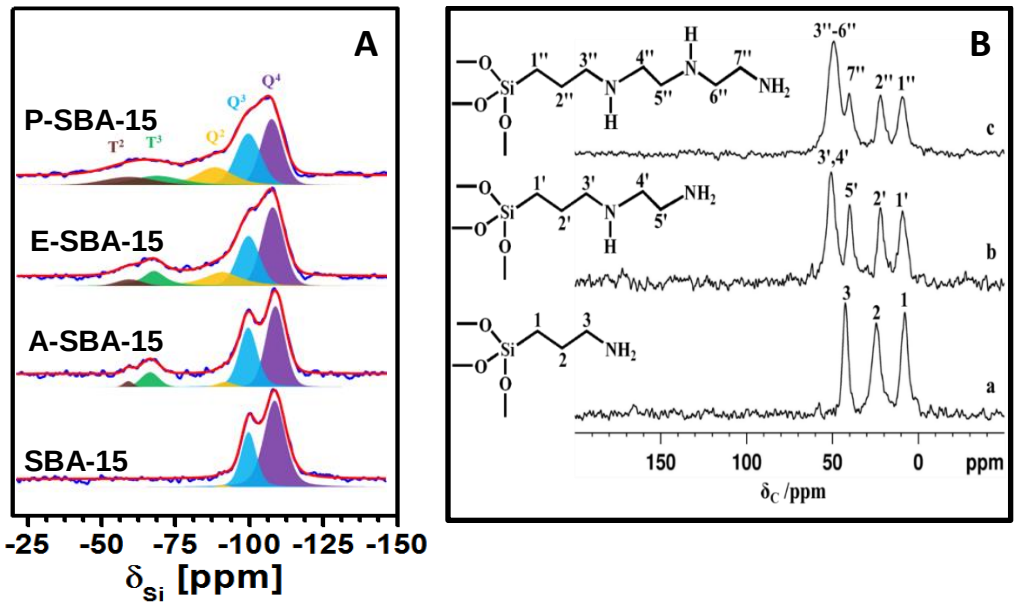

Figure 3.11 Frame A: ^{29}Si MAS NMR spectra of SBA-15 and related grafted hybrid samples recorded at a MAS rate of 10 kHz. Both experimental curve and its deconvoluted spectrum with individual contribution from each ^{29}Si sites are reported. Frame B: ^{13}C CPMAS NMR spectra of A-SBA-15 (a), E-SBA-15 (b) and P-SBA-15 samples (c). A cross polarization contact time of 2 ms and a MAS rate of 10 kHz were used. [26]

The ^{29}Si MAS NMR spectra (Figure 3.11 A) of all samples show resonances at around -111, -102 and -93 ppm due to Q^4 ($Si(OSi)_4$), Q^3 ($Si(OSi)_3OH$) and Q^2 ($Si(OSi)_2(OH)_2$) species, respectively. In addition, grafted SBA-15 samples

(*i.e. A*-SBA-15, E-SBA-15 and P-SBA-15) show resonances at -66 and -58 ppm attributed respectively to T^3 ($Si(OSi)_3C$) and T^2 Si sites ($Si(OSi)_2(OH)C$). These resonance peaks indicates that a successful grafting process has occurred, as already seen by FTIR spectroscopy. [33, 26]

Figure 3.11 B displays ^{13}C CPMAS spectra of grafted hybrid materials. Well-defined resonances at around 8, 24 and 42 ppm attributed to carbon atoms C1, C2 and C3 are visible in the spectra of A-SBA-15. Equally, similar carbons in E-SBA-15 and P-SBA-15 present resonance at around 9 and 22 ppm. However, in E-SBA-15 and P-SBA-15, carbon atoms bind to NH group display a separate resonance at 50 ppm besides the resonance at 40 ppm for NH_2 bound carbon. Therefore, from these analyzes it can be concluded that the grafting functionalization has been successful on all the materials. [26]

3.4.3 Interactions between Basic Groups and Surficial Silanols

A study focused on the interactions between the amino groups present in the organic chains and the silanol groups present on the surface, was performed. This point is crucial for understanding the reactivity of these samples towards carbon dioxide. In fact, recently in the literature it has been hypothesized that such interaction between silanols and amino groups can favour the CO_2 adsorption. [8] In detail, this specific interaction was studied by evaluating the mobility of the organic chains, assuming that the interaction with silanol groups reduces the mobility of the organic chains. This behaviour was studied initially by using single pulse excitation ^1H MAS NMR spectroscopy (Figure 3.12, Frame A). This technique in fact allows to distinguish mobile from rigid components by analyzing the width of the peaks: narrow peaks correspond to high mobility, while broad signals correspond to reduced mobility. [26]

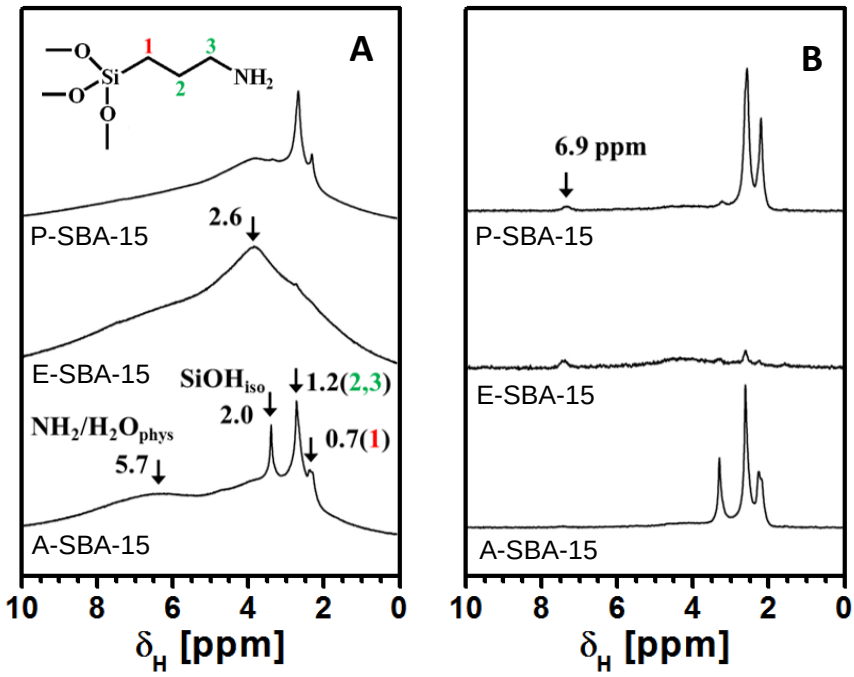

Figure 3.12. ^{1}H MAS NMR (Frame A) and Hahn-echo NMR spectra (Frame B) of hybrid SBA-15 samples. [26]

In Figure 3.12 A, A-SBA-15 and P-SBA-15 sample show narrow resonances at around 0.7 ppm due to CH_3 protons near silicon atoms and a sharp peak at around 1.2 ppm due to the remaining methylene protons. In addition, a peak at 2 ppm attributed to surface silanols is also visible. This suggest that in A-SBA-15 and P-SBA-15 samples organic chains are free to move. On the contrary, no sharp resonances are present for E-SBA-15 sample, suggesting that all the EAPTS chains are in a confined space, where they experience reduced mobility. This effect is probably due to the inter- and/or intra-molecular interactions. For example, intermolecular interactions can occur with the silica surface through bindings by silanols. Finally, a broad resonance peak at 5.7 ppm is visible in all the spectra. This peak is attribute to the interactions between NH_2 groups and the physisorbed water remaining after the thermal treatment and H-bonded silanols. [26]

In order to better investigate the mobility of the organic chains in grafted samples, rotor synchronized Han-eco sequence ($\pi/2$-τ- π- τ) with long time delay (τ : 6700 μs) was also applied (Figure 3.15, Frame B). This sequence allows the selective detection of mobile species, while rigid component are not resolved from the baseline. From spectra in Figure 3.12 B, it can be observed that A-SBA-15 and P-SBA-15 samples show narrow peaks due to the methylene protons of the organic chains. In addition, a resonance at about 2 ppm, attributed to isolated silanols, is also visible. Instead, in E-SBA-15 sample no resonance can be observed, confirming that for this sample a reduced mobility of the organic chains is present due to inter- and/or intra-molecular interactions in/among the organic chains. [26]

The possibility that the grafted chains can interact each other can be estimated by comparing an approximation of the molecular length of the organic chains with the average area around each organo-silane. In Table 3.4, the free average space of each silane domain (calculated as the inverse of the organo-silane density) and the average intermolecular distance (calculated as the square root of this area) are reported; the chain lengths were obtained from ab initio geometry optimizations (see below).

Sample	**Silane Density [n°chains/nm^2]**	**Intermolecular Distance [Å]**	**Length of Silane[a] [Å]**
A-SBA-15	0.9	10.5	5.3
E-SBA-15	1.1	9.5	7.1
P-SBA-15	1.0	10.0	8.9

Table 3.4. Distances between chains of the organo-silane in grafted silica samples.

In order to better investigate the arrangement of organic chains in the space, theoretical calculations have been performed, by using Gaussian09 program at Density Functional Theory (DFT) level. (In detail, hybrid functional B3LYP [4,35] using Dunning's correlation consistent cc-PVDZ basis set on light atoms[36,37] and LANL2DZ effective core potentials and the basis set for silicon [38] were used. In

order to estimate the contribution from dispersion forces to energies and geometrical structures, an atom-atom pairwise algorithm proposed by Grimme[39] and implemented in Gaussian09 was also used. The silica surface was simulated by using two different clusters of amorphous silica reported in the literature [40]: $Si_{39}O_{112}H_{68}$ (Cluster I) and $Si_{52}O_{152}H_{92}$ (Cluster II), with a surface of approximately 2.5 and 4 nm^2, respectively. The silanol concentration on the model surface was set to 5 $SiOH/nm^2$, according to experimental data reported before. In order to simulate the surface after the functionalization, APTS, EAPTS and PAPTS molecules were introduced on the surface by elimination three water molecules per chain from SiOH groups, thus forming Si-O-Si bonds.[26] Initially, one molecule of each organo-silane was added to cluster I, and the optimized geometries are reported in Figure 3.13.

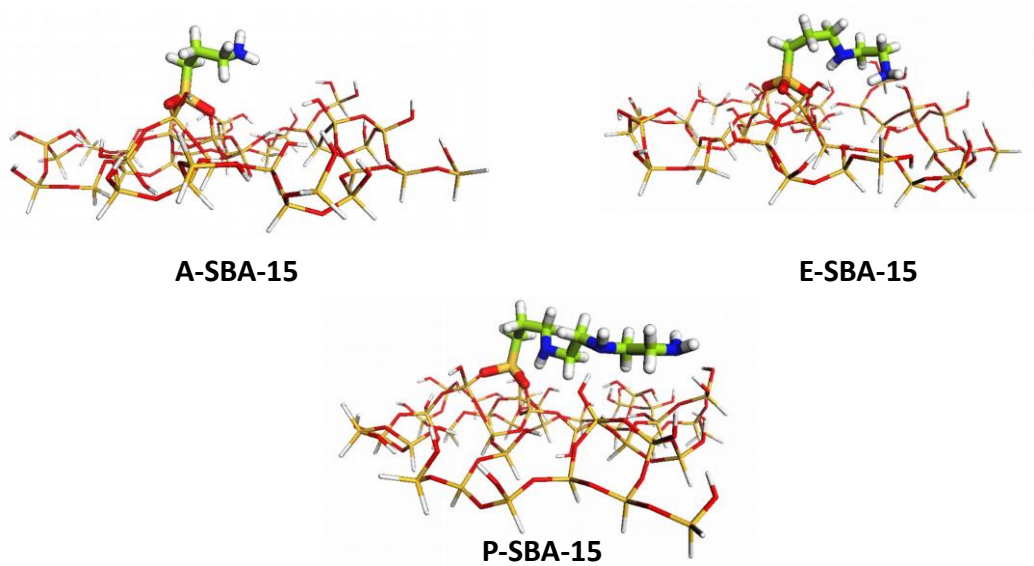

Figure 3.13. Optimized structures of APTS, EAPTS and PAPTS adducts on silica model cluster I. [26]

From optimized structures reported in Figure 3.13 it can be noted that APTS chain is not bended towards the surface due to its relatively short chain, while EAPTS and PAPTS grafted chains can lie down on the silica surface, forming hydrogen bond

between silanols and amino groups. In order to deepen also intermolecular interactions, adducts with two molecules grafted on cluster II were optimized (Figure 3.14).

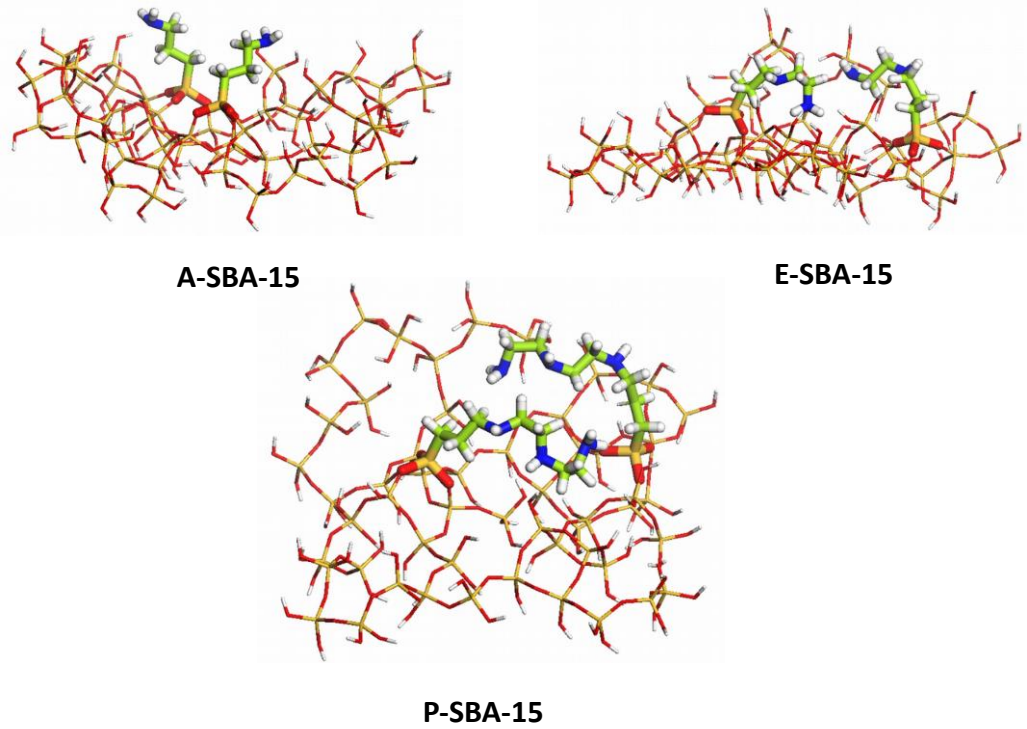

Figure 3.14. Optimized structures of two molecules of APTS, EAPTS and PAPTS adducts on silica model cluster II. [26]

By adding a second organic molecule, the behaviour of the organo-silane on the surface does not present many variations with respect to the presence of a single chain: APTS chain remains perpendicular to the surface, while EAPTS and PAPTS chains lie on the surface. However, in PAPTS grafted sample, not all the amino groups are involved in hydrogen bond with silanols, because there are not enough silanols in suitable positions. This may be the reason why PAPTS chains can move more easily, as observed through NMR spectroscopy analysis (even if this is just one of the possible conformations). [26] Since we are using a cluster (cluster II) with an area of about 4 nm^2, and given that the estimated amount of silane introduced is about

1 chain/nm^2 (see Table 4) we decided to add a third EAPTS and PAPTS chain to cluster II. We decided to study only these two systems because in this longer chains steric effects are expected to be more relevant. The optimized structure are given in Figure 3.15.

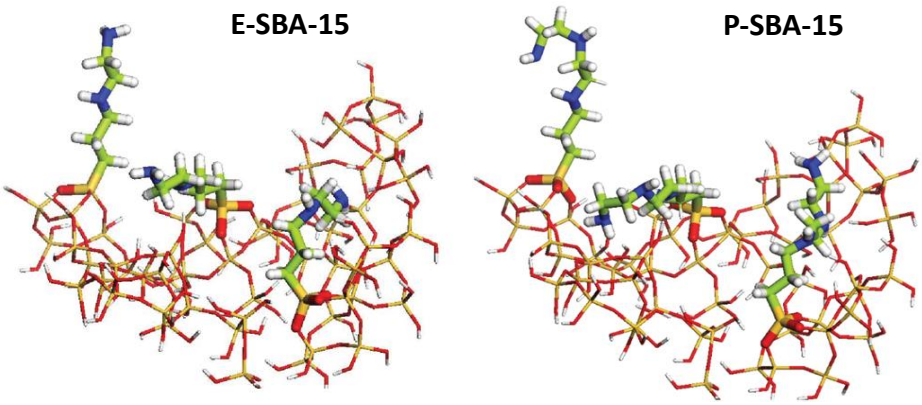

Figure 3.15. Optimized structures of three molecules of EAPTS and PAPTS adducts on silica model cluster II. [26]

After the introduction of the third organic molecule on cluster II, steric hindrance effects became more relevant. In particular, in both structures the third organic chain remains perpendicular and has no access to the silica surface.

3.5 Study of the Reactivity of SBA-15-based Hybrid Samples towards CO_2

Infrared spectroscopy of adsorbed carbon dioxide was used to study the reactions between CO_2 and amino groups of the hybrid silica samples. Self-supporting pellets were placed in a IR cell with KBr windows permanently attached to a vacuum line. In this way all treatments and adsorption-desorption procedure are allowed to be carried out *in situ*. Before the experiment, the silica samples were outgassed at 135°C for 3 h (heating ramp: 5°C/min) in order to desorb the water adsorbed on the silica surface. After the treatment, the samples were cooled to room temperature.

The IR spectrum of P-SBA-15 sample collected after the introduction of 60 mbar of CO_2 at beam temperature (35°C) is reported in Figure 3.16. In addition, spectra obtained by decreasing the CO_2 pressure until final vacuum are also reported.

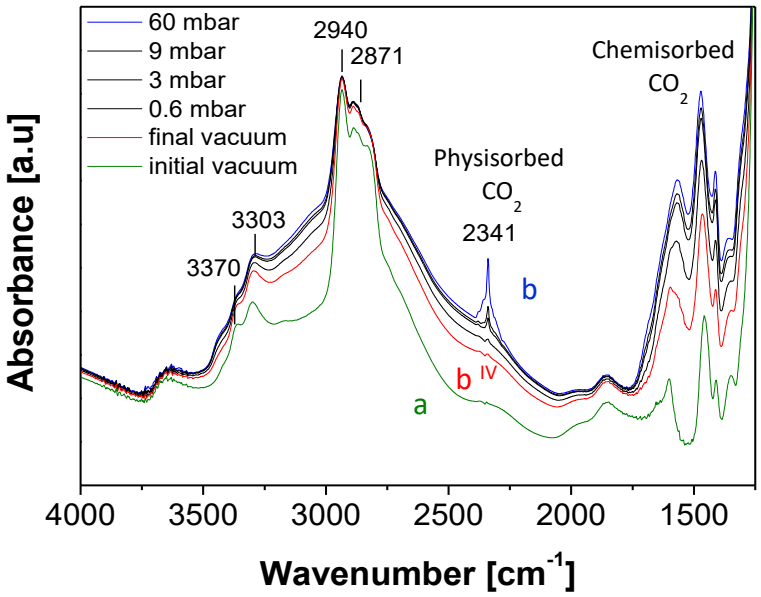

Figure 3.16. FT-IR of P-SBA-15 sample (curve a) and adsorbed CO_2 at room temperature on P-SBA-15 sample (curves b-b ^{IV}).

After the introduction of 60 mbar of CO_2, the IR spectrum of P-SBA-15 appears modified (Figure 3.16, curve b). At high wavenumbers, bands at 3370 and 3303 cm^{-1}, attributed to asymmetric and symmetric stretching modes of NH_2 groups, respectively, and band located at 2940 and 2871 cm^{-1}, due to asymmetric and symmetric stretching of the CH_2 groups of the aliphatic chain, respectively, are modified, suggesting that the organic chain interacts with the carbon dioxide. In addition, at 2341 cm^{-1} appears a band given by the asymmetric stretching (ν3) of CO_2, thus demonstrating the presence of carbon dioxide physisorbed on the material. In the lower frequency region, bands attributed to species formed during the reaction between amino groups and carbon dioxide are present. In order to better analyze this bands, the difference spectra, obtained by subtracting the spectrum recorded before

sending CO_2 (used as background) to all the spectra recorded after the sending of carbon dioxide are reported in Fig. 3.17. In this way, only the modifications due to the chemical reaction are visible; in particular, bands formed during the reaction appears positive, while bands decreased during the interaction are negative. [26]

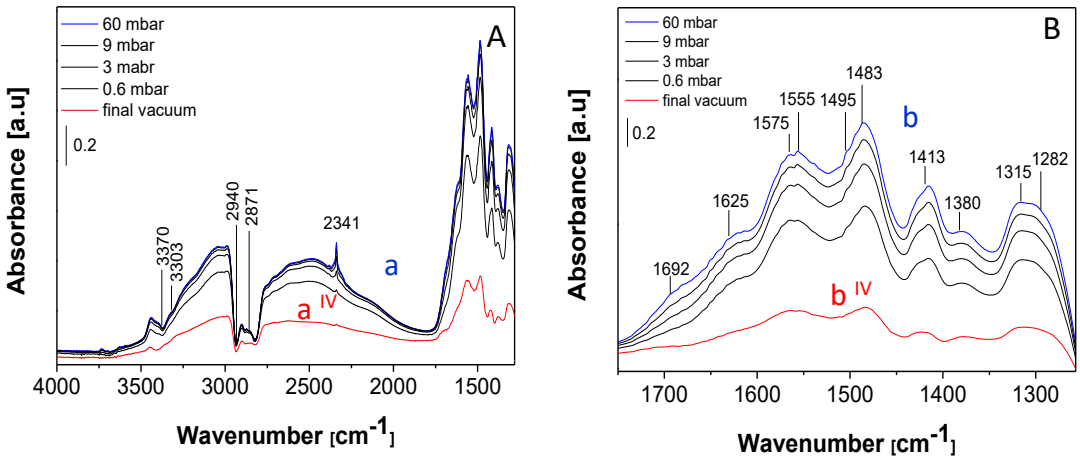

Figure 3.17. Subtracted FT-IR spectra of adsorbed CO_2 at room temperature on P-SBA-15 sample in the 4000-1250 cm^{-1} region (Frame A) and in the 1750-1250 cm^{-1} region (Frame B).

By analyzing the spectrum in the chemisorption region (*i.e.* 1750-1250 cm^{-1}, Figure 3.17, Frame B) it can be noted that the admission of CO_2 leads to the formation of bands attributed to both carbamic acid and ammonium carbamate. The formation of these products and the relative mechanisms has been described in the introductive chapter. In detail, bands at 1555, 1495 and 1413 cm^{-1} are due to the formation of ammonium carbamate, while peaks located at 1692 and 1380 cm^{-1} are attributed to carbamic acid. Detailed assignments of these bands are given in Table 3.5.

Wavenumber [cm^{-1}]	Assignment	Ref.
1692	Stretching (C=O) of carbamic acid	43,44
1625	Asymmetric bending of NH_2^+ /NH_3^+	43, 45-48
1575	Deformation of NH_2^+ or combination of N-H deformation and C-N stretch vibrations in intermolecular carbamates	42
1555	Asymmetric stretching of C=O group of carbamate	48
1495-1483	Stretching of $NHCOO^-$ of Carbamate	43, 44, 46-51
1500-1485	Symmetric bending of NH_2^+ /NH_3^+	43, 45-51
1438-1413	Symmetric stretching of COO^- group of carbamate	43, 45, 50
1380	bending of OH in carbamic acid	41, 50
1332-1315	$NCOO^-$ skeletal vibration	45
1282	Rocking of NH_3^+	43

Table 3.5. Assignments of FT-IR bands in the 1250-1750 cm^{-1} region attribute to the chemisorbed species on grafted SBA-15 samples. [26]

By decreasing progressively the carbon dioxide pressure (Figure 3.17 B, curves b^I – b^{IV}) bands related to ammonium carbamate and carbamic acid progressively decrease in intensity, thus indicating that a portion of the formed species is removed during the outgassing procedure. Deconvolution and integration of bands between 1410 and 1440 cm^{-1} (representative of ammonium carbamate) and band at 1380 cm^{-1} (representative of carbamic acid) demonstrate that the intensity of these bands decrease in the same way, suggesting that ammonium carbamate and carbamic acid species have approximately the same stability.

By analyzing the spectrum related to the final vacuum (Figure 3.17, curve b^{IV}), it can be noted that the bands attributed to ammonium carbamate and carbamic acid do not completely disappear, indicating that a fraction of these products are in strong interaction with the surface. [26]

In order to compare the adsorption of CO_2 of the three samples, the spectra collected after the admission of 60 mbar of carbon dioxide on SBA-15 silica grafted with

APTS, EAPTS and PAPTS are reported in Figure 3.18.

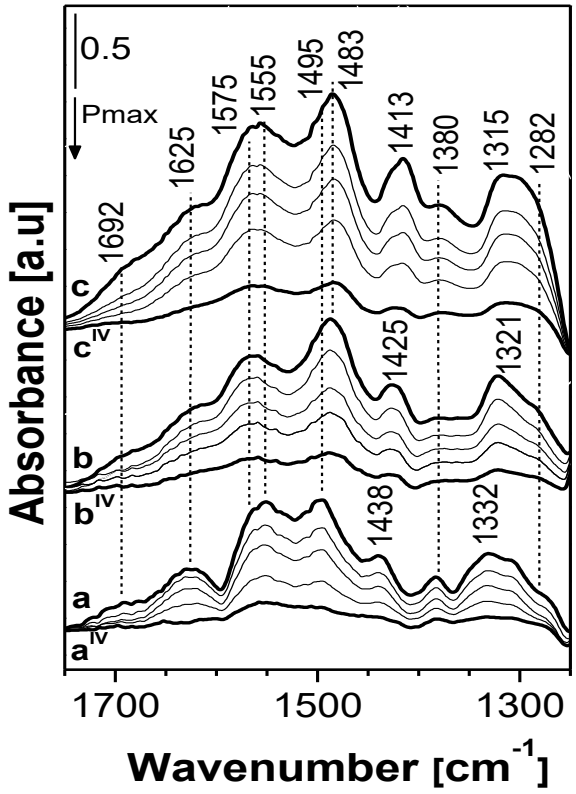

Figure 3.18. FTIR spectra, in the 1750–1250 cm^{-1} region, of CO_2 adsorbed (Pmax = 60 mbar) at BT on grafted samples: A-SBA-15 (curves a-a^{IV}), E-SBA-15 (curves b-b^{IV}) and P-SBA-15 (curves c-c^{IV}). Spectra are normalized by dividing the spectrum by the density of the self standing pellets, and are reported after subtraction of the spectrum of the bare sample (before CO_2 interaction) used as a background. [26]

It can be noted from Figure 3.18 that the admission of carbon dioxide leads to the formation of carbamic acid and ammonium carbamate in all the samples.

Concerning E-SBA-15 and P-SBA-15 samples (*i.e.* samples grafted with amino silanes containing more than one amino groups per chain), it can be noted the formation of a shoulder at 1575 cm^{-1}, not present in A-SBA-15 spectra, that can be

attributed to the formation of NH_2^+ species, or to the combination between N-H deformation and C-N vibration in carbamates. This indicates that samples containing more than one amino group per chain can react with carbon dioxide by intramolecular mechanism, forming an intermolecular ammonium carbamate salt. The formation of intramolecular species is also confirmed by the modification of the band at 1625 cm^{-1}, attributed to the asymmetric bending of NH_3^+: in A-SBA-15 spectrum this signal is more resolved, while in E-SBA-15 and P-SBA-15 it becomes broader, suggesting the presence of NH_2^+ groups.

Furthermore, a shift of symmetric stretching of COO^- groups (from 1438 to 1413 cm^{-1}) and $NCOO^-$ skeletal vibration (from 1332 to 1315 cm^{-1}), probably due to the increase of the length of the organic chains, is observable passing from A-SBA-15 to P-SBA-15 samples.

Concluding this comparison, the intensity of the bands, attributed to the chemisorbed species formed from the interaction between carbon dioxide and amino groups, increases by increasing the number of amino groups present in the chain (passing from A-SBA-15 to P-SBA-15): the higher is the amino groups content, the higher is the reactivity of the grafted samples. [26]

Additional information on the interaction between the organo-modified SBA-15 materials and the carbon dioxide molecule has been achieved by ^{13}C CPMAS NMR spectroscopy. In a typical experiment, before the gas adsorption test, samples were outgassed at 135°C for 3 h (heating ramp: 5°C/min) by using an oil-free apparatus and a grease-free vacuum line. After, the samples were cooled at 35°C and put in contact with 60 mbar of $^{13}CO_2$ for 48 h. Finally, the treated samples were put in the rotor by using a glove box and submitted to the analysis. ^{13}C CPMAS NMR spectra of $^{13}CO_2$ adsorbed on the grafted samples are reported in Figure 3.19.

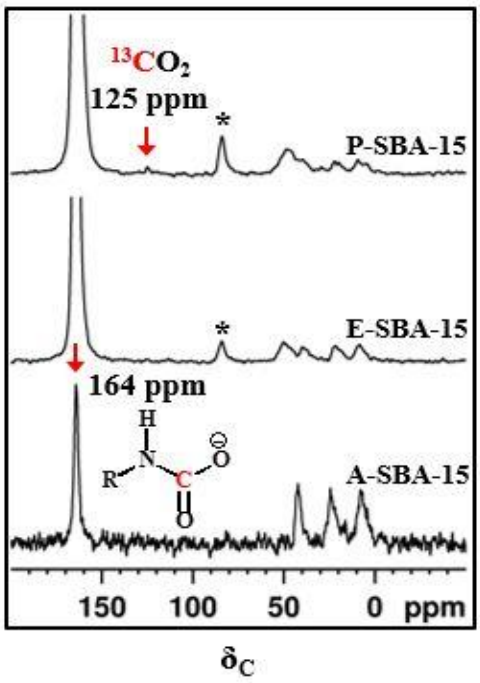

Figure 3.19. ^{13}C CPMAS NMR spectra of $^{13}CO_2$ adsorbed on grafted SBA-15 samples. A cross polarization contact time of 2 ms and a MAS rate of 10 kHz was used in all the experiments. * Denote spinning side-bands. [26]

Analyzing the ^{13}C CPMAS NMR spectra of grafted SBA-15 samples after the adsorption of $^{13}CO_2$ it can be observed that no dramatic changes in chemical shifts of aliphatic carbons are present with respect to the spectra of the pristine samples, even if a broadening of the resonances is evident (Figure 3.19). Moreover, an additional resonance at 164 ppm, attributed to the presence of carbamate groups, is clearly visible in all the samples. Since this resonance lies near the chemical shift values expected for typical carbamic acid (160 ppm), bicarbonate (163 ppm) and ammonium carbamate (164 ppm) species, and since the full width at half-maximum is larger (about 4 ppm) than the chemical shift difference between these products, the presence of carbamic acid and bicarbonate is also possible in the samples considered. The intensity of the signal due to the carbamate species increases by increasing the length of the organic chain (and the concentration of N atoms). These

results, in line with those obtained by FT-IR spectroscopy, suggested that the amount of amino groups influence the reactivity with the $^{13}CO_2$. Finally, ^{13}C CPMAS NMR data revealed the presence of physisorbed $^{13}CO_2$ at 125 ppm, especially in the case of P-SBA-15. [26]

The mobility of the organic chain after the sending of $^{13}CO_2$ was also studied. The obtained ^{1}H MAS NMR (Frame A) and Hahn-echo NMR spectra (Frame B) are given in Figure 3.20.

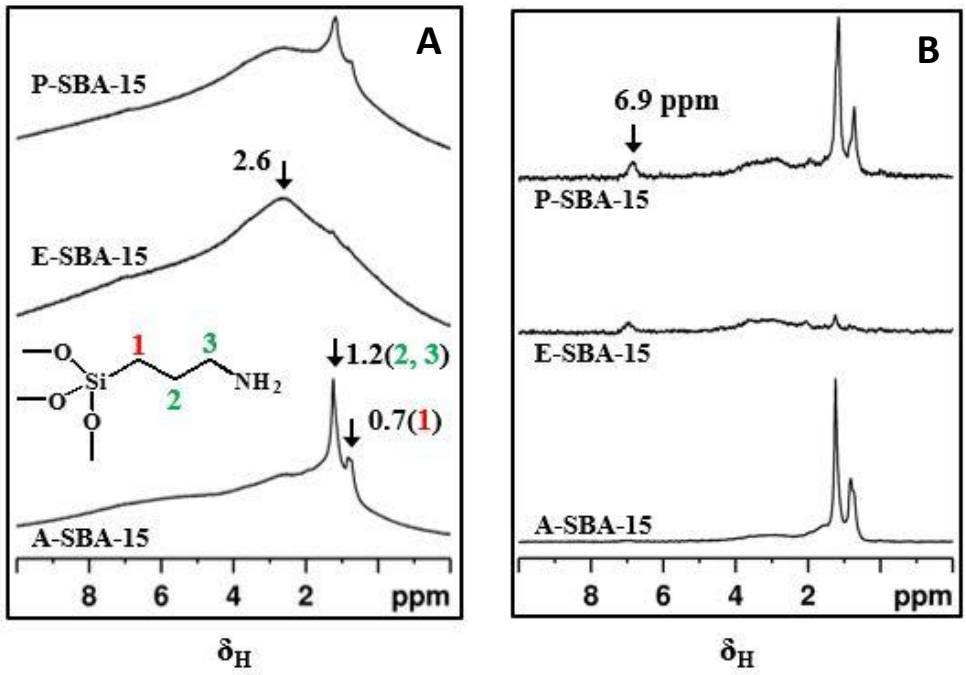

Figure 3.20. ^{1}H MAS NMR (Frame A) and Hahn-echo NMR spectra (Frame B) of hybrid samples after the adsorption of $^{13}CO_2$ on SBA-15 grafted samples. **[26]**

Before the introduction of $^{13}CO_2$, A-SBA-15 and P-SBA-15 samples showed similar amount of mobile and rigid components. On the contrary, only rigid components were visible in sample E-SBA-15, as confirmed by the absence of sharp peaks in the Hahn-echo NMR spectra (Figure 3.12). However, after the adsorption of $^{13}CO_2$, an increase in the rigid components has been observed for all the samples (Figure 3.20). In addition, an increase in the amount of protonated amino groups is visible in all the three hybrid samples. [26]

3.6 Evaluation of the CO_2 Capture Performances

After the qualitative and semi quantitative evaluation of CO_2 adsorption properties on SBA-15 hybrid materials, a quantitative study on the carbon dioxide capture capacity has been carried out by using different techniques.

First of all, volumetric measurements were carried out on all materials at room temperature by using a Quantachrome Autosorb iQ2 instrument . Before the analysis the samples were outgassed at 135°C for 3 h (1°/min heating rate and residual pressure $p < 10^{-6}$ Torr). Figure 3.21 shows the volumetric experiments for SBA-15 grafted samples.

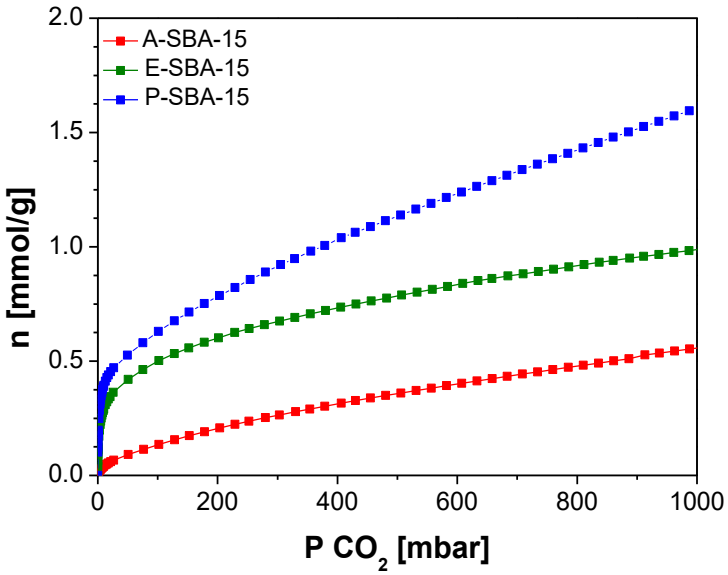

Figure 3.21 CO_2 uptake of A-SBA-15, E-SBA-15 and P-SBA-15 samples at 35°C obtained by volumetric measurements.

The carbon dioxide uptake capacity of the three hybrid samples follows the trend discussed before and determined by FT-IR and SS-NMR spectroscopies: the adsorption capacity is indeed higher for P-SBA-15 than E-SBA-15 and finally A-SBA-15. For all the samples is possible to distinguish two different regions of adsorption. At low pressures, a steep increase of the CO_2 uptake, attributed to the

chemisorption of carbon dioxide on more reactive amino sites, is observable. Instead, at higher pressure a less steep increase of the adsorption capacity is visible.

The lower amount of carbon dioxide adsorbed on A-SBA-15 sample can be related to the different adsorption mechanism compared to the samples containing more than one amino group in the same chain (E-SBA-15 and P-SBA-15). In fact, in this case, the formation of carbamate species occurs only when two amino groups contained in adjacent chains are able to interact, following the intermolecular mechanism. If the organic chain is distant from one other, the adsorption process can not occur. Instead, for E-SBA-15 and P-SBA-15, ammonium carbamate species can be formed more favorably, because two amino groups are present in the same chain; in this case, also intramolecular mechanism occurs. [26]

At relative pressure compatible with post combustion conditions (p=100 mbar) the CO_2 uptake values are 0.18 mmol/g, 0.49 mmol/g and 0.62 mmol/g respectively for A-SBA-15, E-SBA-15 and P-SBA-15. These results are comparable with those obtained with microcalorimetric analysis, in collaboration with Dr. Valentina Crocellà and Prof. Silvia Bordiga from University of Turin. The adsorption capacity values obtained with this technique are: 0.31 mmol/g, 0.51 mmol/g and 0.68 mmol/g, respectively for A-SBA-15, E-SBA-15 and P-SBA-15 samples. [26]

The adsorption of carbon dioxide was also monitored by using the Zero Length Column Analysis (ZLC). This is an innovative and advantageous screening method for amino-grafted silica adsorbents, because it requires a very small amount of samples (10–15 mg) and short experimental time (about 1 hour per test). Zero Length Column Analysis were realized during the stage at the University of Edinburgh's School of Engineering under the supervision of Dr. Enzo Mangano and Prof. Stefano Brandani.

The Zero Length Column consists of a 1/8 Swagelok union in which a small amount of sample is placed as monolayers between two sister discs. In this experiment the sample, after a treatment at 135°C for 3 h (1°C/min heating ramp) under helium flow, is cooled to 35°C and is put in with a mixture of 10% CO_2 in He at a constant flow rate. After reaching the equilibrium, the inlet flow to the ZLC is switched to pure He (carrier) and the desorption process is followed. For this study, the amount of sample packed in the ZLC was 3.5mg, 5.9 mg and 7.3 mg, respectively for A-SBA-15, E-SBA-15 and P-SBA-15. Each experiment was performed at two different flow rates (2 and 2.7 mL/min), in order to check if the samples are in equilibrium or kinetically controlled regime. [52] To ensure that a complete equilibrium was reached, the ZLC experiment was repeated at increasing adsorption times. The system was considered to be in equilibrium when the carbon dioxide uptake did not increase by increasing the adsorption time. According to this procedure, the resulting equilibration time were 40 min for A-SBA-15 and 20 min for E-SBA-15 and P-SBA-15 samples. [26]

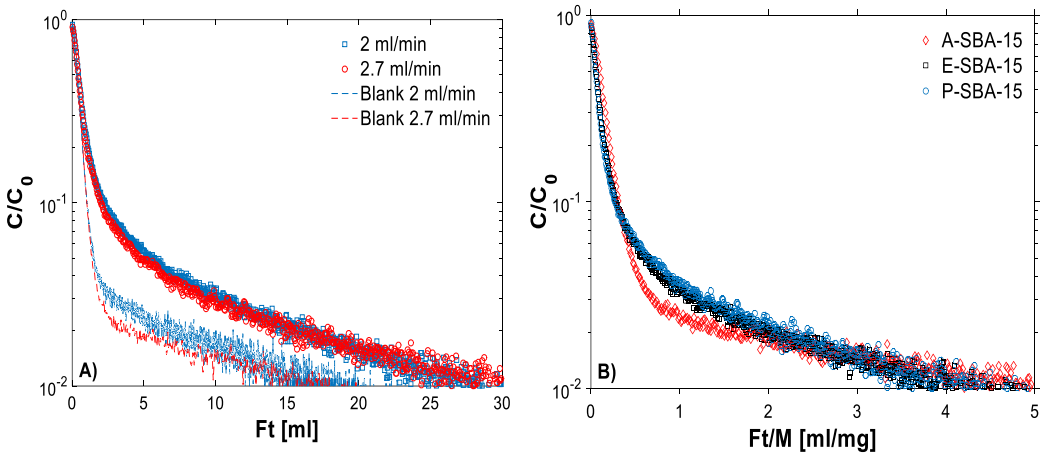

Figure 3.22 Frame A: ZLC desorption curves for P-SBA-15 sample and blank curves at 2 and 2.7 ml/min flow rates. Frame B: ZLC desorption curves for A-SBA-15, E-SBA-15 and P-SBA-15 samples (CO_2 partial pressure: 0.1 bar, T: 35°C). [26]

In Figure 3.22 is reported an example of the ZLC desorption curve for the P-SBA-15 sample. The data are plotted as dimensionless concentration, C/C_0 (where C_0 is the CO_2 concentration in the gas phase at the equilibrium), vs. the volume of gas eluted Ft (where F is the inlet flowrate of helium). The plot includes the blank curves, *i.e.* the response of the system when no sample is loaded. The difference between the area under the desorption curve of the sample and the blank is proportional to the amount of carbon dioxide adsorbed. [53] The CO_2 adsorption capacity can be calculated by integration, following Equation 3.6.

$$q = \frac{A_{sample}p - A_{blank}p}{MRT} \tag{3.6}$$

Where q is the adsorption capacity, p is the pressure of CO_2 (*i.e.* 0.1 mbar), M is the mass of the sample, R is the gas constant (= 8.31 bar ml/mol K), T is the sample temperature and A is the area under the desorption curves (given in Equation 3.7).

$$A = \int_0^\infty \frac{C}{C_0} d\,(Ft) \tag{3.7}$$

The C/C_0 value can be obtained by applying Equation 3.8:

$$\frac{C}{C_0} = \frac{\sigma_t - \sigma_\infty}{\sigma_0 - \sigma_\infty} \tag{3.8}$$

where σ_0 is the signal value of the mass spectrometer (expressed in Torr) at initial time (*i.e.* the signal at saturation level, before starting the desorption), σ_t is the signal at time t during the desorption and σ_∞ is the value of the signal when the desorption has ended (*i.e.* the baseline).

The flowrate of the carrier gas F used in Equation 3.7 is obtained from the measured flowrate after two corrections.

The first is a flow correction, and takes into account that, as a result of the CO_2 adsorption of the sample, the composition of the mixture changes: the more carbon dioxide is adsorbed, the more mixture will be diluted. The flow correction is reported in Equation 3.9.

$$F = F_{corr\,T} \frac{1}{1 - y\frac{C}{C_0}} \tag{3.9}$$

Where y is the mole fraction (y=1).

The second correction that should be applied to the flowrate is a temperature correction, that takes into account of the difference in temperature between when the flowrate is measured (T_{out}= 20°C) and when the adsorption occurs the temperature of the flow is higher (T_{in}=35°C).

$$F_{corr\,T} = F_{measured} \frac{T_{in}}{T_{out}} \tag{3.10}$$

By normalizing the Ft plot by the mass of the sample, M, the ranking of the carbon dioxide uptake for each hybrid SBA-15 sample can be visually compared (Figure 3.22).

The adsorption capacity values calculated for the ZLC desorption curves for the different samples are 0.23 mmol/g, 0.39 mmol/g and 0.51mmol/g, respectively for A-SBA-15, E-SBA-15 and P-SBA-15 sample. A summary of the quantitative determination of CO_2 adsorption capacity values for the hybrid SBA-15 samples is given in Table 3.6.

Sample	Adsorption Capacity [mmol·g^{-1}]		
	Volumetry	**Microcalorimetry**	**ZLC**
A-SBA-15	0.18	0.31	0.23
E-SBA-15	0.49	0.51	0.39
P-SBA-15	0.68	0.68	0.51

Table 3.6. Comparison between ZLC, volumetric and calorimetric results for CO_2 adsorption at low pressure.

The sequence of the CO_2 capacities obtained with ZLC is in agreement with microcalorimetric and volumetric measurements, following the order P-SBA-15 > E-SBA-15 > A-SBA-15.

ZLC method allows also to measure the amount of desorbed CO_2 from the sample. For a purely physisorption process this is the same as the amount originally adsorbed in the sample. In this case, it seems very likely that a portion of the amount adsorbed is chemically bound to the amine groups, therefore irreversibly adsorbed during the time of the experiment (as we can see from FT-IR spectra of desorbed CO_2, Figure 3.18). Temperature programmed desorption (TPD) analysis was carried out on some of the samples, but the signal related to the amount desorbed at high temperature was too close to the detector baseline to be accurately quantified. This, however, can explain the small discrepancy with the adsorbed amount measured by using the volumetric system.

In general, the ZLC analysis also allows to study the equilibrium and the kinetics of adsorption. Unfortunately, in our case the amount of adsorbed carbon dioxide for the samples is particularly low at these conditions; consequently, the experimental ZLC curves are too close to the blank curves, hindering further considerations. [26]

3.7 Conclusions

The adsorption properties of hybrid SBA-15 materials prepared by post synthesis grafting method with APTS, EAPTS and PAPTS, were studied by using a multidisciplinary approach. Both FT-IR and solid-state NMR spectroscopies of adsorbed carbon dioxide provided qualitative and semi quantitative information on the interactions between CO_2 and the amino groups of the functionalized silica samples.

First of all, these techniques confirmed the formation of ammonium carbamate and carbamic acid species, as a result of chemical interactions between amino groups and carbon dioxide. Moreover, both FT-IR and SS-NMR spectroscopies suggested that increasing the number of amino groups present in the chain increases also the reactivity toward CO_2, following the order P-SBA-15 > E-SBA-15 > A-SBA-15. In addition, also the interactions between the amino groups and the surface silanol species has been evaluated by analyzing the mobility of the chain with ^{1}H Hahn echo MAS NMR spectroscopy. This analysis suggested that A-SBA-15 and P-SBA-15 samples display similar amount of mobile and rigid components, while E-SBA-15 shows only rigid components, thus indicating that probably a greater interaction between the basic groups and OH groups present on the surface compared to A-SBA-15 and P-SBA-15 samples occurs. This behaviour agrees with the results of *ab initio* modeling theoretical calculations: the optimized adducts of the three organosilanes on some silica cluster models show that APTS chain interacts loosely with the surface, as well as PAPTS when the density of the grafted molecules is high enough. Viceversa, EAPTS chain lies on the surface, and is involved in H-bond with the surface silanols. In addition, after the introduction of $^{13}CO_2$, an increase in the rigid part was clearly observed for all the samples.

Finally, the amount of adsorbed carbon dioxide on SBA-15 grafted with amino-silanes were estimated comparing two different quantitative techniques: a classical volumetric analysis and the Zero Length Column chromathography. In particular,

the obtained values of the CO_2 adsorption capacity by means of volumetry are 0.18, 0.49 and 0.62 mol/kg, respectively for A-SBA-15, E-SBA-15 and P-SBA-15, while the CO_2 adsorption capacity values obtained with ZLC are 0.21, 0.44 and 0.53 mol/kg, respectively for A-SBA-15, E-SBA-15 and P-SBA-15. In both techniques the same sequence of carbon dioxide follows the order P-SBA-15 > E-SBA-15 > A-SBA-15. The presence of more than one amine in the same chain (EAPTS chain) favours the chemical adsorption of CO_2 also by intramolecular mechanism, thus increasing the total amount of adsorbed carbon dioxide. Moreover, the addition of a third amine in the chain (P-SBA-15 sample) further increases the CO_2 adsorption capacity.

References

[1] C. Chen, J. Kim, W.S Ahn, Korean *J. Chem. Eng.*, **2014**, 31, 1919-1934.

[2] V. Zelenák, M. Badanicová, D. Halamová, J. Cejka, A. Zukal, N. Murafa, G. Goerigk, *Chem. Eng. J.*, **2008**, 144, 336-347.

[3] A. Samanta, A.Zhao, G.K.H. Shimizu, P. Sarkar, P. Gupta, *Ind. Eng. Chem. Res*., **2012**, 51, 1438-1463.

[4] D. Rath, S. Rana and K. M. Parida, *RSC Advances*, **2014**, 4, 57111-57124

[5] Q. Wang, L. Luo, Z. Zhong and A. Borgna, *Energy Environ. Sci*., **2011**, 4, 42–55.

[6] F. Y. Chang, K. J. Chao, H. H. Cheng and C. S. Tan, *Sep. Purif. Technol*., **2009**, 70, 87–95.

[7] R.Sanz, G. Calleja, A. Arencibia, E. S. Sanz-Pérez, *Microporous and Mesoporous Materials*, **2012**, 158, 309–317.

[8] C. Y. Yoo, L. C. Lee and C. W. Jones, *Langmuir*, **2015**, 31, 13350-13360.

[9] D. Zhao, Q. Huo, J. Feng, B.F. Chmelka, G.D. Stucky, *J. Am. Chem. Soc.*, **1998**, 120, 6024-6030.

[10] B. Zornoza, S. Irusta, C. Tellez, J. Coronas, *Langmuir*, **2009**, 25, 5903.

[11] L. Cao, T. Man, M. Kruk, *Chem. Mater*., **2009**, 21, 1144.

[12] R. Ryoo, C. H. and Ko, *J. Phys. Chem. B*, **2000**, 104, 11465.

[13] P. F. Fulvio, S. Pikusb, M. Jaroniec, *J. Mater. Chem.*, **2005**, 15, 5049-5053.

[14] Zhang, F., Yan, Y., Yang, H., Meng, Y., Yu, C., Tu, B. and Zhao D., *J. Phys. Chem. B*, **2005**, 109, 8723.

[15] Nguyen, T.P.B., Lee, J-W., Shim, G.W. and Moon, H., *Microporous and Mesoporous Materials*, **2008**, 110, 560.

[16] V. Crocellà, T. Tabanelli, J.G. Vitillo, D. Costenaro, C. Bisio, F. Cavani, S. Bordiga, *Applied Catalysis B: Environmental*, **2017**, 211, 323–336.

[17] G. Gatti, D. F. Olivas Olivera, V. Sacchetto, M. Cossi, I. Braschi, L. Marchese, C. Bisio, *ChemPhysChem*, **2017**, 18, 17, 2374-2380.

[18] Brinker, C.J., Scherer, G. W., *San Diego: Academic Press*, **1990**.[19] Klemperer, W. G.; Mainz, V. V.; Ramamurthi, S. D.; Rosenberg. Brinker, C. J.; Clark, D. E.; Ulrich, *D. R. Editors. Materials Research Society: Pittsburgh*, PA, **1998**.

[20] Ying, J.Y., Mehnert, C.P., Wong, M.S., *Angew Chem Int Ed*, **1999**, 38, 56

[21] M. Managa, B. P. Ngoy,T. Nyokong, *Journal of Photochemistry and Photobiology A: Chemistry*, **2017**, 339, 49-58.

[22] J. N. Israelachvili and H. Wennerström, *J. Phys. Chem*., **1992**, 96, 520

[23] A.Galarneau, H. Cambon, F. Di Renzo, R. Ryoo, M. Choi, F. Fajula, *New J. Chem*., **2003**, 27, 73-79

[24] L. T. Gibson, *Chem. Soc. Rev.*, **2014**, 43, 5163.

[25] L. Etgar, G. Schuchardt, D. Costenaro, F. Carniato, C. Bisio, S.M. Zakeeruddin, M.K. Nazeeruddin, L. Marchese, M. Graetzel, *J. Mater. Chem. A*, **2013**, 1, 10142-10147.

[26] G. Gatti, D. Costenaro, C. Vittoni, G. Paul, V. Crocellà, E. Mangano, S. Brandani, S. Bordiga, M. Cossi, L. Marchese, C. Bisio, *Phis. Chem. Chem, Phys.*, **2017**, 19, 14114--14128

[27] J.M.R. Gallo, C. Bisio, G. Gatti, L. Marchese, H.O. Pastore, *Langmuir*, **2010**, 26, 5791-5800.

[28] S. Lowell, J.E. Shields, M.A. Thomas, M. Thommes, *Kluwer Academic Publishers*, **2004**.

[29] F. Hoffmann, M. Cornelius, J. Morell, M. Fröba, Angew. *Chem. Int. Ed.*, **2006**, 45, 3216-3225.

[30] M. Thommes, K. Kaneko, A.V. Neimark, J.P. Olivier, F. Rodriguez-Reinoso, J. Rouquerol, K.S.W. Sing, *Pure Appl. Chem*., **2015**, 87(9-10), 1051–1069.

[31] M. Kruk, M. Jaroniec, *Chem. Mater*., **2000**, 12, 1961-1968

[32] F. Cucinotta, F.Carniato, G. Paul, S. Bracco, C. Bisio, S. Caldarelli, L. Marchese, *Chem. Mater*., **2011**, 23 (11), 2803-2809.

[33] S.H. Kim, O.C. Han, J.K. Kim, K.H. Lee, *Bull. Korean Chem. Soc*., **2011**, 32 (10), 3644.

[34] A.D. Becke, *Phys. Rev. B*, **1988**, 38, 3098- 3105.

[35] C. Lee, W. Yang, R.G. Parr, *Phys. Rev. B*, **1988**, 37, 785-791.

[36] T.H. Dunning, *J. Chem. Phys*., **1989**, 90, 1007-1010.

[37] R.A. Kendall, T.H. Dunning, R.J. Harrison, *J. Chem. Phys*., **1992**, 96, 6796-6801.

[38] P.J. Hay, W.R. Wadt, *J. Chem. Phys.*, **1985**, 82, 270-279.

[39] T. Schwabe, S. Grimme, *Phys. Chem. Chem. Phys*., **2006**, 8, 4398-4404.

[40] P. Ugliengo, M. Sodupe, F. Musso, I. J. Bush, R. Orlando and R. Dovesi, *Adv. Mater*., **200**8, 20, 4579–4583.

[41] M.W. Hahn, M. Steib, A. Jentys, J.A Lercher, *J. Phys. Chem. C*, **2015**, 119, 4126-4135.

[42] Z.F. Tran, D. Busche, B. Fryxell, L. Addleman, R. Zemanian, T. Aardahl, L. Christopher, *Ind. Eng. Chem. Res*., **2005**, 44, 3099-3105.

[43] G. Socrates, *John Wilwey & Sons*, LTD, **2001**.

[44] C. Knofel, C. Martin, V. Hornebecq, P.L. Llewellyn, *J. Phys. Chem. C*, **2009**, 113, 21726-21734.

[45] X. Wang, W. Schwartz, J.C. Clark, X. Ma, S.H. Overbury, X. Xu, C. Song, *J. Phys. Chem. C*, **2009**, 113, 7260-7268.

[46] H.Y. Huang, R.T. Yang, D. Chinn, C.L. Munson, *Ind. Eng. Chem. Res*., **2003**, 42, 2427-2433.

[47] S. Hao, H. Chang, Q. Xiao, Y. Zhong, W. Zhu, *J. Phys. Chem. C*, **2011**, 115, 12873-12882.

[48] Z. Bacsik, R. Atluri, A.E. Garcia-Bennett, N. Hedin, *Langmuir*, **2010**, 26, 10013-10024.

[49] N. Hiyoshi, K. Yogo, T. Yashima, *Chemistry Letters*, **2004**, 33, 510–511.

[50] A. Danon, P.C. Stair, E. Weitz, *J. Phys. Chem. C*, **2011**, 115, 11540–11549.

[51] O. Leal, C. Bolivar, C. Ovalles, J.J. Garcia, *Inorg. Chim. Acta*, **1995**, 240, 183–189.

[52] S. Brandani and D. M. Ruthven, *Adsorption*, **1996,** 2, 133–143.

[53] F. Brandani, D. M. Ruthven and C. G. Coe, *Ind. Eng. Chem. Res*., **2003**, 42, 1451–1461.

Chapter 4

CO_2 Adsorption on Amino-functionalized MCM-41 Silicas: Influence of Particle Size

Introduction

As described in Chapter 1, numerous studies regarding the CO_2 adsorption using solid adsorbents are reported in literature. These materials can be categorized as physical or chemical adsorbents: in particular, zeolites, carbons and metal organic frameworks belong to the class of physisorbent solids, while hydrotalcites, metal oxides and hybrid organic-inorganic materials containing basic groups are included in chemisorbent category. [1] In fact, in the latter case, carbon dioxide is retained mainly through chemical reactions.

CO_2 capture by physisorption requires less energy respect to chemisorption. This is due to the fact that during physisorption no covalent bonds are formed, and therefore less energy is needed for the adsorbents regeneration. [2]

Moreover, for physisorbent materials the adsorption capacity decreases by increasing the temperature, while chemisorbent solids behave in the opposite way. [3]

Considering the typical stack temperatures of a power plant, solid adsorbers should preferably operate in a range between 30 and 150 °C. [4] For these reasons, materials that adsorb CO_2 through chemisorption processed (*i.e.* hybrid organic-inorganic materials containing amino groups) are preferable, because allow operating at higher temperatures. In addition, chemisorbents are preferable due to the low concentration of CO_2, because they can have potentially higher capacity at very low partial pressures.

Even if hybrid mesoporous materials are considered chemical adsorbers, part of CO_2 can also be retained by means of physisorption processes (*i.e*. physical adsorption in material's porosity). Therefore, in order to understand the behaviour of these materials with the temperature, it is necessary not only to distinguish but also to quantify the physisorption and chemisorption processes.

Many papers focused on hybrid organic-inorganic materials containing amino-groups are reported in the literature. In addition to organo-modified SBA-15 silicas (described in Chapter 3), other mesoporous hybrid materials largely studied are based on MCM-41 silica.

For example Mello et al. grafted commercial MCM-41 silica with 3-aminopropyltrimethoxysilane thus obtaining an adsorbent with CO_2 adsorption capacity of *ca*. 0.70 mol/kg at 20 °C and 0.1 atm [5].

However, to our knowledge, no studies on the effect of the MCM-41 particle size have been reported in the literature. Therefore, in this chapter, MCM-41-based adsorbents with different particle diameter (passing from micrometric to nanometric scale) have been studied.

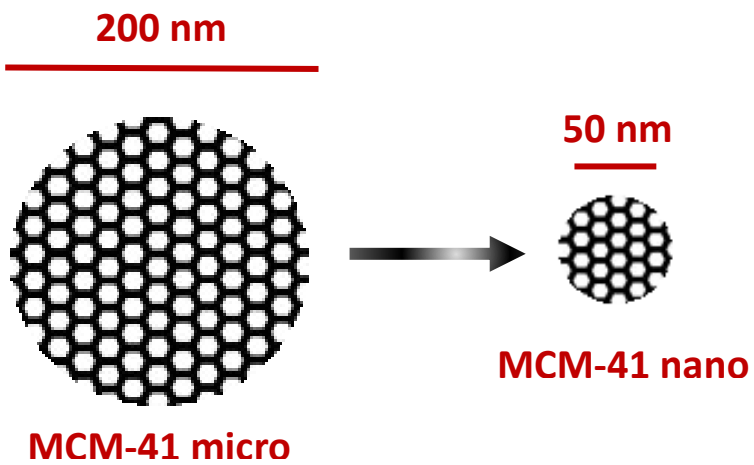

Figure 4.1. Schematic representation of the reduction of particle size of MCM-41 samples.

On the basis of the results obtained in Chapter 3, the solids have been modified via grafting of 3-[2-(2-aminoethyl)aminoethyl]aminopropyltrimethoxysilane (PAPTS). On these materials, a study of the carbon dioxide adsorption processes, especially focused on the reversibility of the reactions between CO_2 and amino groups, was carried out and it is reported in this Chapter. Moreover, particular attention will be given to the distinction between carbon dioxide physisorption and chemisorption processes, by using a combination of FTIR and SS-NMR spectroscopies.

Finally, a study of the CO_2 adsorption process at different temperatures (from 35°C to 90°C) will be reported, in order to investigate the temperature dependence of MCM-41 based hybrid adsorbers.

In detail, in this Chapter will be reported:

- the synthetic procedures of MCM-41 based materials with different particle size (Paragraphs 4.1 and 4.2);
- the physico-chemical properties of MCM-41 materials after functionalization with PAPTS (Paragraph 4.3);
- the evaluation of the CO_2 adsorption properties (Paragraph 4.4) and CO_2 capture capacities (Paragraph 4.5) of the hybrid adsorbents;
- the study of the carbon dioxide adsorption at different temperatures (Paragraph 4.6).

4.1 The MCM-41 Silica

In 1990, researchers from Mobil Corporation Laboratories discovered a synthesis method for the preparation of mesoporous silica, characterized by the presence of ordered arrays of regular pores and high specific surface area. Different type of mesoporous silicas (named MCM-n) were thus produced, including MCM-41 (Mobil Crystalline Material number 41) sample [6].

MCM-41 silica presents a regular hexagonal array of pores, which are separated by thin walls of amorphous silica with a thickness ranging between 0.8 and 1.3 nm (Figure 4.2). [7]

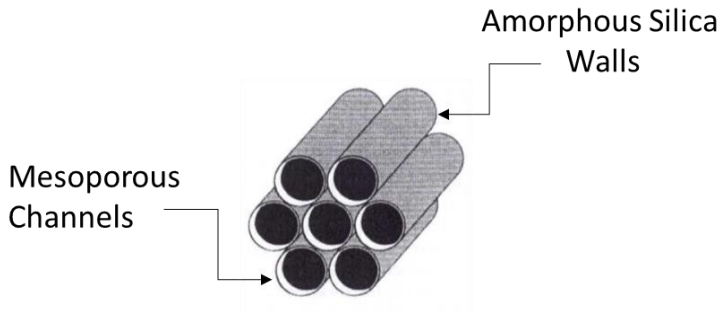

Figure 4.2 Schematic representation of MCM-41 pore structure.

Due to its highly ordered structure, MCM-41 presents an elevated Specific Surface Area (*S.S.A* ≈ 1000 m^2/g) and a pore distribution centred at *ca.* 35-38 Å [8].
This material is largely studied in literature for catalytic applications,[9] encapsulation of luminescent molecules, adsorption of hydrocarbons from water, separation of biological and pharmaceutical compounds. [8, 10] and, as studied in the frame of this PhD thesis, CO_2 capture and storage technologies.

4.1.1 Synthesis Mechanisms of MCM-41 Silica

As for SBA-15 silica, the synthesis procedure of MCM-41 silica occurs by sol-gel process (described in Paragraph 1.2.1). In the synthesis of MCM-41 silica however, cetyl trimethylammonium bromide sufactant (CTAB, Figure 4.3) is used to introduce ordered mesoporosity. This surfactant in water, at concentrations higher than the critical micellization concentration, may form spherical micelles of *ca.* 90 molecules [11]. In the micelle, the hydrophilic head groups form the outer surface and the hydrophobic tails point toward the centre.

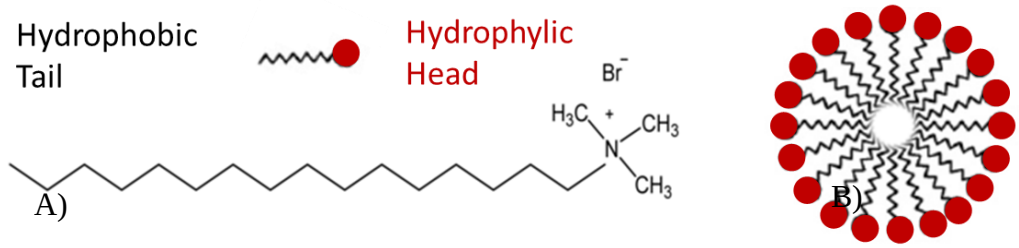

Figure 4.3 A) Schematic representation of CTAB surfactant and B) Schematic representation of the micelle formation in CTAB surfactant.

Two mechanisms are proposed in the literature for the synthesis of MCM-41 mesoporous silica: i) liquid crystal templating mechanism, ii) charge density matching mechanism and iii) silicatropic liquid crystals mechanism. The first mechanistic pathway is reported in Paragraph 3.2.1, because it is the same mechanism proposed for the formation of SBA-15 silica. According to the charge density matching mechanism instead, [12] the initial phase formed during the synthesis is a layered structured. This is due to the electrostatic attractive force of between oppositely charged cationic surfactant head groups and anionic precursor species. The subsequent condensation step causes the reduction in charge density of silicate species, which forces them to balance the charge density by introducing curvature into layers. As a result, lamellar structure is transformed into hexagonal mesophase. A schematic representation of this mechanism is proposed in Figure 4.4.

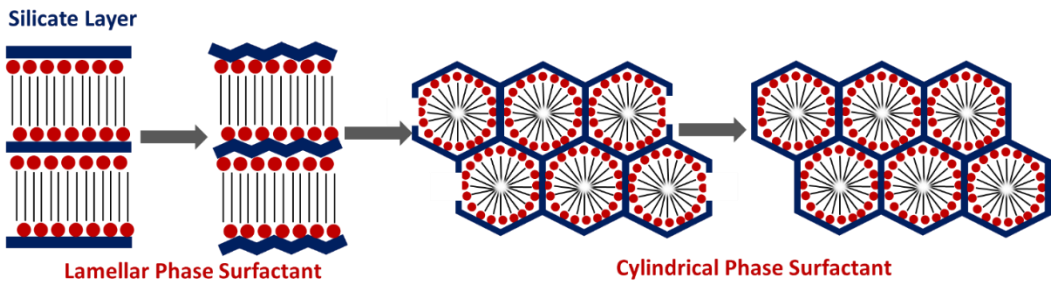

Figure 4.4 Schematic representation of charge density matching mechanism.

Finally, in silicatropic liquid crystals mechanism, CTAB transforms to hexagonal phase in the presence of silicate ions. [13] Silicate precursors, which are negatively charged ions, ion-exchange with surfactant halide counter ions and produce a "silicatropic liquid crystals" phase (SLC). SLC phase displays the same characteristic features of lyotropic systems at low surfactant concentration.

4.1.2 MCM-41 Silica: from Micrometric to Nanometric Size

The traditional preparation method of MCM-41 silica leads to the formation of particles with micrometric size. However, it is possible to modify the synthesis method in order to obtain particles with smaller size. For example, MCM-41 silica particles with dimension between 20 and 50 nm can be obtained by introducing during the synthesis a non ionic triblock copolymer, Pluronic F127, together with the cationic surfactant (cetyl trimethylammonium chloride, CTAC). [14] CTAC surfactant act as a template, as in the traditional the synthesis of MCM-41, while Pluronic F127 is used to suppress the grain growth and thus control the size of silica particles.

In detail, the two templates are dissolved in acidic environment and then the precursor of the silicon is added (*i.e*. tetraethylorthosilicate, TEOS). Hydrolysis and condensation reactions are promoted in acidic conditions, because the presence of protons favours both the release of an ethanol molecule from the TEOS, leading to the formation of silanols, and the release of ethanol or water during the condensation reaction, thus forming of Si-O-Si bonds. Following the solution is tourned into basic conditions by the addition of ammonia, in order to allow the silicates to be aggregated around template micelles. Then nucleation and crystalline growth of the silica occurs, with formation of hexagonal structures. Finally, since the polarity of the aggregates decreases with the aggregation of the anionic and cationic species, the non ionic co-template can surround the silica-CTAC aggregates, blocking the growth and controlling the particle size. Figure 4.5 shows a diagram of the synthesis method of nanosized MCM-41 silica particles.

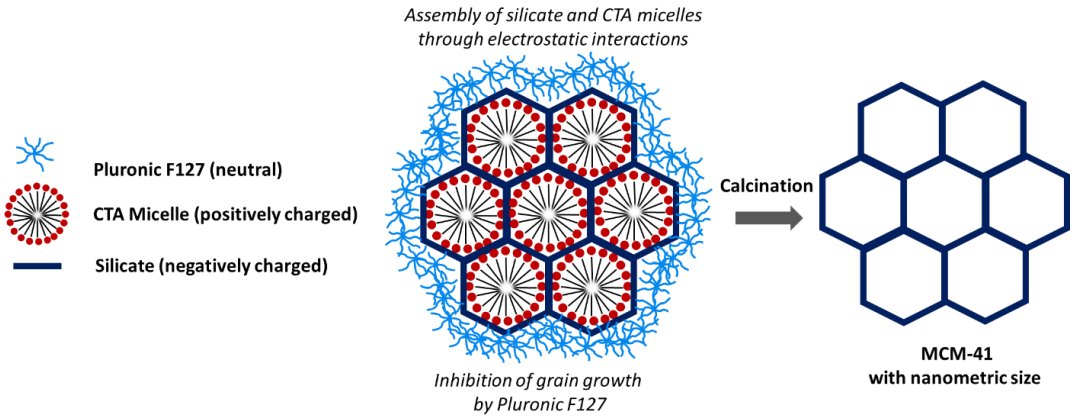

Figure 4.5 Schematic representation nanosized MCM-41 silica particles formation.

4.2 Materials Preparation

4.2.1 Synthesis of Classic MCM-41Silica

In order to obtain MCM-41 silica with micrometric size, cetyl trimethylammonium bromide (CTAB, 15.12 g, Sigma Aldrich, ≥ 98%) was dissolved in 38 mL of deionized water and then heated at 50°C. Tetramethylammonium hydroxide (TMAOH, 8.94 mL, Sigma-Aldrich) was then added, and after 30 minutes silica fumed (5.0 g, Aldrich, 99.8%) was introduced. After 1 h the gel was transferred in a Teflon cup (125 mL capacity) of an autoclave (Anton PAAR 4748) and heated in an oven at 120°C for 72 h. After the hydrothermal treatment, the sample was filtered, washed with deionized water and dried overnight at 120°C. The material was calcined under air flow at 600°C for 5 h (1°C/min heating ramp) in order to remove completely the CTAB surfactant. [15]

The sample obtained will be hereafter named MCM-41 micro.

4.2.2 Synthesis of Nanosized MCM-41 Silica

In order to obtain nanosized mesoporous MCM-41 particles, cetyl trimethylammonium chloride (CTAC, 2.6 g, Sigma Aldrich, ≥ 98%) and Pluronic F127 (2.0 g, Sigma Aldrich) were dissolved in a 0.3 M hydrochloric acid solution (30 g, Sigma Aldrich, ≥37%) at room temperature, and tetraethylorthosilicate (TEOS, 3.5 g, Sigma Aldrich) was then added to the solution. After stirring for 3 h, 3.0 g of ammonium hydroxide solution (Riedel-de Haën, 33%) was introduced. The gel obtained was aged by stirring at room temperature for 24 h and then heated in a thermostatic bath at 60°C for 24 h. The sample obtained was filtered, washed with distilled water and then dried at room temperature overnight. The surfactants were finally removed from the sample by calcination at 600°C in air flow for 3 h (ramp temperature: 1 °C/min). [14]

The sample obtained will be hereafter named MCM-41 nano.

4.2.3 Functionalization of MCM-41 Silicas

Both MCM-41 silica samples were functionalized with N-[3-(trimethoxysilyl)propyl]-diethylenetriamine (PAPTS) by using a post-synthesis grafting method in order to introduce amino groups on the silica surface. The method followed was the same of the one used for the functionalization of SBA-15 silica (Paragraph 3.3.2).

The obtained hybrid samples will hereafter named P_MCM-41 micro and P_MCM-41 nano.

4.3 Physico-chemical Characterization

4.3.1 Structural, Morphological and Textural Analysis

The structural properties of hybrid MCM-41 samples were studied by XRD analysis (Figure 4.6).

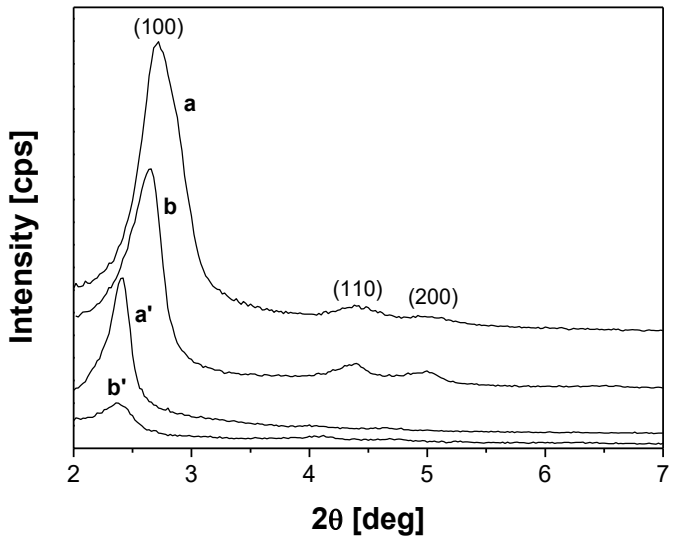

Figure 4.6 XRD patterns of MCM-41 micro (a), MCM-41 nano (b), P_MCM-41 micro (a'),P_MCM-41 nano (b'). [16]

The diffraction pattern of MCM-41 micro and nano samples (Figure 4.6, curves a, b) shows reflections at 2.7, 4.3 and 5.0° 2Θ degree, corresponding to the families (100), (110) and (200) of planes. These reflections are typical of materials with ordered hexagonal arrangement of cylindrical pores.[15] Instead, grafted MCM-41 silica samples (Figure 4.6, curves a', b') show mainly the basal reflection at 2.4° 2Θ degree, indicating that the introduction of the PAPTS silane decreases the structural order typical of MCM-41 materials.[16]

In addition, the morphology of MCM-41 silica samples was studied by using transmission electron microscopy (TEM). The obtained images of MCM-41 samples are reported in Figure 4.7.

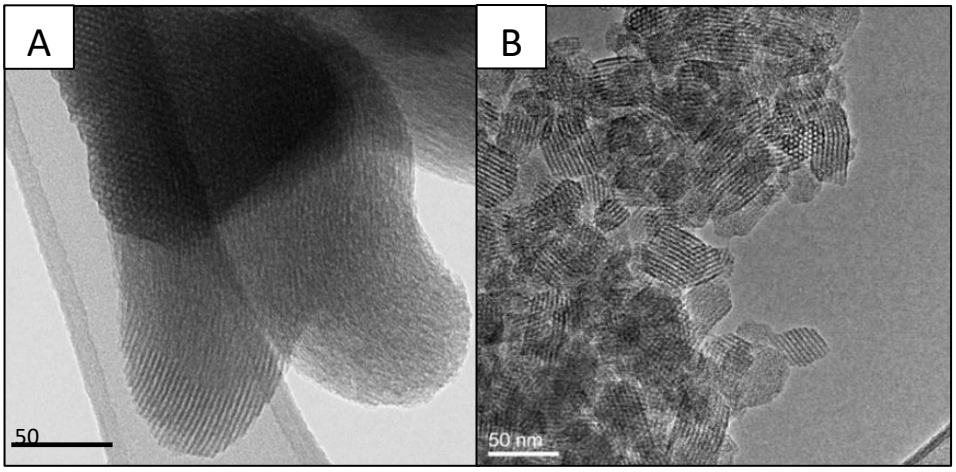

Figure 4.7 TEM micrographs of MCM-41 micro (A) and MCM-41 nano samples (B). [16]

As we can see in Figure 4.7 A, MCM-41 micro sample is composed by micrometric particles with a mean diameter of about 200-300 nm and presents the typical ordered arrangement of pores. MCM-41 nano sample instead (Figure 4.7, Frame B) preserves the same ordered structure, but the mean diameter of particles is reduced to about 40 nm. [17] The size reduction of MCM-41 nano sample, compared to MCM-41 micro, is due to the introduction during the synthesis of an additional surfactant (Pluronic F127), which limits the growth of the grains, controlling the size of the silica particles [14,16].

In order to collect information on the textural properties of MCM-41 grafted samples, N_2 physisorption analysis at 77K was carried out, with special attention to the determination of specific surface area and pore size distribution. N_2 adsorption-desorption isotherms and pore size distribution are reported in Figure 4.8.

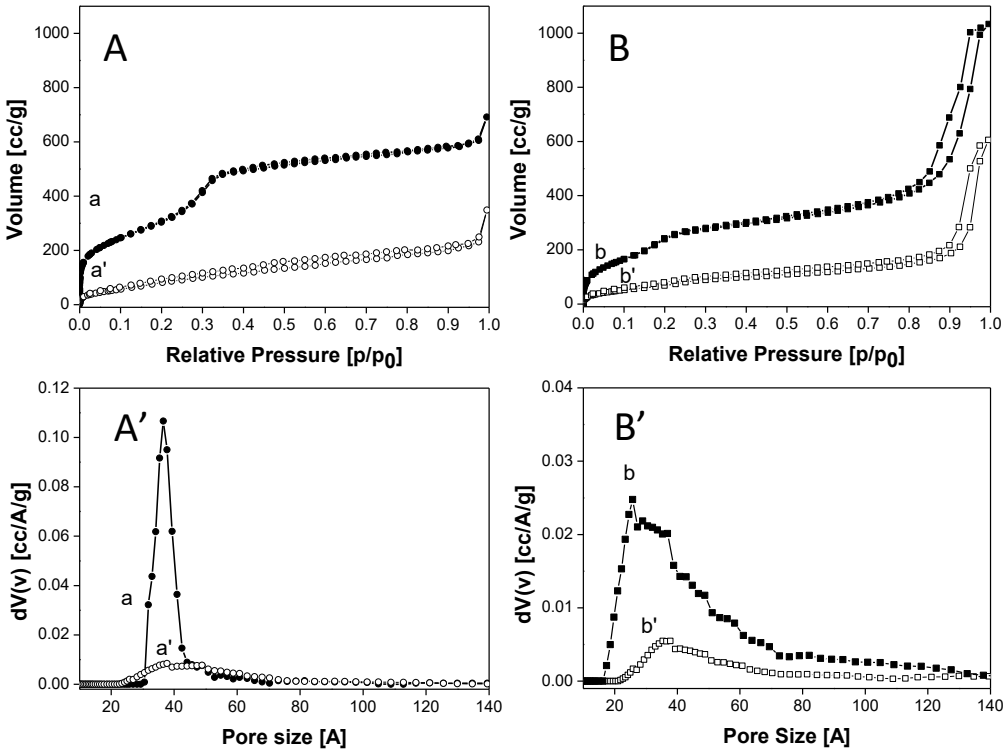

Figure 4.8 N_2 adsorption-desorption isotherms at 77 K and relative pressures (P/P_0) from $1*10^{-7}$ to 1 (frames A, B) and pore size distribution determined by NLDFT methods (frames A', B') of MCM-41 micro (a), P_MCM-41 micro (a'), MCM-41 nano (b) and P_MCM-41 nano (b'). [16]

MCM-41 micro and nano samples (Figure 4.8, frames A,B, curves a, b) show type IV adsorption isotherms based on the IUPAC classification, indicating the presence of ordered mesoporosity in the samples.[18] In addition, MCM-41 nano sample presents a hysteresis loop at high P/P_0 values, not observable in microsized sample, due to the aggregation of small particles. After the grafting procedure, the shape of the isotherm in both samples is modified. In particular, the volume of nitrogen adsorbed is decreased in the functionalized samples.

The specific surface area (S.S.A), estimated by using BET method, and pore volume values are showed in Table 4.1. Before the functionalization the specific surface area values of MCM-41 micro and MCM-41 nano samples are 1205 and 893 m^2/g, respectively. After the grafting of PAPTS, a reduction of specific surface area values

respect to the bare MCM-41 silicas is observable (about -70% for both samples). This decreasing can be attributed to the presence of the organic chains that limit the access to the pores. Despite P_MCM-41 micro contains about the same amount of NH_2 groups as P_MCM-41 nano (about $1*10^{-2}$ mmol/m^2, data reported in Table 1), the pore volume decreases more (-60% for P_MCM-41 micro, -45% for P_MCM-41 nano), suggesting that for P_MCM-41 micro the organic chains are present mostly inside the pores, while for P_MCM-41 nano the species are grafted mostly onto the external surface. This effect should be related to the reduced pore size of MCM-41 nano compared to MCM-41 micro sample (Figure 4.8, sections A' and B'), that is in part limiting the access of the organosilane into the pores (length of PAPTS chain: 8.9 Å, see Paragraph 2.4). [16]

Sample	**SSA [m^2/g]**	**Vp [cc/g]**	**Conc. N [mmol·g^{-1}]**	**Conc. N [mmol·m^{-2}]**
MCM-41 micro	1205	0.894	-	-
P_MCM-41 micro	372	0.363	3.57	$0.95*10^{-2}$
MCM-41 nano	893	1.552	-	-
P_MCM-41 nano	268	0.864	3.17	$1.1*10^{-2}$

Table 4.1. Specific surface area and total pore volume values obtained by N_2 physisorption analysis and nitrogen concentration values of MCM-41 and hybrid related samples determined by elemental analysis. [16]

4.3.2 Surface Properties of MCM-41 Hybrid Materials

The presence of the PAPTS on the surface of MCM-41 silica particles was monitored by infrared spectroscopy. Spectra of the samples before and after the functionalization are given in Figure 4.9.

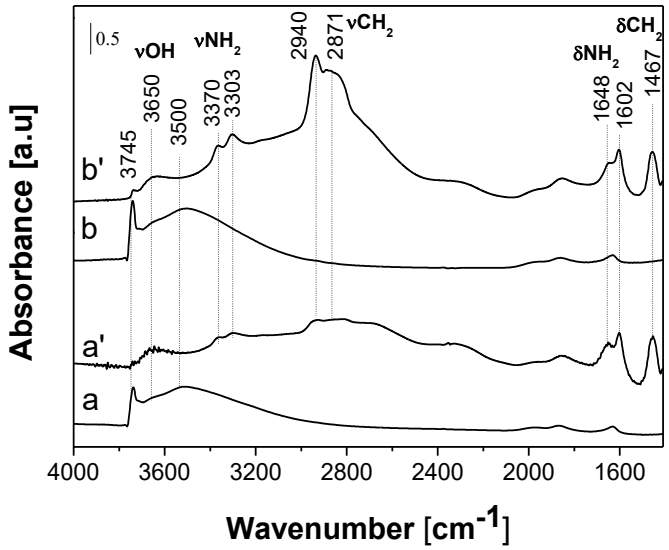

Figure 4.9 FT-IR spectra of MCM-41 micro (a), P_MCM-41 micro (a'), MCM-41 nano (b) and P_MCM-41 nano (b') samples. Spectra were recorded after outgassing of the materials at 100°C for 1 h to remove the water physisorbed on the surface. [16]

The FT-IR spectra of the bare MCM-41 silica samples (Figure 4.9, curves a, b) shows in the high frequency range a band located at 3745 cm^{-1} and a broad adsorption in the 3700-3000 cm^{-1} region, in which bands at ca. 3650 and 3500 cm^{-1} are present. The sharp component at 3745 cm^{-1} is ascribed to the stretching mode of isolated SiOH groups, whereas the broad absorption at lower frequencies is due to the stretching mode of hydrogen-bonded OH groups weakly interacting with each other [19]. In particular, it can be noticed that in MCM-41 nano sample (Fig. 4.9, curve b) the intensity of these bands is more intense compared to the MCM-41 micro sample, thus indicating the presence of a greater number of silanol groups (both isolated and H-bonded) compared to the other sample (Fig. 4.9, curve a). This observation is also confirmed by the quantitative determination of the silanol concentration performed by TGA analysis: 2.78 SiOH/nm^2 for MCM-41 micro and 3.16 SiOH/nm^2 for MCM-

41 nano sample, respectively (further details on the quantitative determination are reported in Chapter 3, Paragraph 3.4.2).

In the low frequency region, the spectra of both materials show bands at *ca*. 1980, 1865 and 1600 cm^{-1}, due to the overtones and combination modes of the silica framework [20].

After the grafting procedure (Figure 4.9, curves a', b') the bands due to surface silanols, both isolated and hydrogen-bonded, are strongly decreased in intensity. This effect is due to the fact that these species: i) react with the grafted organic chain and ii) are hydrogen bonded with the PAPTS amino groups.

Moreover, the infrared spectra of both grafted samples are characterized by the presence of a broad band 3500–2000 cm^{-1} region, in which a series of complex absorptions are visible. This broad band is due to the occurrence of strong H-bonds between the silanols and the amino groups of the PAPTS chain, which are bent towards the silica surface. [21] In particular, in this region are present components at 3370 and 3303 cm^{-1} due to the asymmetric and symmetric stretching modes of amino groups, respectively; the associated bending mode falls at 1602 cm^{-1}.[19] Moreover, in the 3000-2800 cm^{-1} range are present also bands due to the asymmetric and symmetric stretching modes of CH_2 groups of the silane grafted onto the silica surface; the associated bending mode falls at 1467 cm^{-1}. [19] Finally, the band at 1648 cm^{-1} can be associated to the bending mode of the NH groups content in the PAPTS chain. [19] [16]

4.4 Study of the Interaction between MCM-41-based Hybrid Samples and CO_2

Infrared spectroscopy of adsorbed carbon dioxide was used to evaluate the interactions between CO_2 and the organo-modified MCM-41 mesoporous silicas. Experimental details are given in Paragraph 3.5. Infrared spectra collected after the

admission of 60 mbar of CO_2 at 35°C on the hybrid samples are reported in Figure 4.10.

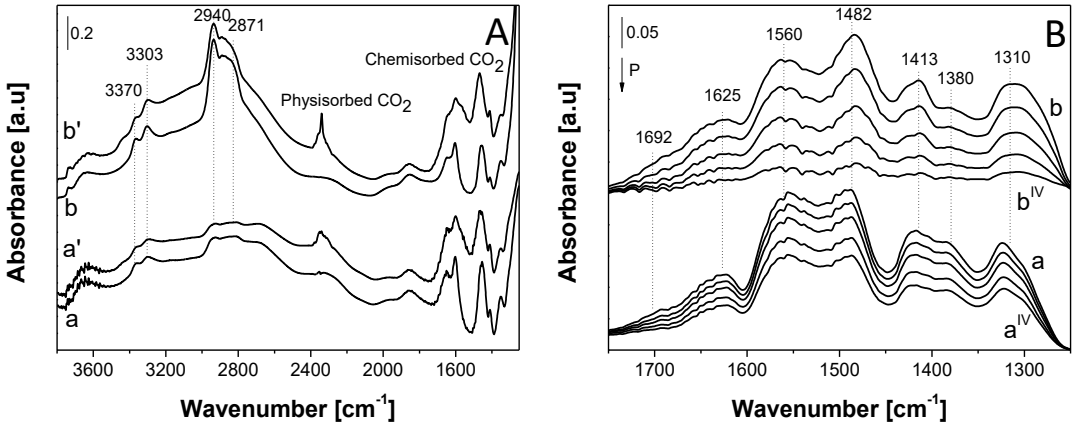

Figure 4.10. Frame A: FTIR spectra in the 3800-1250 cm^{-1} region of P_MCM-41 micro (a) and P_MCM-41 nano (b) before (curves a, b) and after the admission of 60 mbar of CO_2 at 35°C(curves a',b'). Spectra are reported after subtraction of the spectrum of gaseous CO_2. [16] Frame B: FTIR spectra, in the 1750–1250 cm^{-1} region, of CO_2 adsorbed (Pmax = 60 mbar) at 35°C on P_MCM-41 micro (a-a^{IV}) and P_MCM-41 nano (b-b^{IV}). The arrows indicate decreasing CO_2 pressure until vacuum. Spectra are reported after subtraction of the spectrum recorded before CO_2 interaction, used as a background, and after the subtraction of the spectrum of gaseous CO_2. [16]

After the introduction of 60 mbar of CO_2, the IR spectrum of P_MCM-41 micro sample (Figure 4.10 A, curve a') appears strongly modified. In particular, bands at 3370 and 3303 cm^{-1}, related to the stretching modes of NH_2 groups, appear decreased in intensity, thus indicating that part of these groups are involved in the reaction with CO_2, thus forming ammonium carbamate and carbamic acid.[22] At lower frequencies, bands due to both physisorbed and chemisorbed carbon dioxide are visible. The stretching mode of physisorbed CO_2 is located at 2341 cm^{-1}, whereas bands due to products of the chemical reaction between amino groups and CO_2 fall in the region between 1750 and 1250 cm^{-1}. In order to better appreciate these bands, in Figure 4.10 B are reported spectra after subtraction of the spectrum of the bare sample (*i.e.* before CO_2 admission). In particular, bands located at 1560, 1482 and

1413 cm^{-1} are related to the formation of carbamate species and bands at 1692 and 1380 cm^{-1} are ascribed to the formation of carbamic acid [21, 23, 24, 25] (a detailed description of the assignation of these bands is given in Paragraph 3.5). In addition, the band at 1625 cm^{-1} is attributed to the asymmetric bending of NH_3^+ species, probably deriving from the interaction of NH_2 species with carbamic acid [23], whereas the band located at 1310 cm^{-1} is due to skeletal vibrations of $NCOO^-$species [26]. The formation of carbamic acid is also confirmed by the increase of the large band between 3500 and 2000 cm^{-1}, thus indicating an interaction of the amino groups at the silica surface. By decreasing progressively the CO_2 pressure (Figure 4.10 B, curves a^I- a^{IV}) bands related to both carbamic acid and carbamate species progressively decrease in intensity, indicating that part of the reaction products are removed by the outgassing procedure. [16] The carbon dioxide adsorption on P_MCM-41 nano (Fig. 4.10, curve b') also leads to the formation of physisorbed and chemisorbed species. In order to compare the results obtained for the two samples in terms of physisorbed species, the obtained difference spectra are reported in Figure 4.11.

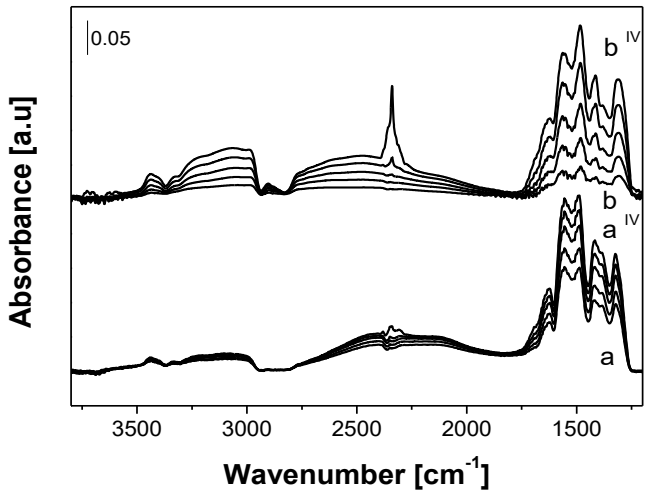

Figure 4.11. FTIR spectra of carbon dioxide adsorbed (Pmax = 60 mbar) at 35°C on P_MCM-41 micro (a-a^{IV}) and P_MCM-41 nano (b-b^{IV}). The arrows indicate decreasing CO_2 pressure until vacuum. Spectra are reported after subtraction of the spectrum recorded before CO_2 interaction, used as a background. [16]

In Figure 4.11 it can be observed that physically adsorbed (band at 2341 cm^{-1}) carbon dioxide is much more abundant in the P_MCM-41 nano sample probably because of its higher pore volume compared to P_MCM-41 micro: 0.864 $cc \cdot g^{-1}$ and 0.363 $cc \cdot g^{-1}$, respectively (Paragraph 4.3, Table 4.1). However, taking into account the low CO_2 pressure, the sample is far from the saturation conditions, and therefore this behaviour may be due to a different affinity and strength of the adsorption sites. Concerning the species formed during chemisorption, after the evacuation (Figure 4.10, Frame B, curves a^{IV} and b^{IV}) it can be seen that the related bands are more intense for MCM-41 micro sample with respect to MCM-41 nano, thus indicating that a greater amount of stable ammonium carbamates and carbamate acids is present in the micrometric sample. In fact, the desorption process is different for the two samples: in P_MCM-41 nano the bands decrease faster and remain less intense, while in MCM-41 micro the bands decrease less rapidly and remain well visible also at the end of desorption. This effect is also supported by the fact that the broad band in the 3500-2000 cm^{-1} range after evacuation is more pronounced for P_MCM-41 micro than for P_MCM-41 nano (Figure 4.11), thus indicating a stronger interaction between carbamic acid and the amino groups. This difference of the stability of carbamate species is probably due to the location of NH_2 groups grafted on the silica surface: in P_MCM-41 nano more amino groups are present on the external surface, outside the pores, and probably the formed carbamates are less protected by the confinement effects compared to P_MCM-41 micro. [16]

The CO_2 adsorption process was further studied by using ^{13}C MAS NMR spectroscopy (Figure 4.12).

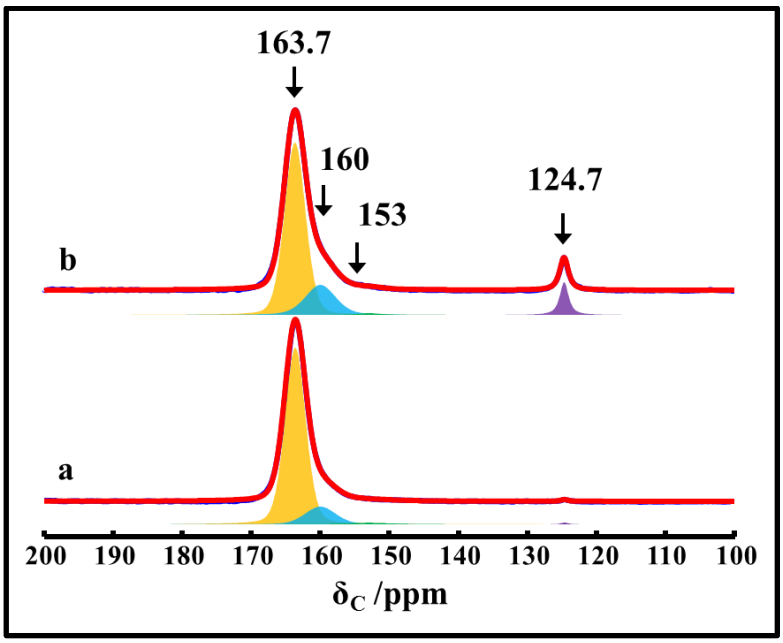

Figure 4.12. ^{13}C MAS NMR spectra of $^{13}CO_2$ adsorbed on P_MCM-41 micro (a) and P_MCM-41 nano (b) recoded using a MAS rate of 10 kHz. Figure includes experimental and its deconvoluted spectrum with individual contribution from each ^{13}C sites. [16]

^{13}C MAS NMR spectra of micro and nano P_MCM-41 samples show peaks due to both physisorbed and chemisorbed $^{13}CO_2$ species. The peak related to the physisorbed $^{13}CO_2$ is located at 124.7 ppm. Three additional resonances at 163.7, 160 and 153 ppm, typically associated with carbamate carbons formed upon $^{13}CO_2$ chemisorption with the PAPTS amines, are visible. Quantitative data derived from the ^{13}C MAS NMR spectra of P_MCM-41 nano show that about 7% of the total $^{13}CO_2$ is physically adsorbed, while the remaining part is distributed among chemisorbed species. However, the amount of physisorbed $^{13}CO_2$ present in P_MCM-41 micro sample is much smaller (less than 1%). [16] Quantitative estimation of $^{13}CO_2$ adsorbed in different modes is given in Table 4.2.

Chemical shift, δc [ppm]	P_MCM-41 micro [wt%]	P_MCM-41 nano [wt%]
163.7	85	72
160	13	20
153	<2	1
124.7	<1	7

Table 4.2. Quantitative data derived from ^{13}C MAS NMR spectra of $^{13}CO_2$ adsorbed on P_MCM-41 samples. [16]

As we can observe from Table 4.2, the $^{13}CO_2$ distribution in the different forms varies depending on the pore architecture and particle dimension of MCM-41 hybrid samples. The small amount of $^{13}CO_2$ physisorbed on P-MCM-41 sample (in full agreement with the IR findings, *vide supra*), could be due to the reduced pore volume value of this sample (0.363 cc/g) compared to those in nanosized sample (0.864 cc/g, Table 1). In addition, the lower amount of physisorbed $^{13}CO_2$ might be due to hydrogen bonded ammonium carbamates and/or carbamic acid network that blocks the access of gaseous $^{13}CO_2$ to the pores. [16] Two proposed hydrogen bonded network configurations are shown in Figure 4.13.

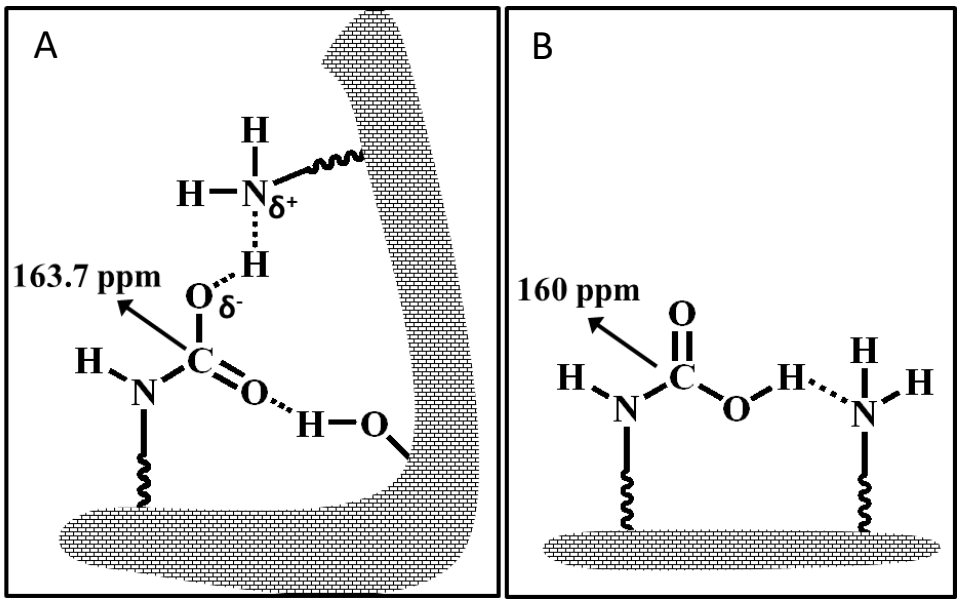

Figure 4.13. Schematic diagram representing two possible models of hydrogen bonding network formed by carbamate and carbamic acid species with surface silanols and neighbouring PAPTS chains. [16]

In P_MCM-41 micro, the 85% of adsorbed $^{13}CO_2$ contributes to the peak at 163.7 ppm. This peak due to a complex hydrogen bonding network involving multiple species (*i.e.* surface silanols and amino groups from PAPTS chains). Such complex network could fill the channels as well as block the access for gaseous $^{13}CO_2$. For this reason, the $^{13}CO_2$ physisorbed contribute is low (less than 1%). However, in P_MCM-41 nano sample, a minor percentage of $^{13}CO_2$ species contributes to the peak at 163.7 ppm (about 72%). That leaves just enough space for the access of gaseous $^{13}CO_2$ to the channels, as seen by the intense peak at 124.7 ppm. [16]

4.5 Evaluation of CO_2 Capture Capacity of Hybrid MCM-41 Samples

The CO_2 adsorption capacity was initially evaluated by performing carbon dioxide adsorption-desorption cycles followed by thermogravimetric analysis by using a Setaram Sensys Evo TG/DSC apparatus. In a typical experiment, *ca.* 30 mg of

sample was packed in a platinum crucible, which was counterbalanced by an identical crucible packed with an equivalent mass of lead beads. Prior the measurements the sample was pre-treated at 135°C for 3 h (2°C/min heating rate) under He flow (50 ml/min). The sample was then cooled to 35 °C, and the adsorption was performed by exposing the sample to a mixture of 10% of carbon dioxide in helium at a constant total flowrate (50 ml/min) for 2 h (typical time of a TSA cycle). The CO_2 concentration and the adsorption time were chosen in order to be representative of a typical post-combustion capture process from a coal-fired power plant. At the end of the adsorption step, the inlet flow is switched to pure He at the same flowrate for 2 h, in order to allow the desorption of carbon dioxide. CO_2 uptake curves of MCM-41 based hybrid samples obtained with thermogravimetric analysis are reported in Figure 4.13.

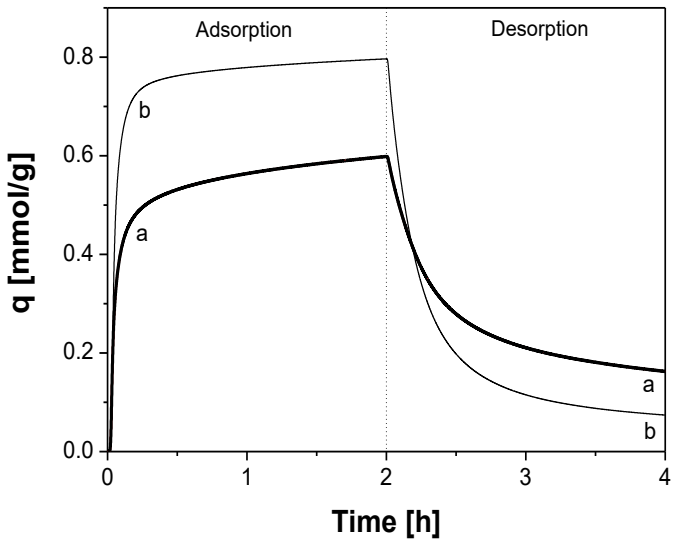

Figure 4.13. CO_2 uptake curves obtained from TGA analysis of P_MCM-41 micro (a) and P_MCM-41 nano (b) silica samples. Measurements were recorded at 35°C, 0.1 bar CO_2-0.9 bar He in adsorption and 1 bar He in desorption. [16]

Gravimetric adsorption curves revealed that P_MCM-41 nano (Figure 4.13, curve b) has a higher CO_2 adsorption capacity (q) compared to P_MCM-41 micro sample (Figure 4.13, curve a). In detail, the CO_2 uptake after 2 h of adsorption are 0.79 and 0.58 mmol/g, respectively for P_MCM-41 nano and P_MCM-41 micro samples. For both materials, during the adsorption a fast initial uptake of carbon dioxide, followed by a second slower process are observable. This is in general an indication of a non-isothermal adsorption process, in which CO_2 molecules are rapidly adsorbed producing a temperature increase and then, as the sample cools down, more molecules are slowly adsorbed. [16] This is confirmed by the temperature profile of the samples and the heat of adsorption measured by TGA/DSC instrument (Figure 4.14, Frames A and B).

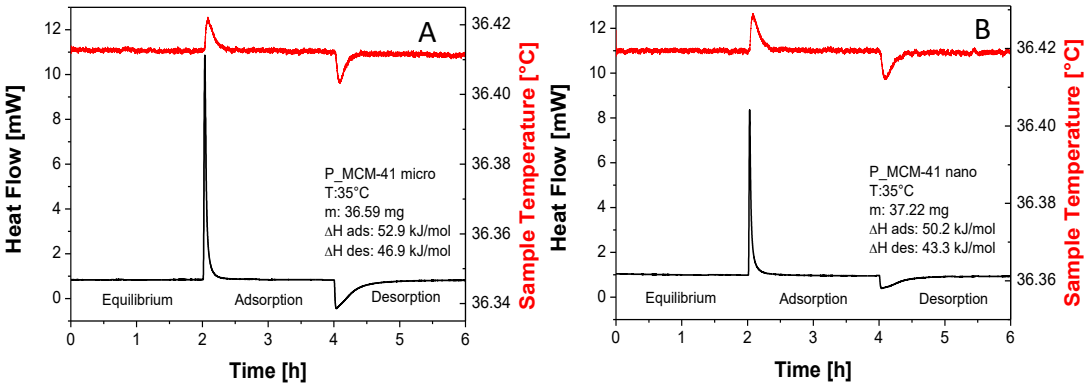

Figure 4.14. Heat Flow and Sample Temperature from DSC-TGA Analysis for P_MCM-41 micro and P_MCM-41 nano samples. [16]

The low variation of the sample temperature observed in Figure 4.14 (about 0.01 °C) is related to the fact that in the system thermocouples are not placed inside the sample, but in the camera where the crucibles are inserted: for this reason, the registered temperature is intermediate between sample and camera temperatures.

In addition, from Figure 4.13 it can be seen that the hybrid silica samples show different adsorption-desorption rate: P_MCM-41 micro shows slower adsorption and

desorption rate compared to P_MCM-41 nano, suggesting a higher contribute of chemical adsorption (even if this effect could also be due to a different reaction, to the transport mechanism, or the heat of adsorption, higher for P_MCM-41 micro sample). This is more evident in the desorption curve, where at the end of the desorption, despite the lower uptake, a higher percentage of CO_2 is retained in microsized sample (*ca*. 27% of the total) compared to the nanosized one (about 9% of the total). It is important to note that in the case of purely physisorption process, assuming that equilibrium has been reached and no transport resistances are present, the amount of carbon dioxide adsorbed and desorbed should be the same, indicating perfectly reversible process. On the contrary, a residual amount of CO_2 after desorption indicates that a portion of carbon dioxide, strongly interacting with the surface, is irreversibly chemisorbed. This is perfectly in agreement with FT-IR Spectroscopy observations. [16]

Adsorption (ΔH_{Ads}) and desorption heats (ΔH_{Des}) of the process can also be calculated from the heat flow measured by the DSC (Figure 4.14) using Equation 4.1, where *m* is the amount of adsorbed CO_2 expressed in moles and *t* is the time.[27]

$$\Delta H = \frac{\int_{t_0}^{t} Heat\ Flow\ dt}{m_t - m_{t_0}} \tag{4.1}$$

The calculated values of ΔH_{Ads} for P_MCM-41 micro and P_MCM-41 nano samples are 52.9 and 50.2 kJ·mol^{-1}, respectively, while the corresponding ΔH_{Des} values are lower (46.9 kJ/mol and 43.3 kJ·mol^{-1}, respectively). The lower desorption heat indicates that the CO_2 desorbed is primarily the physisorbed fraction. In literature, processes with ΔH values lower than 50 kJ/mol are considered to be physisorption, while values greater than 50 kJ·mol^{-1} are considered to be chemisorption [28]. In this case, the adsorption heats of both samples are similar to the limit value (50 kJ/mol), suggesting that both physical and chemical adsorption occur. In addition, the

calculated adsorption heat values of the pristine samples (before the grafting procedure) are 37.1 and 37.9 kJ·mol^{-1} for MCM-41 micro and MCM-41 nano samples, respectively. In these materials only physisorption can occur, because amino groups, which are able to react chemically with the carbon dioxide, are not present. Therefore, it is evident that the increase in the ΔH_{Ads} for P_MCM-41 micro and nano samples is due to the contribution of the chemisorption associated to the amino groups of the PAPTS chains grafted. [16]

The quantitative determination of adsorbed CO_2 was also studied using the ZLC analysis. Figure 4.15 shows the ZLC desorption curves of P_MCM-41 micro sample (section A) and P_MCM-41 nano sample (section B) at 35°C and different flowrates: 2 and 2.7 ml·min^{-1}; the plots include the blank curves (*i.e.* the response of the system when no sample is loaded).

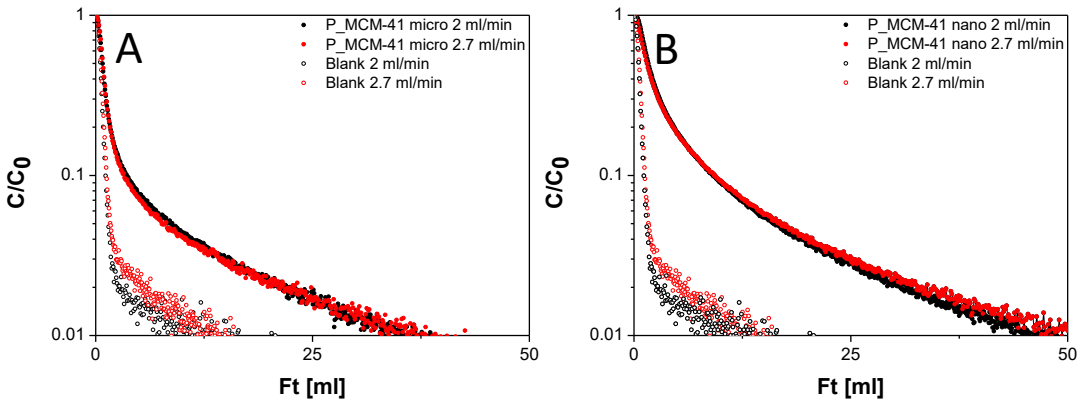

Figure 4.15. ZLC desorption curves for P_MCM-41 micro (frame A) and P_MCM-41 nano sample (frame B) and blank curves at 2 and 2.7 ml/min flow rates. CO_2 partial pressure: 0.1 bar, T: 35°C. [16]

From ZLC desorption curves the carbon dioxide adsorption capacity can be calculated (Paragraph 3.6). The CO_2 capacity values are: 0.349 and 0.58 mmol·g^{-1} for P_MCM-41 micro and P_MCM-41 nano, respectively. These capacity values are significantly lower than those obtained with thermogravimetric analysis. This is due to the fact that ZLC analysis measures the amount of CO_2 desorbed from the sample. For a purely physisorption process this value corresponds to the amount originally

adsorbed on the sample. In our case instead, as it has been observed from FT-IR and TGA analysis, as a portion of CO_2 is chemically bound to the amino groups, and therefore is irreversibly adsorbed. [16]

In order to desorb also the irreversible fraction, and obtain the total adsorption capacity, temperature programmed desorption (TPD) analysis was carried out on P_MCM-41 samples. The obtained TPD curves are reported in Figure 4.16.

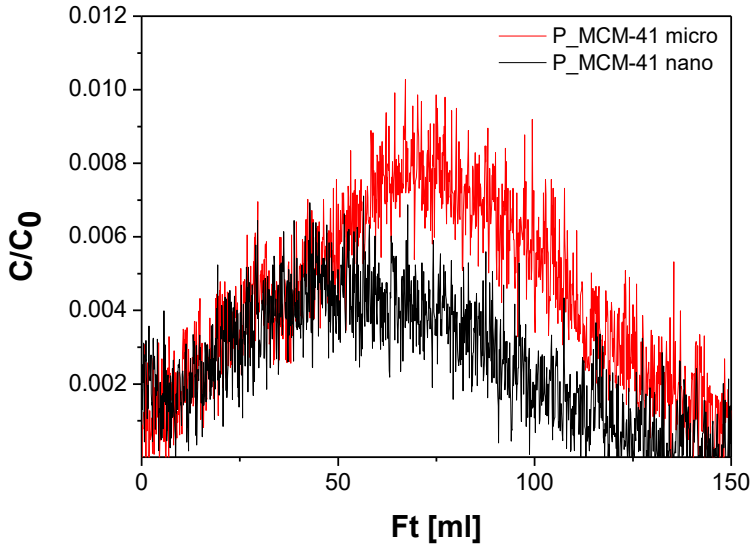

Figure 4.16. Temperature Programmed Desorption curves for P_MCM-41 micro and P_MCM-41 nano sample at 2 ml/min flow rates. CO_2 partial pressure: 0.1 bar. [16]

The fractions of CO_2 irreversibly bonded, obtained by integration of the TPD curves, are 0.16 and 0.06 mmol·g^{-1}, respectively for P_MCM-41 micro and P_MCM-41 nano samples. The largest fraction of irreversible CO_2 observed for P-MCM-41 micro sample compared to P_MCM-41 nano is in accordance with FT-IR observations. Taking into account the amount of irreversible fraction observed with TPD, more accurate values of CO_2 adsorption capacity can be obtained by adding these values to those obtained with ZLC. The total adsorption capacity values obtained are 0.51 and 0.64 mmol·g^{-1} for P_MCM-41 micro and P_MCM-41 nano samples,

respectively. These data are now only slightly lower than the adsorption capacity values obtained by using thermogravimetric analysis. In fact the ZLC experiment was the last performed, and for this reason it was supposed that the loss of capacity could be associated to degradation of the samples. For this reason, a new TGA measurement was carried out on the same nanosized sample used to pack the ZLC. The new measured capacity was 0.63 mmol/g for P_MCM-41 nano sample, confirming that the discrepancy in the values observed in the ZLC experiment are due to degradation of the samples, and that the results obtained with the two techniques are comparable. In addition, the fractions of carbon dioxide adsorbed CO_2 in ZLC analysis accounts are 31 and 9 % of the total amount adsorbed for P_MCM-41 micro and P_MCM-41 nano respectively. This result is in very good agreement with what observed in thermogravimentric experiment. [16]

The CO_2 uptake at 35°C was also studied using a volumetric adsorption analyzer. Before the analysis the samples were outgassed at 135°C for 3 h in order to desorb the water adsorbed on the surface (1°C·min^{-1} heating rate and residual pressure $p < 10^{-6}$ Torr). Volumetric curves are reported in the following Paragraph (Figure 4.22). The values of adsorption capacities obtained are reported in Table 4.3, in comparison with ZLC and TGA analysis.

Sample	**Adsorption Capacity [mmol·g^{-1}]**		
	Volumetry	**TGA**	**ZLC**
P_MCM-41 micro	0.62	0.58	0.51
P_MCM-41 nano	0.79	0.79	0.64

Table 4.3. Adsorption Capacity values obtained with Thermogravimetric Analysis, Volumetric Analysis and Zero Length Column chromatography. [16]

In Table 4.4, for a direct comparison, the irreversible chemisorption fraction values obtained with ZLC, TGA and Volumetric Analysis are reported.

Sample	Irreversible Fraction [mmol·g^{-1}]		
	Volumetry	**TGA**	**TPD**
P_MCM-41 micro	0.16	0.16	0.16
P_MCM-41 nano	0.06	0.07	0.10

Table 4.4. Irreversible fractions obtained with TPD, TGA and Volumetric Analysis for the hybrid MCM-41 materials. [16]

4.6 CO_2 Adsorption Process: a Temperature Dependence Study

Aiming to study the temperature dependence of the carbon dioxide adsorption process on MCM-41 materials grafted with PAPTS, FT-IR Spectroscopy at different temperature (*i.e.* 35, 50, 70 and 90°C) has been performed. The experiment has been carried out *in situ* by using an IR cell permanently attached to vacuum line (residual pressure: ≤ 1.33x10^{-4} Pa). This specific cell is equipped with a heating system, which allows keeping the sample at a specific temperature during the analysis. Before the gas adsorption tests, the silica samples were outgassed at 135°C for 3 h under dynamic vacuum, using an oil-free apparatus and grease-free vacuum line. The samples have been then cooled at the desired temperature (*i.e.* 35, 50, 70 and 90°C) for the collection of IR spectra upon CO_2 adsorption. The spectra obtained in the 1750-1250 cm^{-1} range are reported in Figure 4.17.

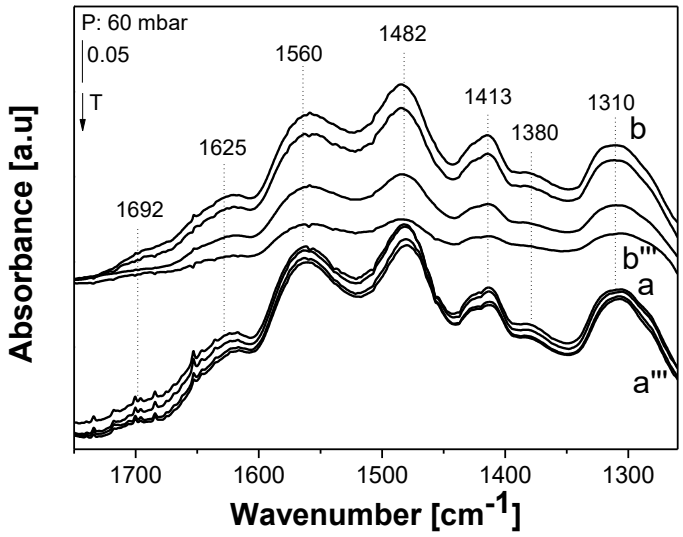

Figure 4.17. FTIR spectra, in the 1750-1250 cm^{-1} region of P_MCM-41 micro (curves a-a^{III}) and P_MCM-41 nano (curves b-b^{III}) after the admission of 60 mbar of CO_2. The arrows indicate increasing temperature 35, 50, 70 and 90°C). Spectra are reported after subtraction of the spectrum recorded before CO_2 interaction, used as background, and the subtraction of the spectrum of the CO_2 gas. [16]

From Figure 4.17 it can be seen that when the temperature increases from 35 to 90°C, the bands due to carbamic acid and carbamates decrease in intensity, and this is particularly evident for P_MCM-41 nano sample. In fact, these products resulting from the interaction between CO_2 and the amino groups are thermally unstable upon heating. [29] This result agrees with previous literature studies, which demonstrated that CO_2 started to be desorbed from amino-functionalized materials above 40°C. [30] The greater stability with the increase of the temperature of the products formed on P_MCM-41 micro compared to the P_MCM-41 nano sample suggests that in the micrometric sample PAPTS chains, and thus the formed products, are located mainly inside the pores; for this reason they are confined and more protected toward decomposition and desorption. [16]

In addition, the temperature dependence of the carbon dioxide adsorption process was studied using the gravimetric method. The CO_2 uptake of the amino-modified MCM-41 silica samples as a function of temperature (from 20 to 90°C) is reported in Figure 4.18.

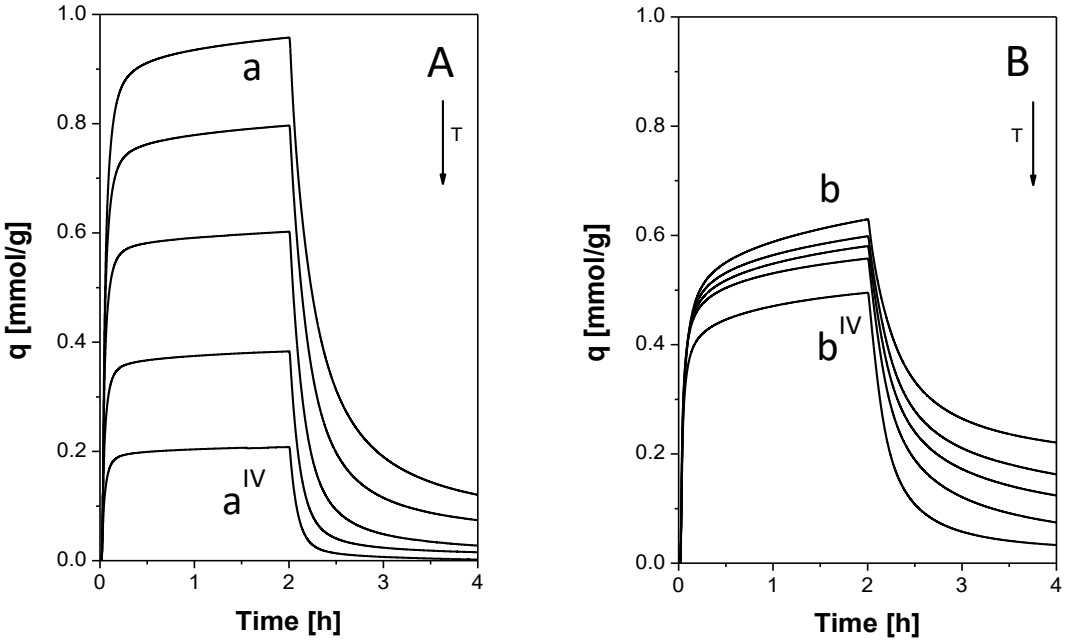

Figure 4.18. CO_2 uptake curves obtained with TGA analysis of P_MCM-41 nano (frame A) and P_MCM-41 micro (frame B) samples at 20, 35, 50, 70 and 90 °C (a to a ^{IV} and b to b ^{IV} curves). [16]

As we can see from CO_2 uptake curves reported in Figure 4.18, the amount of carbon dioxide after 2 h of adsorption decreases with the increase of the temperature. [31] [32] Both materials show this behaviour, but for P_MCM-41 micro sample the decrease is less pronounced, confirming FT-IR observations. In addition, by observing the desorption branch, it can be seen that, for both MCM-41- based hybrid samples, increasing the temperature decreases the residual amount of CO_2 chemisorbed on the amino functionalities. However, the stability of these species is different: for P_MCM-41 nano at 90°C the CO_2 residual fraction is not present, while for P_MCM-41 sample at 90°C a 6.7 % of adsorbed CO_2 is still present.[16] The values of adsorbed

carbon dioxide (reversible and irreversible fractions) obtained with TGA analysis are summarized in Table 4.5.

Sample / Temperature	**CO_2 Adsorption Capacity [mmol/g]**	**reversible fraction [%]**	**irreversible fraction [%]**
P_MCM-41 micro / 20°C	0.63	64.9	35.1
P_MCM-41 micro / 35°C	0.60	72.8	27.2
P_MCM-41 micro / 50°C	0.58	78.6	21.4
P_MCM-41 micro / 70°C	0.55	86.6	13.4
P_MCM-41 micro / 90°C	0.49	93.3	6.7
P_MCM-41 nano / 20°C	0.96	87.4	12.6
P_MCM-41 nano / 35°C	0.79	90.7	9.3
P_MCM-41 nano / 50°C	0.60	95.4	4.6
P_MCM-41 nano / 70°C	0.38	96.0	4.0
P_MCM-41 nano / 90°C	0.21	99.1	0.9

Table 4.5. CO_2 Adsorption Capacity, reversible and irreversible fractions obtained with TGA analysis for the grafted MCM-41 materials. [16]

The adsorption heat values at different temperatures were also calculated for both MCM-41 hybrid samples. Results are reported in Figure 4.19.

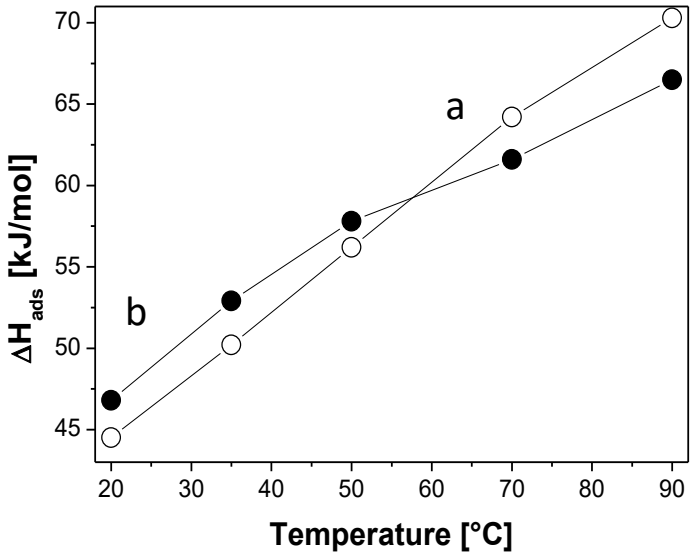

Figure 4.19. Adsorption Heat at different temperatures for P_MCM-41 micro (a) and P_MCM-41 nano (b) samples. [16]

From Figure 4.19 it can be observed that even if the CO_2 uptake decreases when the temperature increases, the overall heat of adsorption increases. In particular increases from 44.5 and 46.8kJ/mol at 20°C to 70.3 and 66.5 kJ/mol at 90 °C for P_MCM-41 micro and P_MCM-41 nano samples respectively. The higher ΔH_{ads} is probably due to the fact that by increasing the temperature the physisorption process no longer plays a significant role. Thus, the measured ΔH_{ads} is related to the pure chemisorption process. [35] [16]

The temperature dependence of the carbon dioxide adsorption process on MCM-41 hybrid samples has been evaluated also by using ZLC analysis. Desorption curves for both grafted samples are reported in Figure 4.20.

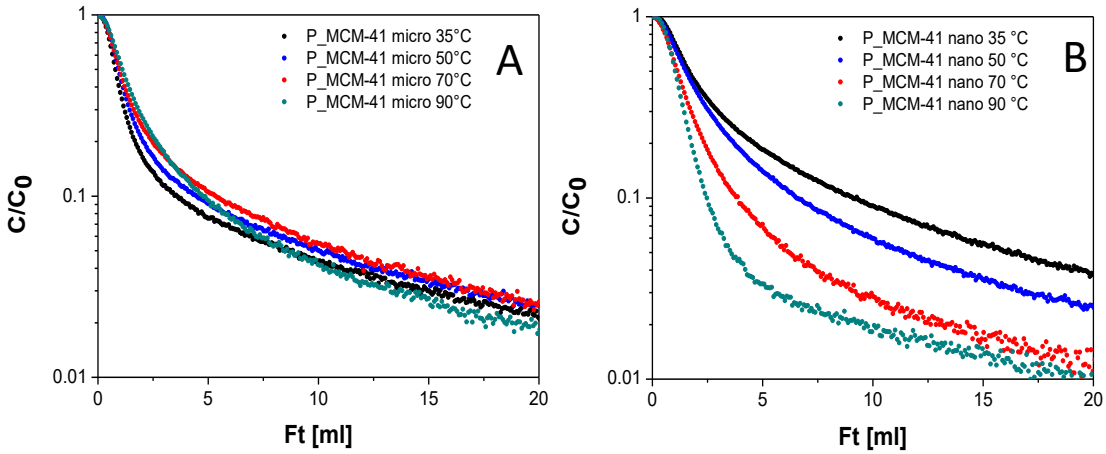

Figure 4.20. ZLC desorption curves for P_MCM-41 micro (A) and P_MCM-41 nano (B) at 35-50-70-90°C. CO_2 partial pressure: 0.1 bar , 2 ml/min flow rate.

The adsorption capacity values obtained from these curves for hybrid microsized and nanosized MCM-41 materials from 35 to 90°C are reported in Figure 4.21.

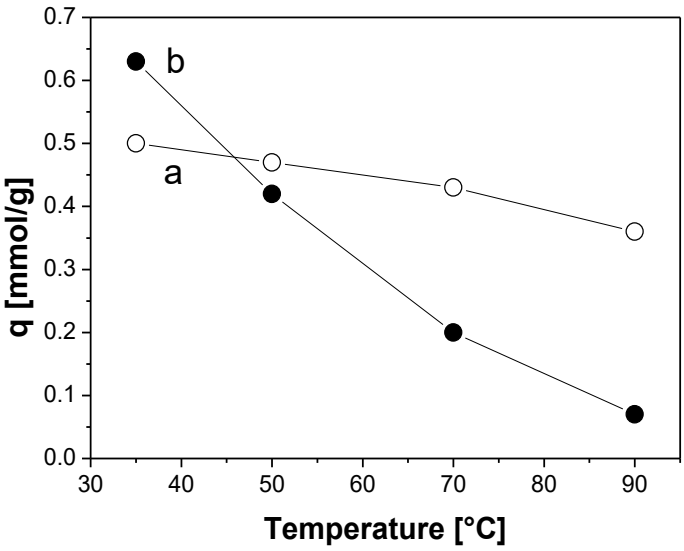

Figure 4.21. CO_2 adsorption capacity values at different temperatures (35-90°C) obtained through ZLC/TPD analysis for P_MCM-41 micro (curve a) and P-MCM-41 nano (curve b).

The temperature dependence of carbon dioxide adsorption on hybrid MCM-41 samples evaluated by using ZLC analysis is in agreement with results obtained from TGA analysis: the CO_2 uptake decrease by increasing the temperature for both

samples, but this effect is less evident for P-MCM-41 micro. This effect is probably due to the fact that the formed carbamic acid and ammonium carbamate in this sample are located in a more protective environment (*i.e.* inside the pores). [16]

Finally, the temperature dependence of the CO_2 uptake was studied using a volumetric adsorption analyzer. Experiments at 35 and 50 °C for both tMCM-41 hybrid materials are reported in Figure 4.22.

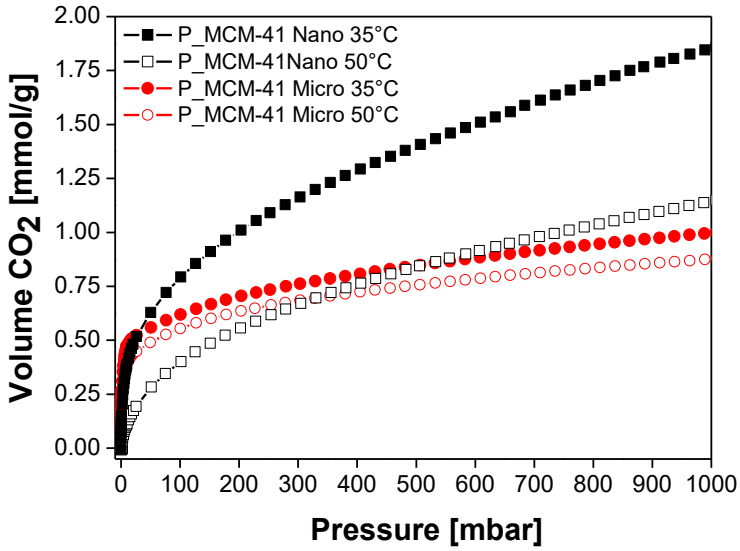

Figure 4.22. CO_2 uptake for P_MCM-41 micro and P_MCM-41 nano samples at 35 and 50 °C obtained by volumetric analysis. [16]

Figure 4.22 shows that the P_MCM-41 nano has a higher CO_2 adsorption capacity at 35°C compared to the P_MCM-41 micro sample: at a relative pressure comparable with thermogravimetric analysis (p=100 mbar) the CO_2 uptake values are 0.79 and 0.62 mmol/g, respectively. This result is in agreement with the CO_2 capture capacity values obtained with TGA (0.79 and 0.58 mmol/g, respectively). However, the isotherms of the two P_MCM-41 materials show different shape. For P_MCM-41 nano sample, the volume of adsorbed carbon dioxide continues to rise by increasing the pressure, being, in the range of pressures considered, far from saturation.

Conversely, the isotherm of P_MCM-41 micro sample presents a quasi-rectangular shape, with a steep step at low pressure, indicating the presence of stronger adsorption sites. This sample is approaching its saturation capacity at atmospheric pressure. [16]

For both MCM-41 samples, the carbon dioxide uptake decreases with the increase of the temperature. However, this behaviour for P_MCM-41 sample is less pronounced than for P_MCM-41 nano sample, fully confirming the observations obtained with TGA and ZLC analysis. [16]

4.7 Conclusions

In this chapter, the CO_2 adsorption properties of amino-modified MCM-41 silicas were studied. FTIR and SS-NMR spectroscopies were used to provide information on physisorption and chemisorption processes occurring contacting carbon dioxide and hybrid materials. It was revealed that higher amount of physical adsorbed CO_2 is present in nanometric sample respect to the micrometric one, probably because of the higher pore accessibility due to the higher pore volume in P-MCM-41 sample. In addition, the amount of CO_2 adsorbed on grafted MCM-41 samples was determined by three different quantitative techniques: gravimetric analysis (TGA), Zero Length Column chromatography (ZLC) and volumetric analysis. The obtained values of CO_2 adsorption capacity, for P_MCM-41 nano and P_MCM-41 micro are respectively: 0.79 and 0.58 mol/kg (TGA), 0.64 and 0.51 mol/kg (ZLC) and 0.79 and 0.62 mol/kg (volumetric analysis). The three different quantitative techniques have led to the determination of comparable carbon dioxide adsorption capacity values.

Furthermore, the reversibility of the reaction was studied. After the desorption process, the microsized sample shows a residual amount of chemisorbed CO_2 higher compared to the nanosized one (respectively 27% and 9% of the total adsorbed CO_2).

Finally, the adsorption process was studied at different temperatures. For both samples, the amount of adsorbed carbon dioxide decreases by increasing the temperature from 20 to 90°C. This is due to the fact that carbamic acid and ammonium carbamate products resulting from the reaction between CO_2 and the amino groups are thermally unstable and release CO_2 upon heating. However, the products of the reaction with carbon dioxide show a greater stability in the micrometric sample, compared to those in the nanosized one, probably because of a greater protection effect caused by the pores.

References

[1] S. Choi, J. H. Drese, C, W. Jones, *ChemSusChem*, **2009**, 2, 796-854.

[2] R. Ben-Mansour, M.A. Habib, O.E. Bamidele, M. Basha, N.A.A. Qasem, A. Peedikakkal, T. Laoui, M. Ali, *Applied Energy*, **2016**, 161, 225–255.

[3] X. Xu, C. Song, J. M. Andresen, B. G. Miller, A. W. Scaroni, *Energy & Fuels*, **2002**, 16, 1463-1469.

[4] X. Xu, C. Song, J. M. Andresen, B. G. Miller, A. W. Scaroni, *Energy & Fuels*, **2002**, 16, 1463-1469.

[5] M.R. Mell, D. Phanon, G. Q. Silveira, P. L. Llewellyn, C.M. Ronconi, *Microporous and Mesoporous Materials*, **2011**, 143, 174–179.

[6] J.C. Vartuli, W.J. Roth and T.F. Degnan, *Dekker Encyclopedia of Nanoscience and Nanotechnology*, **2004**.

[7] J. Chen, N. Xia, T. Zhou, S. Tan, J. Jiang, D. Yuan, *Int. J. Electrochem. Sci*., **2009**, 4, 1063.

[8] X. S. Zhao, G .Q. Lu, G. L. Millar, *Ind. Eng. Chem. Res*., **1996**, 35, 2075.

[9] R. K. Kloetstra, H. van Bekkum, *J. Chem. Res. (Symp.)*, **1995**, 26.

[10] A.Synak, M. Gil, J.A. Organero, F. Sanchez, M. Iglesias and A. Douhal, *J. Phys. Chem. C*, **2009**, 113, 19199.

[11] J. Y. Ying, C. P. Mehnert, M. S. Wong, *Angew Chem Int Ed*, **1999**, 38, 56.

[12] G. D. Stucky, A. Monnier, F. Schüth, Q. Huo, D. Margolese, D. Kumar, M. Krishnamurty, P. Petroff, A. Firouzi, M. Janicke, B. F. Chmelka, *Mol. Cryst. Liq. Cryst.*, **1994**, 240, 187.

[13] A. Firouzi, F. Atef, A.G. Oertli, G.D. Stucky, B.F. Chmelka, *J. Am. Chem. Soc*., **1997**, 119, 3596.

[14] K. Suzuki, K. Ikari and H. Imai, *J. Am. Chem. Soc*., **2004**, 126, 462.

[15] J. S. Beck, J. C. Vartuli, W. J. Roth, M. E. Leonowicz, C. T. Kresge, K. D. Schmitt, C. T-W. Chu, D. H. Olson, E. W. Sheppard, S. B. McCullen, J. B. Higgins and J. L. Schlenkert, *J. Am. Chem. Soc*., **1992**, 114, 10834-10843.

[16] G. Gatti, C. Vittoni, D. Costenaro, G. Paul, E. Mangano, S. Brandani[b], C. Bisio, L. Marchese[a] , *Phys. Chem. Chem. Phys*, **2017**, 19, 29449 – 29460.

[17] C. Vittoni, V. Sacchetto, D. Costenaro, S. Mastroianni, A. Hinsch, L. Marchese, C. Bisio, *Solar Energy*, **2016**, 124, 101–113.

[18] S. Lowell, J.E. Shields, M.A. Thomas, M. Thommes, *Kluwer Academic Publishers*, **2004**.

[19] G. Socrates "Infrared and Raman Characteristic Group Frequencies", *John Wilway & Sons*, LTD, **2001**.

[20] C-Y. Chen, H-Y. Li, M.E. Davis, *Microporous Materials*, **1993**, 2, 1, 17-26.

[21] G. Gatti, D. Costenaro, C. Vittoni, G. Paul, V. Crocellà, E. Mangano, S. Brandani, S. Bordiga, M. Cossi, L. Marchese, C. Bisio, *Phis. Chem. Chem, Phys.*, **2017**, 19, 14114-14128.

[22] C-J Yoo, L-C Lee, C.W. Jones, *Langmuir*, **2015**, 31, 49, 13350-13360.

[23] X. Wang, W. Schwartz, J.C. Clark, X. Ma, S.H. Overbury, X. Xu, C. Song, *J. Phys. Chem. C*, **2009**, 113, 7260-7268.

[24] A. Danon, P.C. Stair, E. Weitz, *J. Phys. Chem. C*, **2011**, 115, 11540–11549.

[25] S. A. Didas, M. A. Sakwa-Novak, G. S. Foo, C. Sievers, C. W. Jones, *J. Phys. Chem. Lett.*, **2014**, 5, 4194−4200.

[26] C. Knofel, C. Martin, V. Hornebecq, P.L. Llewellyn, *J. Phys. Chem. C*, **2009**, 113, 21726-21734.

[27] J.A.A. Gibson, A.V. Gromov, S. Brandani, E.E.B. Campbell, *Microporous and Mesoporous Materials*, **2015**, 208, 129-139.

[28] J.A.A. Gibson, E. Mangano, E. Shiko, A.G. Greenaway, A.V. Gromov, M. Lozinska, D. Friedrich, E.E.B Campbell, P.A. Wright, S. Brandani, *Ind. Eng. Chem. Res.*, **2016**, 55, 3840-3851.

[29] B. Dutcher, M. Fan, A. G. Russell, *ACS Appl. Mater. Interfaces*, **2015**, 7, 2137−2148.

[30] O. Leal, C. Bolivar, C. Ovalles, J. J. Garcia, Y. Espidel, *lnorganica Chimica Acta*, **1995**, 240, 183-189.

[31] Z. Bacsik, R. Atluri, A. E. Garcia-Bennett and N. Hedin, *Langmuir*, **2010,** 26, 12, 10013–10024.

[32] Y. Belmabkhout, A. Sayari, *Adsorption*, **2009**, 15, 318–328.

[33] G. P. Knowles, S.W. Delaney, A.L. Chaffee, *Ind. Eng. Chem. Res*., **2006**, 45, 2626-2633.

Chapter 5

Unravelling the Effect of the Adsorbent Porosity on the CO_2 Adsorption Performances

Introduction

As reported in previous chapters, ordered mesoporous siliceous materials have been widely investigated as solid adsorbent for the carbon dioxide capture. However, most of these ordered porous solids, such as MCM-41 and SBA-15, are quite expensive.[1] For example, it was estimated that in amino-based MCM-41 or SBA-15 materials the cost of the mesoporous support accounts for more than 90% over the total expense of the adsorbent (> $700/kg). [2] The high cost is mainly due to the use of very expensive templates (*i.e.* Hexadecyltrimethylammonium chloride, CTAC), necessary for the formation of the ordered structure of pores typical of these solids. Hence, using a less expensive support, the preparation cost of the adsorbent can be considerably reduced. Furthermore, ordered mesoporous silica (specially MCM-41 type) present poor hydrothermal stability. [3] This feature can lead to the sorbent degradation after several adsorption/desorption cycles, limiting the practical application of these sorbents for the CO_2 capture from flue gas. [1]

With the aim of overcome these problems, in literature other types of silica have been studied as support for carbon dioxide capture. For example silica gel, a porous material produced on a large scale with a price less than $40/kg, has been investigated.[4] For example, Zhang et al. studied a sorbent consisting of

polyethylenimine-impregnated silica gel. In their work, they found that the silica-gel-based material is a promising adsorbent for carbon dioxide capture due to its high adsorption capacity (q: 3.13 mmol/g), low-preparation cost and easy commercial availability of the silica gel. [1]

So far, however, among the various low cost siliceous materials, monodisperse silica particles have not yet been considered in literature as solid support for CO_2 adsorption. However, such materials may constitute very interesting adsorbents in this field, especially for economic factors: the synthesis of monodisperse silica spheres in fact, for example with Stöber method, does not involve the use of templates.

Moreover, a comparison of the carbon dioxide adsorption properties of silica particles with those of mesoporous ordered silica allows to investigate the effect of the porosity on the CO_2 capture performances. This aspect, fundamental for the comprehension of the carbon dioxide adsorption process, has not been studied to date in literature.

For these reasons, in this chapter the adsorption properties of monodisperse silica particles obtained by Stöber method will be studied. On the basis of the results obtained in Chapter 3, the Stöber support has been modified via grafting of 3-[2-(2-aminoethyl)aminoethyl]aminopropyltrimethoxysilane (PAPTS). Moreover, in order to investigate the effect of the adsorbent porosity on the carbon dioxide adsorption performances, organo-modified Stöber-based adsorbers have been compared with MCM-41-based materials. MCM-41 silica was chosen among other as it is characterized by micrometric dimensions, comparable to the Stöber silica particle size. Unlike the Stöber silica, however, presents an ordered structure of pores. A schematic representation of these two materials is given in Figure 5.1.

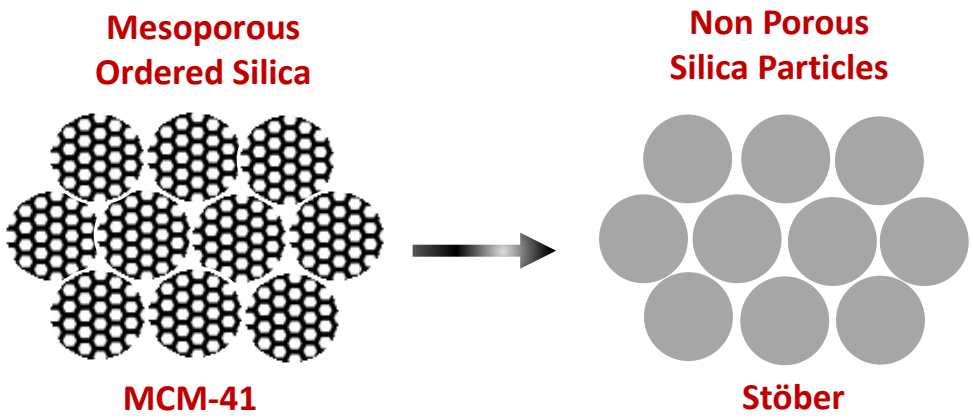

Figure 5.1. Schematic representation of the comparison between a mesoporous ordered silica (MCM-41 type) and non porous silica particles obtained by using the Stöber method.

In the following Paragraphs will be described:

- the synthesis method of Stöber silica and derived hybrid material (Paragraphs 5.1 and 5.2);
- the physico-chemical properties of Stöber silica and the related organo-modified material (Paragraph 5.3);
- a multidisciplinary study of the CO_2 adsorption process on the Stöber –based adsorber, compared to that of MCM-41-based sample (Paragraphs 5.4).

5.1 Stöber Silica

In 1956 Kolbe et al. for the first time obtained spherical silica particles from the precipitation of tetraethylorthosilicate (TEOS) in an alcoholic solution with the presence of ammonia.[5] Following this study, in 1968 Stöber et al. proposed an effective method for the synthesis of monodispersed silica particles with diameters ranging from nanometers to 1-2 microns. According to this method, the modification of particle size can be obtained by varying several factors, such as temperature, reagent concentration and the type of solvent. [6]

Silica particles obtained by Stöber method present the following characteristics: i) remain stable in solution due to electrostatic repulsion by the negatively charged silica particles, ii) are perfectly uniform in size and shape, iii) their size can be easily controlled and the process provides high yields at low costs.

For these peculiarities, Stöber silica are widely used in different application fields. First of all, it is commonly used for chromatographic applications; in fact, thanks to the reduced particle size, the separation of the eluate becomes extremely fast. In addition, Stöber silica is used as pigment and dye carrier material, for example for diagnostic applications; in fact, many dyes contain acid sulfonic groups, which can be easily anchored to the surface by a post-synthesis grafting procedure or incorporated during the particle growth by one-pot method. Many research groups also used Stöber silica as a model to study the rheological behaviour of colloidal dispersions. Finally, this type of silica have been used to test porosimetry analysis techniques, such as nitrogen adsorption or mercury intrusion porosimetries, since they are characterized by an extremely ordered structure resulting from the uniformity of the particle size. [7]

Stöber silica is produced by using a precursor (usually tetraethylorthosilicate), an alcoholic solvent as ethyl alcohol, water and ammonia, which acts as alkali catalyst to initiate hydrolysis and condensation reactions. [8] The description of these reactions is reported more in detail in Paragraph 3.2.1.

As mentioned before, the particle size can be tailored by changing several factors. In particular, the particle dimension become wider at lower reaction temperatures. Moreover, the particle size may be decreased by using tetramethylorthosilicate instead of tetraethylorthosilicate, and methanol instead of ethanol. TEOS concentration also affects the particle size: high TEOS concentrations allows to prepare larger particles; in any case, however, the concentration of tetraethylorthosilicate should not exceed 0.2 mol/dm^3, as higher quantities form non-spherical particles. [6]

Several nucleation and growth mechanisms for the formation of Stöber silica particles have been proposed in literature. Currently, the most common mechanisms are the Monomer Addition Growth model and the Aggregation Growth model. The first mechanism have been proposed by Matsoukas and Gulari. [9] According to their theory, initially there is a first-order slow activation step (hydrolysis), followed by a three times faster step (condensation). The nucleation occurs when the over-saturation limit is exceeded, whereas the growth occurs later by condensation of the hydrolyzed monomer on the surface of the pre-existing nuclei.

According to the second model, proposed by Boogush and Zukoski, nanometric silica particles (nuclei) are continuously formed during the hydrolysis and the condensation of TEOS (the nucleation occurs continuously during the reaction). However, nuclei are unstable and therefore aggregate to form larger units. When they reach a critical diameter, they become stable. Further growth is possible due to the addition of primary nuclei to the agglomerates surface. [10]

A compromise between these two models was proposed by van Blaaderen et al. According to their theory, the particle growth involves the addition of monomer, and the rate of particles growth is controlled by the rate in which the hydrolysis of the alkoxide occurs; on the other hand, the nucleation of the particles proceeds through the aggregation of the subparticles. [11]

5.2 Materials Preparation

5.2.1 Synthesis Procedure of Stöber Silica

Stöber silica has been synthesized by hydrolysis and condensation of tetraethylorthosilicate (TEOS) catalyzed by ammonia. In a typical synthesis, a solution of 3.0 mL of NH_4OH, 7.28 mL of water and 50 mL of ethanol have been prepared. Subsequently, 5.6 mL of TEOS were added, and the solution was stirred for 2 hours at room temperature. The ethanol solution was then evaporated at 60 °C for 5 hours and finally the precipitate was dried at 80 °C for 2 hours. [12]

5.2.2 Post Synthesis Functionalization of Stober Silica

Stöber silica samples were functionalized with N-[3-(trimethoxysilyl)propyl]-diethylenetriamine (PAPTS) in order to introduce basic groups on the silica surface by using a post-synthesis grafting method. The method followed was the same used for the functionalization of SBA-15 silica (Paragraph 2.3.2).

The obtained hybrid sample will be hereafter named P_ Stöber**.**

5.3 Physico-chemical Characterization

Silica particles obtained by Stöber method and the relative hybrid materials were characterized by using different experimental techniques to determine the physico-chemical properties.

The morphology of MCM-41 silica samples was studied by using scanning electron microscopy (SEM). The obtained SEM images and the particle size distribution of Stöber silica sample are reported in Figure 5.2.

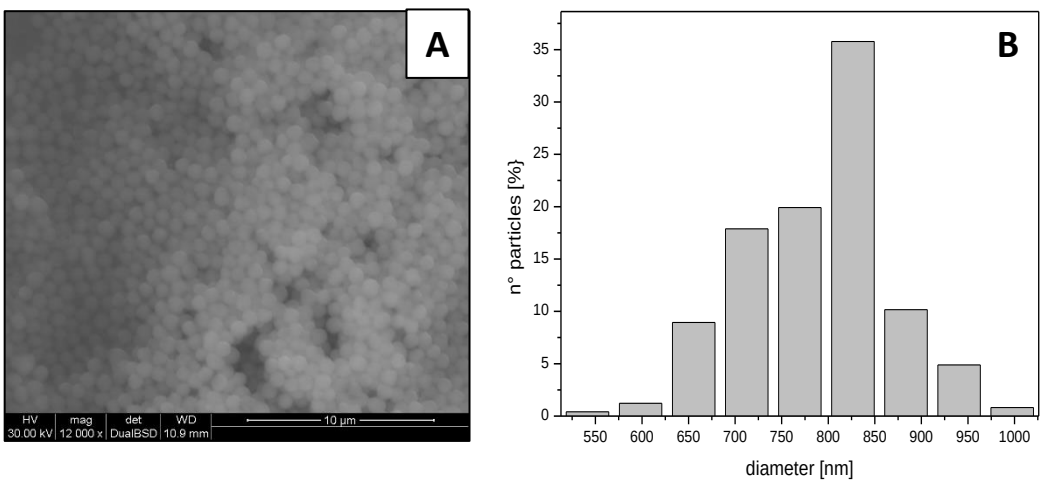

Figure 5.2. SEM micrograph (Frame A) and particle size distribution (Frame B) of Stöber silica sample.

Stöber silica (Figure 5.2, Frame A) is made of spherical particles with micrometric size with a mean diameter of *ca.* 800 nm. The histogram reported in Figure 5.2 B, obtained by analyzing around 250 particles, shows that the particle diameter is in the range between 650 and 900 nm. The polydispersity index (PI), expressed by the relative standard deviation of the diameter, is 0.22 (if the particles are perfectly monodisperse, P.I = 0, while an increase in polydispersity yields higher PI values). [13][14]

The textural properties of Stöber silica sample and the relative functionalized material, N_2 physisorption analysis at 77K was carried out. N_2 adsorption-desorption isotherms and pore size distribution of Stöber and P_Stöber samples are reported in Figure 5.3.

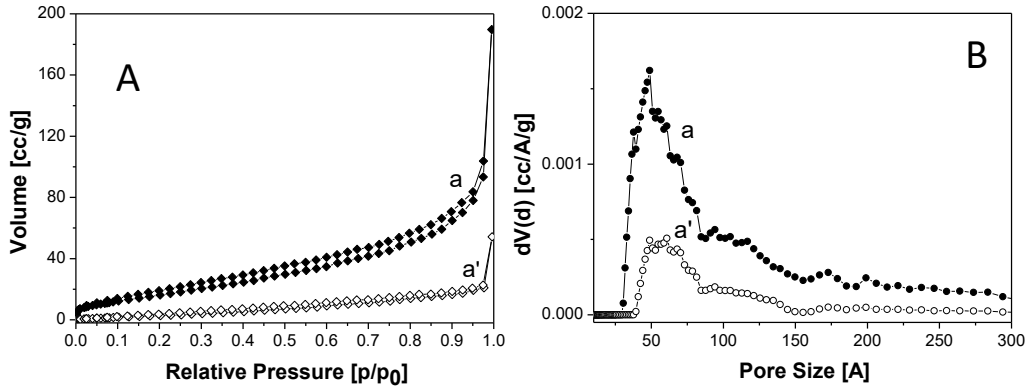

Figure 5.3. Nitrogen adsorption-desorption isotherms at 77 K and relative pressures (P/P_0) from $1*10^{-7}$ to 1 (Frame A) and pore size distribution determined by NLDFT methods (Section B) of Stöber (a) and P_ Stöber (a') samples.

The adsorption isotherms of the Stöber silica sample (Figure 5.3 A, curve a) is of type II, typical of non-porous solids, and presents a thin hysteresis loop of H1 type in a wide range between 0.2 and 0.9 P/P_0. This type of hysteresis loop, due to aggregation porosity, is often obtained with materials consisting of approximately uniform spheres agglomerates.[15] After the functionalization procedure, the shape of

the isotherm is modified (Figure 5.3, curve a'). In particular, the volume of adsorbed N_2 in the grafted sample is decreased.

The BET algorithm was used to estimate the specific surface area (SSA) of the materials that was determined to be 60 and 15 m^2/g, respectively for Stöber and P_Stöber samples. The reduction of specific surface area values of P_Stöber sample respect to the bare one (about -75%) can be due to the presence of the organic chains on the surface that are reducing the aggregation porosity.

The pore size distribution was determined by using the NLDFT method and the desorption branch of the isotherm. From this graph (Figure 5.3 B) it is possible to note that the Stöber silica sample is characterized by aggregation pores with a size between 25 and 200 Ǻ, with a maximum at around 50 Å. After the grafting, the porous volume decrease due to the presence of PAPTS chains in the aggregation porosity. Instead, smaller pores (between 25 and 40 Å) are completely filled with the organic chain.

The nitrogen content in P_ Stöber has been determined by elemental analysis, and was found to be 2.25 mmol/g.

The presence of the PAPTS on the surface of Stöber silica particles was monitored by infrared spectroscopy. Spectra of the samples before and after the grafting are given in Figure 5.4.

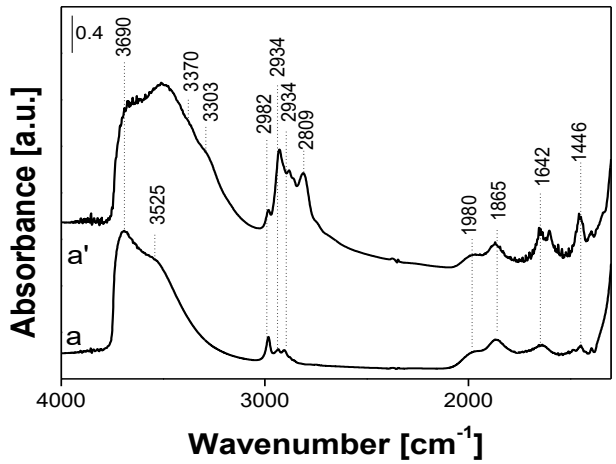

Figure 5.4. FT-IR spectrum of Stöber (curve a) and P_ Stöber (curve a') samples in the 4000–1250 cm^{-1} region. Spectra were recorded after outgassing of the samples for 1 h.

The FT-IR spectrum of the Stöber silica sample (Fig. 5.4, curve a) is characterized by the presence of a broad band with maxima at 3690 and 3525 cm^{-1}, due to the stretching modes of different family of OH groups interacting with each other by H bonding. [16] Moreover, bands in the 3000–2800 cm^{-1} range are due to the stretching modes of CH_2 species deriving from the presence of incompletely reacted TEOS.[17] In the low frequency region, the spectrum shows bands at 1980 and 1865 cm^{-1}, due to the overtones and combination modes of the silica framework.

After the functionalization (Figure 5.4, curve a'), bands due to surface silanols are shifted at high wavenumbers, thus indicating an interaction between OH groups and the amino groups of PAPTS chains. Moreover, the stretching and bending vibrations related to PAPTS chains are also visible (more detailed information are given in Paragraph 3.3.2) thus confirming the presence of the organic chains.

5.4 Study of the Interaction between Stöber Hybrid Samples and CO_2

The interactions between CO_2 and the organo-modified Stöber silica sample have been evaluated by using infrared spectroscopy of adsorbed carbon dioxide. Extensive experimental details are reported in Paragraph 3.5. FT-IR spectra after the admission of 60 mbar of CO_2 at 35°C on the organo-modified Stöber silica samples are reported in Figure 5.5.

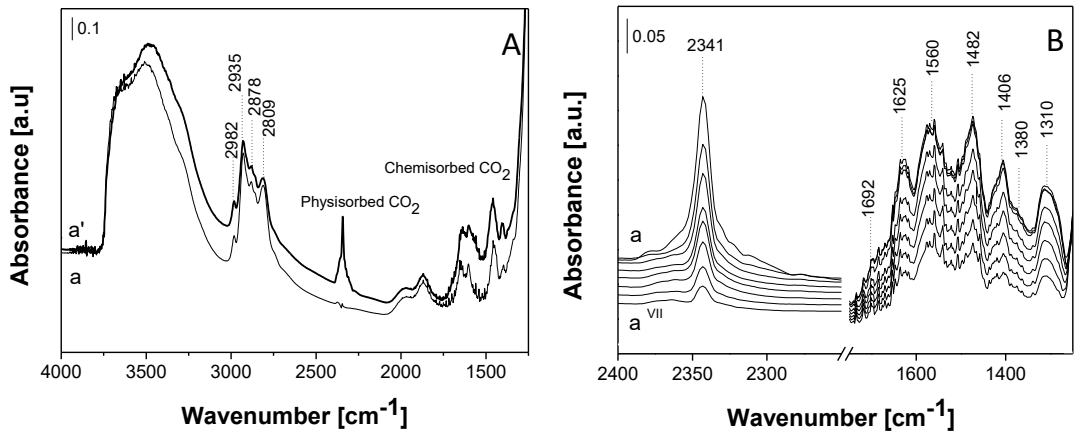

Figure 5.5. Frame A: FTIR spectra in the 4000-1250 cm^{-1} region of P_Stöber before (curve a) and after (curve a') the admission of 60 mbar of CO_2 at 35°C. Spectra are reported after subtraction of the spectrum of gaseous CO_2. Frame B: FTIR spectra, in the 2400–1250 cm-^{1} region, of CO_2 adsorbed (Pmax = 60 mbar) at 35°C on P_Stöber (a-a^{VII}). The arrows indicate a decrease of CO_2 pressure. Spectra are reported after subtraction of the spectrum recorded before CO_2 interaction and after the subtraction of the spectrum of gaseous CO_2.

After the admission of carbon dioxide the infrared spectrum of P_ Stöber sample (Figure 5.5 A, curve a') is modified. In particular, the large band between 3500 and 2000 cm^{-1} is shifted at lower frequencies, owing to interaction of the silica surface (silanol groups and organic chain grafted on the surface) with carbon dioxide. Moreover, bands due to both physical and chemical adsorbed CO_2 are visible. In particular, at 2341 cm^{-1} a band due to the stretching mode of physisorbed CO_2 is

visible, whereas bands due to products of the chemical reaction between NH_2 and carbon dioxide are located in the region between 1750 and 1250 cm^{-1}. In order to better appreciate these bands, spectra obtained after the subtraction of the spectrum recorded before the CO_2 admission are reported in Figure 5.5 B. In the low frequency region (in which absorptions of chemisorbed species fall), bands due to the formation of both carbamate and carbamic acid are observable. In particular, bands due to ammonium carbamate species are visible at 1560, 1482 and 1406 cm^{-1}, while bands due to carbamic acid are located at 1692 and 1380 cm^{-1} (a detailed description of the assignation of these bands is reported in Paragraph 3.5). [18,19,20,21] Furthermore, the band at 1625 cm^{-1} is ascribed to the bending of NH_3^+ species deriving from the interaction of amino groups with carbamic acid [19], while the band at 1310 cm^{-1} is attribute to skeletal vibrations of $NCOO^-$species [22]. By decreasing progressively the CO_2 pressure (Fig. 5.5B, curves a^I- a^{VII}) bands related to both physisorbed and chemisorbed CO_2 decrease in intensity. In particular, bands due to physical adsorbed CO_2 decrease faster, as the involved bonds are weaker. In order to evaluate the differences between this non porous material with a porous one, in Figure 5.6 is reported a comparison between P_ Stöber and P-MCM-41 spectra after the admission of carbon dioxide.

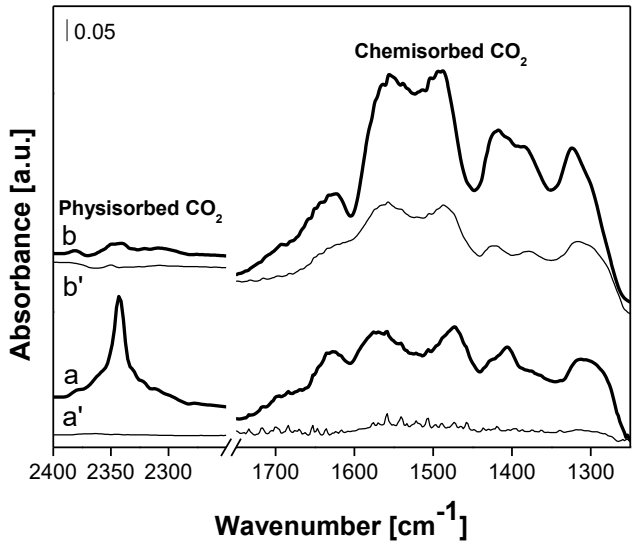

Figure 5.6. FTIR spectra of 60 mbar of carbon dioxide adsorbed at 35°C on P_Stöber (curve a) and P_MCM-41 (b) and FT-IR spectra recorded after degassing CO_2 until vacuum (curve a' and b', respectively for P_Stöber and P_MCM-41). Spectra are reported after subtraction of the spectrum recorded before CO_2 interaction, used as a background.

In Figure 5.6 it can be observed that physisorbed CO_2 (band at 2341 cm^{-1}) is much more abundant in P_Stöber sample compared to P_MCM-41. This result was unexpected, because the Stöber silica sample does not exhibit structural porosity. Such huge adsorption, however, can occur in the porosity formed by the aggregation of the monodisperse particles.

Moreover, concerning the chemisorption region, the related bands (curves a,b) are more intense for P_MCM-41 with respect to P_Stöber sample, thus indicating that a greater amount of ammonium carbamates and carbamate acids species are present in the mesoporous ordered sample. This effect is probably due to the highest amount of PAPTS groups present in the mesoporous sample. In fact, the Nitrogen content of the samples determined by elemental analysis are 2.25 and 3.67 mmol/g for P_Stöber and P_MCM-41 samples, respectively. This difference is due to the different number of silanol groups present in the two samples: $3.35 * 10^{21}$ and $6.09 * 10^{20}$ SiOH/g,

respectively for P_Stöber and P_MCM-41 samples. In any case, it seems from the FT-IR observations that all basic groups are accessible to carbon dioxide.

At the end of the desorption process (curves a', b'), in P_ MCM-41 the related bands are still observable, whereas in P_ Stöber are not visible. This indicates a difference of the stability of ammonium carbamate and carbamic acid species due to the location of NH_2 groups. In P_MCM-41 sample, the amino groups are located into the pores. Stöber sample instead is non porous, and therefore NH_2 groups are present on the external surface. For this reason, the carbamate species formed on this sample are less protected by the confinement effects compared to P_MCM-41 sample.

The comparison of CO_2 adsorption process on porous and non porous materials was further studied by using ^{13}C MAS NMR spectroscopy (Figure 5.7).

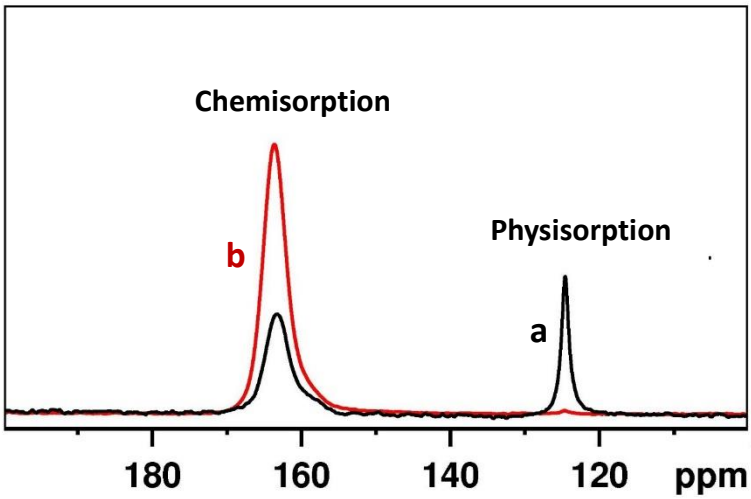

Figure 5.7. ^{13}C MAS NMR spectra of $^{13}CO_2$ adsorbed on P_Stöber (a) and P_MCM-41 (b) recoded using a MAS rate of 10 kHz.

^{13}C MAS NMR spectrum of P_ Stöber sample (Figure 5.7, curve a) show a peak due to chemisorbed carbamate species centred at 164 ppm and a peak related to the physisorbed $^{13}CO_2$ located at 125 ppm. Quantitative data derived from the ^{13}C MAS NMR spectra of P_ Stöber sample show that the amount of $^{13}CO_2$ physically

adsorbed represent about the 30% of the total, while the remaining part is due to the contribution of chemisorbed species. These quantitative data confirm that the physisorption contribute in P_ Stöber sample is higher compared to that in P_MCM-41 (less than 1% of total adsorption).

In order to determine whether the huge physisorption seen in P_Stöber sample is observable even in the case of bare Stöber sample (*i.e.* not containing the amino groups), in Figure 5.8 is reported comparison of FT-IR spectra of both samples.

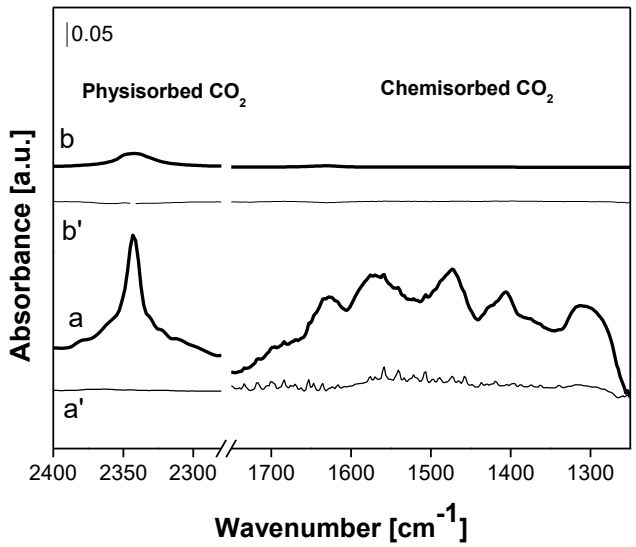

Figure 5.8. FTIR spectra of 60 mbar of carbon dioxide adsorbed at 35°C on P_Stöber (curve a) and Stöber sample (curve b) and FT-IR spectra recorded after the degassing (curve a' and b', respectively for P_Stöber and Stöber sample). Spectra are reported after subtraction of the spectrum recorded before CO_2 interaction.

As expected, for bare Stöber sample (Figure 5.8, curve b) no bands attribute to chemisorbed CO_2 are observable. Only a small band at 2341 cm^{-1}, due to the physisorbed carbon dioxide, is visible. This band is much less abundant compared to P_Stöber sample (curve a), indicating that the PAPTS chains grafted on the surface of the particles forms a new type of aggregation porosity (Figure 5.3, frame B), in

which the physisorption occurs. As for chemisorption, as expected, no bands are formed; this is due to the absence of amino groups in this sample.

To confirm these observations, ^{13}C MAS NMR spectroscopy of adsorbed carbon dioxide on the bare Stöber sample has been performed. Results are reported in Figure 5.9.

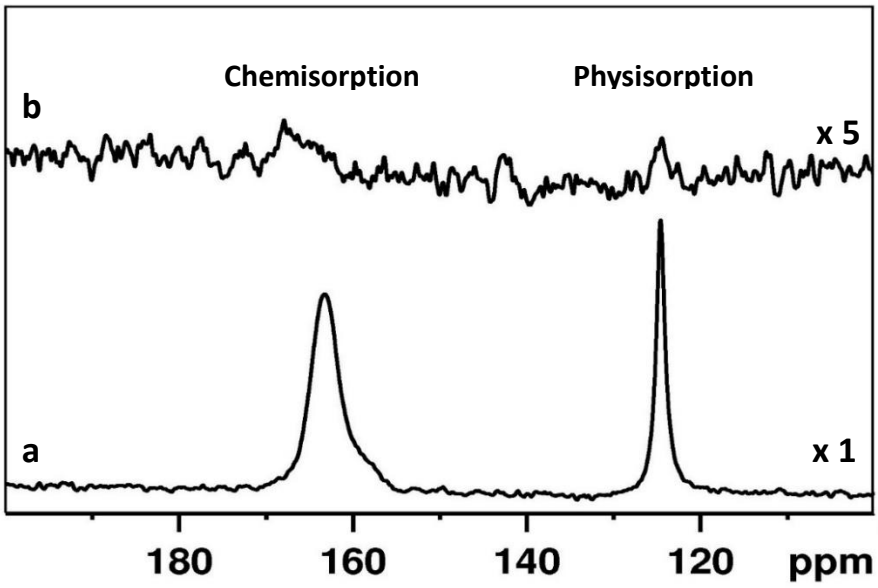

Figure 5.9. ^{13}C MAS NMR spectra of $^{13}CO_2$ adsorbed on P_Stöber (a) and Stöber sample (b). The spectrum of Stöber sample (curve b) has been amplified (x5) for a better signal observation.

In ^{13}C MAS NMR spectrum of bare Stöber sample (Figure 5.9, curve b) the signal of physisorbed $^{13}CO_2$, located at 125 ppm, is not easily distinguishable from the background noise, indicating that only a small amount of $^{13}CO_2$ is physically adsorbed on the bare sample. Therefore, is the PAPTS chain grafted on the silica surface that is responsible of a new pore distribution, where the physisorption occurs.

5.5 Evaluation of CO_2 Capture Capacity of Hybrid Stöber Samples

The carbon dioxide adsorption capacity has been evaluated by CO_2 adsorption-desorption cycles followed by gravimetric analysis. Experimental details are reported in paragraph 4.5. CO_2 uptake curve at 35°C of P_Stöber sample, compared with that of MCM-41, is reported in Figure 5.10.

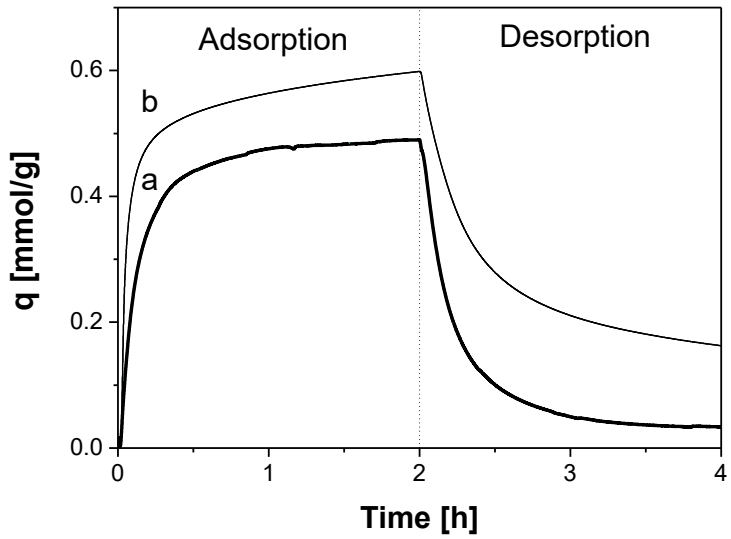

Figure 5.10 CO_2 uptake curves obtained from TGA analysis of P_Stöber (curve a) and P_MCM-41 (curve b) silica samples. Measurements were recorded at 35°C, 0.1 bar CO_2-0.9 bar He in adsorption and 1 bar He in desorption.

The CO_2 adsorption capacity (q) of P_Stöber sample derived from gravimetric adsorption curve (Figure 5.10, curve b) is 0.49 mmol/g. This value is slightly lower respect to the CO_2 adsorption capacity of P_MCM-41 (0.58 mmol/g). Moreover, the shape of the adsorption curves of the two samples are different. In detail, the diverse adsorption/desorption rate of P_Stöber compared to P_MCM-41 sample suggest that a different predominant adsorption process occurs. P_MCM-41 shows slower adsorption rate compared to P_ Stöber sample, suggesting a higher contribute of chemisorption fraction: the chemical adsorption, in fact, is characterized by a slower

kinetic compared to that relative to the physisorption. Furthermore, at the end of the desorption curve, different amount of CO_2 (representing the irreversible fraction still chemisorbed on the samples) is present. In particular, for P_MCM-41 a higher percentage of CO_2 is retained (about 27% of the total) compared to P_ Stöber (ca. 6% of the total), thus indicating that in the mesoporous sample the chemisorption is the predominant process, while in P_ Stöber sample the physisorption has the main role. These results agree with FT-IR and SS-NMR Spectroscopy observations.

Adsorption heat values (ΔH_{Ads}) of P_ Stöber and P_MCM-41 samples have been calculated from the heat flow measured by the DSC. Details on calculations are given in Paragraph 4.4. The ΔH_{Ads} values obtained for P_ Stöber and P_MCM-41 samples are 52.9 and 43.2 kJ/mol, respectively. The lower adsorption heat obtained for P_ Stöber sample compared to P_MCM-41 confirms that in the predominant mechanism occurring in the non porous material is physisorption.

The quantitative determination of adsorbed carbon dioxide has been also performed by using the ZLC analysis. Desorption curves obtained for P_ Stöber and P_MCM-41 at 35°C are reported in Figure 5.11.

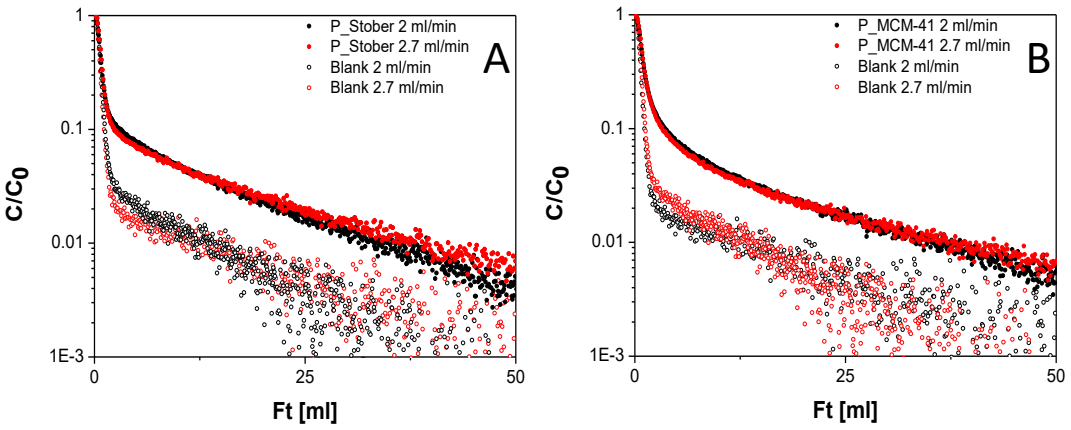

Figure 5.11. ZLC desorption curves for P_ Stöber (section A) and P_MCM-41 sample (section B) and blank curves at 2 and 2.7 ml/min flow rates. CO_2 partial pressure: 0.1 bar, T: 35°C.

The carbon dioxide adsorption capacity values calculated from ZLC desorption curves (Paragraph 3.6) are: 0.40 and 0.51 and mmol/g for P_ Stöber and P_MCM-41, respectively. These data reflect the behaviour observed by TGA analysis. These adsorption capacity values are only slightly lower than those obtained by gravimetric analysis (0.49 and 0.58 mmol/g for P_ Stöber and P_MCM-41, respectively) due to a degradation occurred in the samples (ZLC analysis in fact was the last experiment conducted).

Anyway, even if the ordered mesoporous-based material is more efficient compared to the non-porous one, it must be considered that the difference of the adsorption capacity is not very large, and that the Stöber-based material is much cheaper. For these reasons, it deserve interest for potential applications in the carbon capture field.

5.6 Conclusions

In this chapter, the CO_2 adsorption properties of amino-functionalized Stöber silica sample have been evaluated by using different experimental techniques. In particular, FTIR and SS-NMR spectroscopies were used to provide information on physical and chemical adsorption processes occurring by contacting CO_2 and the non porous silica-based hybrid material. From these analyzes it was revealed that a high amount of physisorbed CO_2 is present in the Stöber-functionalized sample, whereas a close to zero amount of physical adsorbed carbon dioxide is observable for the bare Stöber sample. From this comparison it was emerged that is the aggregation porosity modified by the presence of PAPTS chains the responsible of the huge amount of physical adsorption.

Moreover, the effect of the support porosity on the carbon dioxide adsorption performances has been evaluated by comparing the organo-modified Stöber with a MCM-41-based material. From this comparison, obtained by using FTIR and SS-NMR analyzes, it was revealed that higher amount of physisorbed CO_2 is present in the Stöber-based sample compared to the MCM-41- based one, probably because of

the higher pore accessibility. With regard to chemisorption, conversely, the ordered mesoporous sample present the highest amount of CO_2 adsorbed. This effect is probably due to the highest amount of PAPTS groups present in this material (the Nitrogen content of the samples is 2.25 and 3.67 mmol/g for P_Stöber and P_MCM-41 samples, respectively).

In addition, in order to verify which material is able to absorb a higher amount of carbon dioxide, a quantitative analysis has been performed by using TGA and ZLC analyzes. The obtained values of CO_2 adsorption capacity are 0.49 and 0.58 mol/kg (TGA) and 0.40 and 0.51 mol/kg (ZLC), respectively for P_ Stöber and P_MCM-41 samples. Therefore, taking into account of the adsorption process as a whole (*i.e.* with respect of both phyisorption and chemisorption), the ordered mesoporous-based material is more efficient. However, the non-porous material is much cheaper and has an efficiency not too low compared with the MCM-41-based material: for this reason, non-porous materials such P_ Stöber deserve to be considered among the various solid adsorbents for the carbon dioxide capture.

References

[1] Z. Zhang, X. Ma, D. Wang, and C. Song, *AIChE Journal*, **2012**, 58, 8, 2495-2502.

[2] M.G. Plaza, C. Pevida, A. Arenillas, F. Rubiera, J.J. Pis, *Fuel*, **2007**, 86, 2204–2212.

[3] F. Carniato, C. Bisio, G. Paul, G. Gatti, L. Bertinetti, S. Coluccia and L. Marchese, *J. Mater. Chem.*, **2010**, 20, 5504–5509.

[4] O. Leal, C. Bolìvar, Cèsar Ovalles, J.J. Garcia, Y. Espidel, *lnorganica Chimica Acta*, **1995**, 240, 183-189.

[5] G. Kolbe, "The Complex Chemical Behavior of Silica", Dissertation, Jena, Germany, **1956**.

[6] J. H. Zhang, P. Zhan, Z. L. Wang, W. Y. Zhang, and N. B. Ming, *J. Mater. Res.*, **2003**, 18, 3, 649-653.

[7] H. Giesche, "Medical Applications of Colloids", *Springer*, **2008**.

[8] W. Stober, A. Fink, E. Bohn, *Journal of Colloid and Interf. Sci.*, **1968**, 26, 62-69.

[9] T. Matsoukas, E. Gulari, *J. Colloid Interf. Sci*., **1988**, 124, 1, 252-261.

[10] G. H. Bogush, C. F. Zukoski, *J. Colloid Interf. Sci.*, **1991**, 142, 1, 19-34.

[11] A.Van Blaaderen, J.Van Geest, A.Vrij, *J. Colloid Interf. Sci.*, **1992**, 154, 2, 481-501.

[12] D. L. Green, J. S. Lin, Y-H. Lam, M. Z. -C. Hu, D. W. Schaefer, M. T. Harris, *J. Colloid Interf. Sci.*, **2003**, 266, 346–358.

[13] N. Plumerè, A. Ruff, B. Speiser, V. Feldmann, H. A. Mayer, *J. Colloid Interf. Sci.*, **2012**, 368, 208–219.

[14] C. Vittoni, V. Sacchetto, D. Costenaro, S. Mastroianni, A. Hinsch, L. Marchese, C. Bisio, *Solar Energy*, **2016**, 124, 101–113.

[15] Z. Wu, H. Xiang, T. Kim, M-S. Chun, K. Lee, *J. Colloid Interf. Sci.*, **2006**, 304, 119-124.

[16] A. Beganskiene, V. Sirutkaitis, M. Kurtinaitiene, R. Juskenas, A.Kareiva, *Mater. Sci.*, **2004**, 10, 287–290.

[17] M. Pàlmai, L. N. Nagy, J. Mihàly, Z. Varga, G. Tàrkànyi, R. Mizsei, I. C. Szigyàrtò, T. Kiss, T. Kremmer, *J. Colloid Interf. Sci*., **2013**, 390, 34–40.

[18] G. Gatti, D. Costenaro, C. Vittoni, G. Paul, V. Crocellà, E. Mangano, S. Brandani, S. Bordiga, M. Cossi, L. Marchese, C. Bisio, *Phis. Chem. Chem, Phys.*, **2017**, 19, 14114-14128.

[19] X. Wang, W. Schwartz, J. C. Clark, X. Ma, S. H. Overbury, X. Xu, C. Song, *J. Phys. Chem. C*, **2009**, 113, 7260-7268.

[20] A. Danon, P. C. Stair, E. Weitz, *J. Phys. Chem. C*, **2011**, 115,11540-11549.

[21] S. A. Didas, M. A. Sakwa-Novak, G. S. Foo, C. Sievers, C. W. Jones, *J. Phys. Chem. Lett*., 2014, 5, 4194-4200.

[22] C. Knofel, C. Martin, V. Hornebecq, P. L. Llewellyn, *J. Phys. Chem. C*, **2009**, 113, 21726-21734.

Chapter 6

An Example of CO_2 Utilization: the Hydrogenation to Formic Acid

Introduction

Following the capture and storage procedures, the carbon dioxide can be valorized by its transformation in highly useful product. In the literature, many studies of CO_2 conversion in new chemical commodities, such as fuels (through, for example, Fischer–Tropsch chemistry) or polymers (through successive copolymerization and chain growth) are present. [1] Among these, the hydrogenation reaction to formic acid is particularly interesting. In fact, formic acid is widely used in many fields, such as textile, leather and rubber industries. Furthermore, it can be used as feedstock for the production of chemicals in food industries (*i.e.* sweetener, preservatives). Finally, the hydrogenation of CO_2 to formic acid, followed by its decomposition to give back CO_2 and H_2, can be an interesting hydrogen storage technique. The development of improved technologies for H_2 generation and storage in a safe and reversible manner is a prerequisite for the utilization of hydrogen as fuel. [2] Actually the techniques for H_2 accumulation are based on tank systems for gaseous-pressurized and liquid hydrogen. However, both systems have some drawbacks such as the low hydrogen storage density, the requirement for high pressure or high-energy liquefaction apparatus, together with safety problems. Furthermore, also storage systems based on hydrogen chemisorption (*i.e.* metal hydrides and other inorganic H_2-rich compounds) or physisorption of (*i.e.* carbon nanotubes, metal–organic frameworks, etc…) have been investigated in literature. [3] Unfortunately, the chemisorption-

based techniques need high temperature for hydrogen release and are not reversible, while in physisorption-based processes the storage capacity at room temperature is too low. [3] Recently, also formic acid and methanol obtained from the reduction of carbon dioxide with molecular hydrogen have been studied as potential hydrogen storage materials. Since methanol and formic acid are liquid, they are easier to store, transport and handle, compared to H_2. [4] Besides, HCOOH is considered less hazardous than methanol, and therefore a valuable alternative in spite of its lower hydrogen density (43 vs. 125 g/kg). [5] Finally, in the methanol formation reaction, a mole of H_2 is lost by forming water, following the reaction:

$$CO_2 + 3H_2 \rightarrow CH_3OH + H_2O \qquad (6.1)$$

Nevertheless, the chemistry of CO_2 transformation is a challenge due to the presence of large energy barriers, requiring catalysis. The mainly used catalysts for the hydrogenation-dehydrogenation reactions are expensive homogeneous catalysts (Ru, Ir complexes) and heterogeneous catalyst based on noble metals (Pd, Au, Ag). As far as non-noble metals are concerned, only a few catalysts of this type (Fe, Cu based catalysts) are reported in the literature.

In this aim, in this chapter the study of heterogeneous Cu-based catalyst supported on SiO_2 is reported. This frame has been done in collaboration with Dr. Nicola Scotti and Dr. Nicoletta Ravasio from the Institute of Molecular Science and Technologies of CNR (CNR-INSTM Centre of Milan).

6.1 Hydrogenation of CO_2 to Formic Acid Reaction

The hydrogenation reaction of carbon dioxide to formic acid is given in Equation 6.2.

$$CO_2 + H_2 \rightarrow HCOOH \qquad (6.2)$$

The CO_2 hydrogenation to HCOOH is thermodynamically disfavoured ($\Delta G_{273\ K}$ = 32.9 kJ/mol). In order to shift the reaction to give the formic acid product, a base must be added to the reaction. In fact, in such conditions, the proton transfer to the base drives the reaction. In addition to the base, homogeneous or heterogeneous catalyst must be added to the CO_2 hydrogenation reaction. In this sense, transition metal-based homogeneous catalysts, such as Ru, Rh and Ir complexes, are used with good results for the synthesis of formic acid, primarily in terms of activity and selectivity. [6] The catalytic performance of some of the homogenous catalysts studied in the literature is shown in Table 6.1.

Catalyst Precursor	**Solvent**	**Add.**	**p_{H2}/ p_{CO2} [atm]**	**T [°C]**	**TON**	**TOF [h^{-1}]**	**Ref**
$RhCl(PPh_3)_3$	MeOH	PPh_3, NEt_3	20/40	25	2700	125	7
$Ru_2(CO)_5(dppm)_2$	acetone	NEt_3	38/38	25	207	207	8
$TpRu(PPh_3)(CH_3CN)H$	THF	NEt_3, H_2O	25/25	100	760	48	9
$TpRu(PPh_3)(CH_3CN)H$	CF_3CH_2OH	NEt_3	25/25	100	1815	113	10
$RuCl_2(PMe_3)_4$	Sc CO_2	NEt_3, H_2O	80/40	50	7200	153	11
$RuCl(OAc)(PMe_3)_4$	Sc CO_2	NEt_3 C_6F_5OH	70/120	50	31667	95000	12
(η^6-arene)Ru(oxinato)	H_2O	NEt_3	49/49	100	400	40	13
(η^6-arene)Ru(bis-NHC)	H_2O	KOH	20/20	200	2300	306	14
PNP–Ir(III)	H_2O	KOH, THF	29/29	120	3500000	73000	15
$NiCl_2(dcpe)$	DMSO	DBU	40/160	50	4400	20	16

Table 6.1. Hydrogenation of CO_2 to formic acid reaction catalyzed by transition metal-based homogeneous catalysts. TON= Turnover number; TOF= Turnover Frequency. [6]

Unfortunately, homogeneous catalysts present different limitations, as catalyst separation and recovery processes. For these reasons, this type of catalyst is not suitable for commercial applications. With this perspective, heterogeneous catalysts are preferable in terms of stability, separation, handling, recovery and reuse [17].

The first CO_2 hydrogenation reaction to produce formic acid by using a heterogeneous catalyst was carried out with Raney nichel under 200–400 bar H_2 pressure at 80-150 °C.[18] Later, only few publications on the carbon dioxide to form formic acid reaction by using heterogeneous catalysts were published. Furthermore, these literature studies concerned only expensive catalysts mainly based on noble metals, such as Au/TiO_2,[19] PdNi/ carbon nanotube-graphene [20] and Ir/SiO_2 catalysts. [21] Due to the large cost of these materials, new heterogeneous catalysts based on non noble metals should be tested. In the literature, copper-based catalysts have not been studied yet for the hydrogenation to formic acid reaction, but they are widely studied for other type of hydrogenation reactions. For example, copper-based systems are the most active catalysts for the CO_2 hydrogenation to methanol. In Table 6.2, the activity of some copper-based catalysts for this reaction is resumed.

Catalyst	**Preparation method**	**T [°C]**	**CO_2 conversion [%]**	**CH_3OH selectivity [%]**	**Ref**
$Cu/Zn/Ga/SiO_2$	co-impregnation	270	5.6	99.5	22
$Cu/Ga/ZnO$	co-impregnation	270	6.0	88.0	23
Cu/ZrO_2	deposition-precipitation	240	6.3	48.8	24
$Cu/Ga/ZrO_2$	deposition-precipitation	250	13.7	75.5	25
$Cu/B/ZrO_2$	deposition-precipitation	250	15.8	67.2	25
$Cu/Zn/ZrO_2$	coprecipitation	250	19.4	29.3	26
$Cu/Zn/ZrO_2$	urea-nitrate combustion	240	17.0	56.2	27
$Cu/Zn/Al/ZrO_2$	coprecipitation	240	18.7	47.2	28

Table 6.2. Hydrogenation of CO_2 to methanol reaction catalyzed by Cu-based homogeneous catalysts. [17]

With the aim of verifying whether copper-based catalysts can also be active for CO_2 hydrogenation reaction to formic acid, in the following paragraphs a preliminary study on heterogeneous copper-based catalyst supported on SiO_2 is reported.

6.2 Synthesis of Cu-based catalyst: Chemisorption-Hydrolysis Method

Metal oxides has been largely used as heterogeneous catalysts in different industrial processes. In order to increase the activity, nanosized particles of metal oxides dispersed onto inorganic matrixes has been widely considered in literature. First of all the reduction of particle size (*i.e.* the increase of the surface/volume ratio) allows to speed up the chemical reactions. In addition, both the reduction of the particle size and the interaction with the support heavily influence the electronic state of the metal oxide, affecting its reactivity.

Traditionally, co-precipitation or impregnation techniques are used to synthesize nanostructured materials supported on inorganic matrixes. These methods provide simple steps and the use of non expensive reagents, but lead to the formation of metal oxide low dispersed onto the matrix and with non homogeneous particle size distribution. Alternatively, chemical vapor deposition (CVD) method can be used. CVD technique leads to the formation of well dispersed catalyst, but require sophisticated apparatus and present a poor reproducibility. For these reasons is less applicable on industrial scale.

Recently an unconventional technique called chemisorption-hydrolysis (CH) has been reported in literature [29]. This methodology is characterized by the adsorption of $[Cu(NH_3)_4]^{2+}$ precursor on a support, followed by hydrolysis and calcination steps. In this method, copper oxides highly dispersed on different inorganic supports has been obtained in easy and reproducible way, with simple preparation steps and cheap precursors and apparatus. In addition, the high dispersion of the copper oxide obtained with this technique ensures an easy reduction with H_2 of the oxide phase to

metallic copper, which is the catalytically active phase in hydrogenation reactions. Moreover, the high dispersion of the copper oxide obtained with CH method gives acidic properties to the heterogeneous catalyst due to the presence of Lewis acid sites, even if the metal oxide (that in the bulk form presents basic behaviour) is supported over non acidic matrixes such as silica. In detail, the Lewis acidity is ascribed to the surface defectivity *(i.e.* coordinative insaturation) of the highly dispersed copper oxide phase, which presents distorted octahedral configuration. Finally, after reduction of the dispersed copper oxide, the acidity of the materials increases, due to further distortion into cuboctrahedral geometries. [31]

Therefore, the chemisorption-hydrolysis method offers the possibility to create a bifunctional heterogeneous catalyst, with both acidic and hydrogenation activity.

6.2.1 Catalyst Preparation

Cu-based catalysts were prepared by chemisorption−hydrolysis (CH) method. In particular, the siliceous support (Fluka, SSA = 413 m^2/g, PV = 0.75 mL/g) was added to a 0.7 M aqueous $[Cu(NH_3)_4]^{2+}$ solution, prepared by dropping NH_4OH to a $Cu(NO_3)_2 \cdot 3H_2O$ solution until pH 9 had been reached. After 20 min under stirring, the slurry, held in an ice bath at 0 °C, was slowly diluted with 3L of deionized water in order to allow the hydrolysis of the copper complex and the deposition of the copper oxide. Following, the solid was separated by filtration and washed with deionized water. Finally, the catalyst was dried overnight at 120 °C and calcined in air at 350 °C for 4h. [30] The sample obtained with this procedure is hereafter named CuO/SiO_2. Catalysts have been prepared by researchers of CNR-INSTM Centre of Milan.

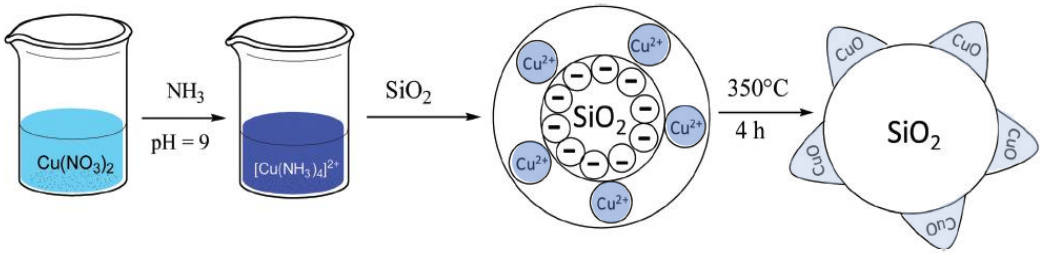

Figure 6.1 Schematic representation of copper oxide over silica formation by chemisorption method.

Also Cu-based catalysts containing amino groups grafted on the silica surface were prepared. In this case, before the chemisorption-hydrolysis procedure, the silica was functionalized with 3-aminopropyltriethoxysilane (APTS) following the grafting procedure described in Chapter 3. The idea is to test whether the amino groups can immobilize the carbon dioxide on the surface of the catalyst, thus favouring the hydrogenation reaction to formic acid. Furthermore, in this way the system become reusable and easily separable from the reaction mixture. The same C-H method used for the preparation of CuO/SiO_2 catalyst has been followed. However, in order to preserve amino-functionalities, the calcination step has been performed in air at 150°C for 4 h. The sample obtained with this procedure is hereafter named CuO/A_SiO_2.

6.3 Physico-chemical Characterization of Catalysts

6.3.1 Structural and Morphological Analysis

The structural properties of the prepared samples were studied by XRD analysis (Figure 6.2).

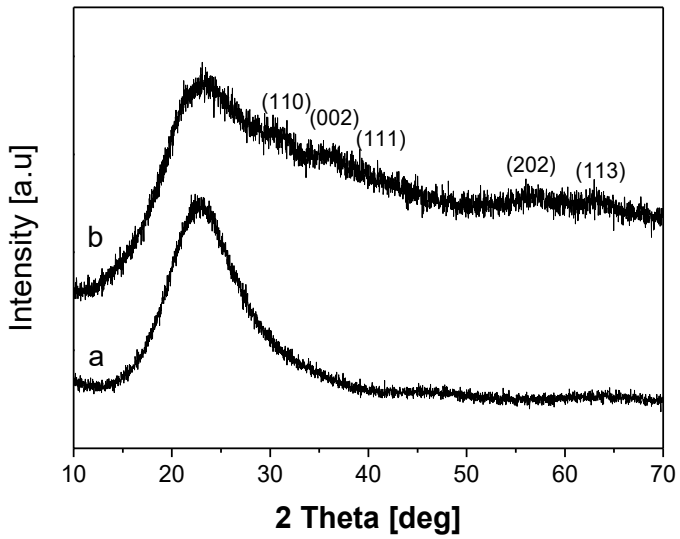

Figure 6.2. XRD pattern from 10 to 70 ° 2θ of pure SiO_2 (curve a) and CuO/SiO_2 (curve b) materials.

The XRD pattern of the pure silica (Figure 6.2, curve a) presents no significant reflections, confirming its amorphous structure. In the diffraction patterns of CuO/SiO_2 catalyst (curve b) very broad reflections at 21, 26, 38, 58 and 62 °2θ, corresponding to the planes (110), (002), (111), (202) and (113) respectively, are visible. These reflections are typical of CuO, while the very prominent broadness indicates the effective dispersion of copper oxide on the silica surface.[32] Furthermore, the broadness of the peaks can be due to the finely dispersion of the copper oxide on the silica.

In addition, the morphology of Cu-based catalysts was studied by using transmission electron microscopy (TEM). The obtained images are reported in Figure 6.3.

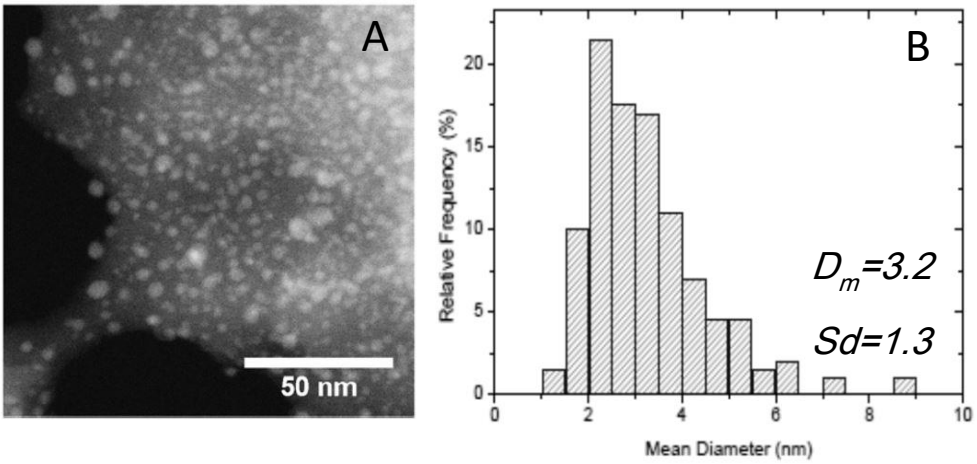

Figure 6.3. TEM analysis (Frame A) and size distribution (Frame B) of CuO/SiO_2 sample.

As we can see in Figure 6.3, in CuO/SiO_2 sample the copper oxide particles presents a very small size (the estimated mean particle size is about 3.2 nm) highly dispersed onto the silica support.

6.3.2 Surface Properties of Cu-based Materials

The presence of the organic chains grafted on CuO/SiO_2 sample was evaluated by FT-IR spectroscopy. Spectra of the samples before and after the functionalization are reported in Figure 6.4.

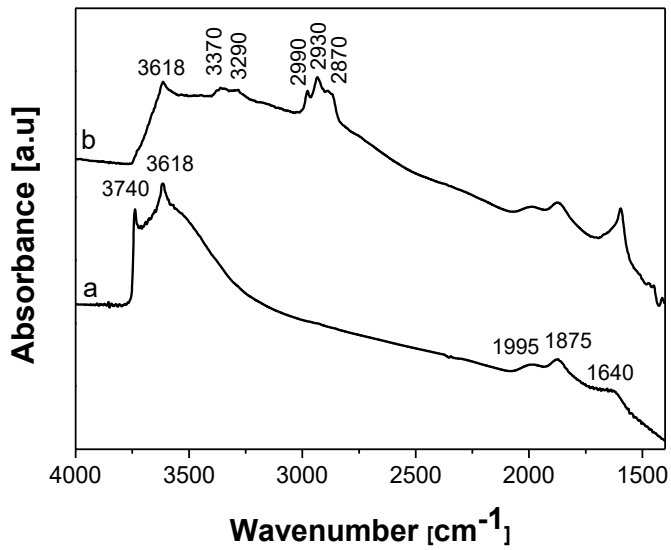

Figure 6.4. FT-IR spectra of CuO/SiO_2 (curve a) and CuO/A_SiO_2 (curve b) samples. Spectra were recorded after outgassing the samples at r.t. for 30 minutes.

In the high frequency range, the FT-IR spectrum of CuO/SiO_2 sample (Figure 6.4, curve a) is characterized by sharp band centred at 3740 cm^{-1} with a shoulder at 3715 cm^{-1}, due to the stretching mode of isolated SiOH groups, [33] and a broad band with a peak centred at 3618 cm^{-1}, attribute to the stretching mode of silanol species interacting each other through H-bond. [34]

After the grafting procedure with APTS (Figure 6.4, curve b), the bands due to surface silanol species appear strongly modified. In particular, the band at 3740 cm^{-1} disappears due to the condensation of silanol groups with the amino silane during the grafting procedure.

At lower frequencies, the FT-IR spectrum of grafted sample is characterized by the presence of bands at 3370 and 3290 cm^{-1}, due to the stretching modes of NH_2 functionalities, and absorptions located at 2990, 2930 and 2870 cm^{-1}, attributed to stretching modes of CH_2 groups of the silane. The associated scissoring mode of NH_2 groups is visible at 1592 cm^{-1}.

The amount of the organic species introduced with the grafting procedure (expressed in terms of nitrogen concentration) on CuO/A_SiO_2 is 1.2 mmol/g (as derived by elemental analysis)

6.4 Evaluation of the Copper Oxidation State

The amount of copper introduced in the sample has been evaluated by using ICP-QMS spectrometry and an external calibration methodology, after microwave digestion of catalyst in HNO_3. The values obtained are 11.6% and 13.3% for CuO/SiO_2 and CuO/A_SiO_2 samples, respectively.

In order to obtain a catalyst active for the hydrogenation reaction it is necessary that the copper dispersed on the silica support is in the metallic state. For this reason, before the catalytic test, the sample must be treated as follows. After heating at 200 °C in air for 20 min, the sample is put under rotary vacuum for 20 min, and then reduced in static at the same temperature with 1 atm of pure hydrogen. 3 H_2-vacuum cycles have been performed for an optimal reduction treatment.

In order to clarify if the catalyst is reduced to the optimum state, a study of the copper oxidation state has been carried out. One of the most used methods for this purpose is the adsorption of a probe molecule (in this case carbon monoxide) on the sample, followed by FT-IR Spectroscopy. Before the experiment, using a vacuum line connected to a FT-IR cell containing a self-supported pellet of the sample simulates the reducing treatment. In detail, the sample is put under vacuum and is heated until 200 °C for 30 min (heating ramp: 10°C/min). After, 100 mbar of H_2 is sent to the sample and kept in contact for 2 min. Following, the gas is evacuated, the sample is

kept in vacuum for 2 min, and the H_2-vacuum cycle is repeated for 3 times. During the last cycle, after the sending of the hydrogen, the sample is cooled to 150 °C (heating ramp 5 °C/min). Finally, the sample is put under vacuum and cooled to room temperature. In order to maximize the interaction between the CO molecule and the surface, the experiment is carried out at low temperature. For this reason, the sample is further cooled with liquid nitrogen, and kept at 77 K for all the experiment.
In Figure 6.5 is reported the FT-IR spectrum of the adsorbed CO on CuO/SiO_2 sample.

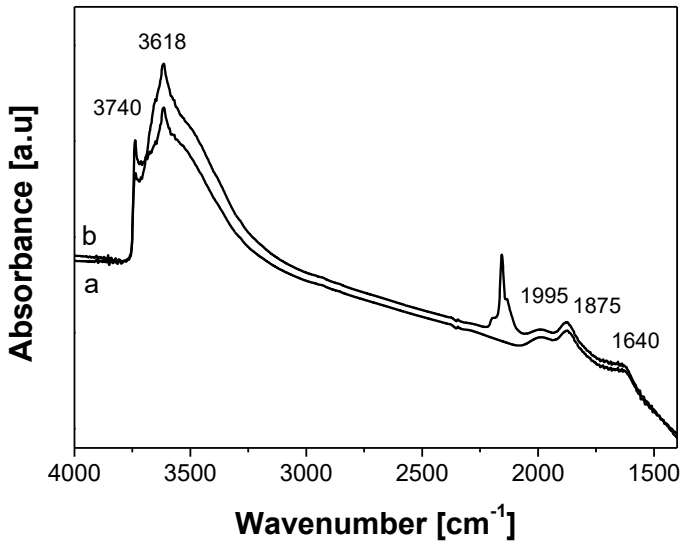

Figure 6.5. FT-IR Spectra of CuO/SiO_2 sample treated before (curve a) and after (curve b) the admission of CO at 77K (Pmax: 65 mbar).

After the CO admission, the FT-IR spectrum of CuO/SiO_2 sample appear strongly modified. In particular, changes both in high frequency region, due to the interaction of OH groups with the CO molecule, and in the low frequency region, due to the interaction of the CO molecule with the material, are present. In order to better appreciate the modifications due to the interaction with carbon monoxide, in Figure 6.6 are reported the difference spectra, obtained by subtracting the spectrum recorded

before the sending of CO to all the spectra recorded after the admission of the probe molecule. In this way, the bands grown after the interaction with the CO appear positive, while the decreased ones appear negative.

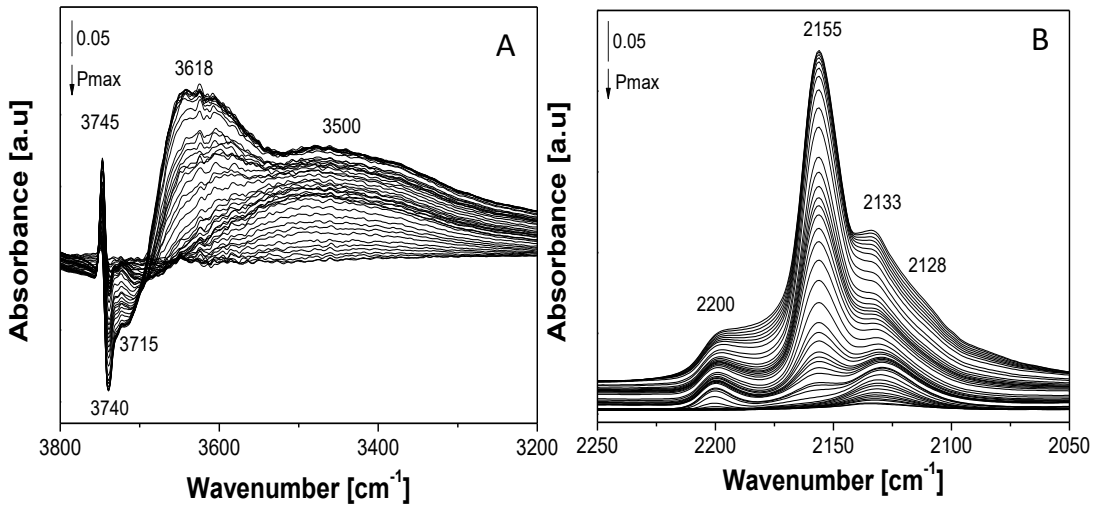

Figure 6.6. FT-IR Spectra of adsorbed CO at 77K (Pmax: 65 mbar) on CuO/SiO_2 sample treated at 200°C from 3800 and 3200 cm^{-1} (Frame A) and from 2250 and 2050 cm^{-1} (Frame B). The arrows indicate a decreasing of CO pressure. Spectra are reported after subtraction of the spectrum of the bare sample (before CO interaction).

In the high frequency region, the CO admission on CuO/SiO_2 sample (Figure 6.6, Frame A) results in the conversion of the original bands due to surface OH groups at 3740 and 3715 cm^{-1} (appearing as negative bands in the spectrum) into broader adsorptions centred at 3618 and 3500 cm^{-1}. These bands are due to the surface silanol groups interacting through H-bonding with the CO probe molecule.

In the lower frequency region (Figure 6.6, Frame B) a complex series of bands with maxima at 2200, 2155 and 2133 cm^{-1} are present. The band at 2200 cm^{-1} is due to the adsorption of CO on isolated Cu^{2+} ions, remained in the oxidized form despite the reduction with H_2.[34] The intense band at 2155 cm^{-1} is attribute to the CO H-bonded on the surface silanol groups of the support [35]. In addition, according to Hadjiivanov et al. [36] this band may also be due to CO adsorbed on Cu^{+} ions. Finally,

the complex adsorption with maximum at 2133 cm^{-1} is difficult to be assigned. In fact, adsorptions located in this region can be attribute both to Cu^{+}-CO carbonyls and Cu^{0}-CO species. [34] Since the spectral region of these two species overlap, in order to distinguish between both kind of complexes it is necessary to observe their stability. In fact, CO forms mainly a π- bond with Cu^{0} atoms; therefore, the resulting complexes are unstable, and can be easily decomposed during evacuation. Cu^{+} ions instead forms both σ and π- back bonds with carbon monoxide, and therefore Cu^{+}-CO complex is more stable.[34] In sight of this, we can observe that the band at 2133 cm^{-1} rapidly decreases intensity with evacuation, and therefore can be attribute to Cu^{0}-CO species. In addition, proceeding with desorption, a band located at 2128 cm^{-1} become visible. Since the band is stable upon evacuation, it should be attributed to the presence of Cu^{+}-CO complexes.

The same experiment has been repeated for CuO/A_SiO_2 sample. The obtained FT-IR spectra are reported in Figure 6.7.

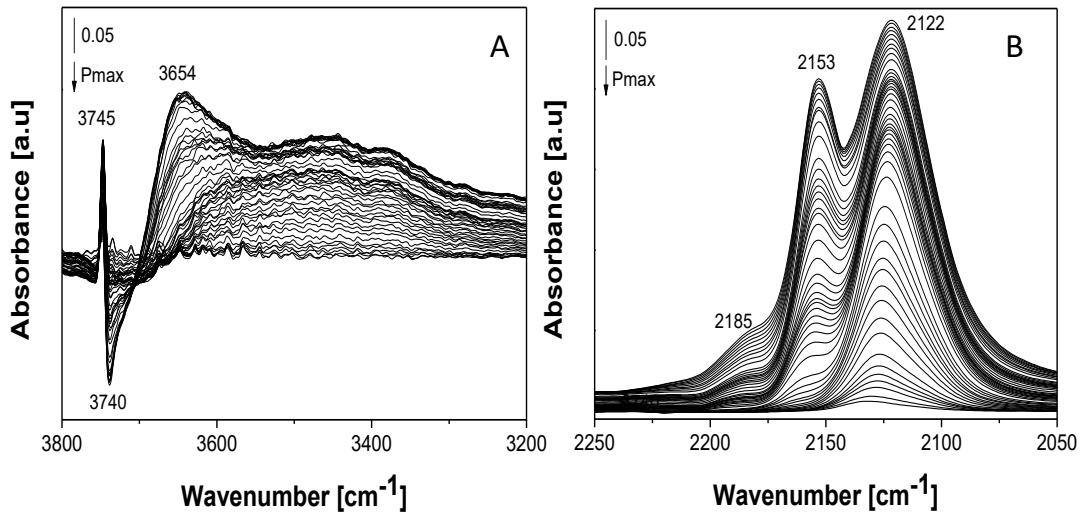

Figure 6.7. Difference FT-IR Spectra of adsorbed CO at 77K (Pmax: 65 mbar) on CuO/A_SiO_2 sample from 3800 and 3200 cm^{-1} (Frame A) and from 2250 and 2050 cm^{-1} (Frame B). The arrows indicate a decreasing of CO pressure.

At high frequencies (Figure 6.7, Frame A) the FT-IR spectra of CO adsorbed at 77 K on CuO/A_SiO_2 sample is characterized by the presence of the same bands already discussed for CuO/SiO_2 sample. Nevertheless, some differences in the IR spectra are visible at lower frequencies (Figure 6.7, Frame B). In this region, bands centred at 2185, 2153 and 2122 cm $^{-1}$ are present. The adsorption at 2185 cm^{-1}, due to the adsorption of CO on Cu^{2+} cations, is less intense compared to that observed for CuO/SiO_2 sample, and appears at lower wavenumbers. The band located at 2153 cm^{-1}, attribute to the CO interacting with the surface silanol groups or to the CO adsorbed on Cu^{+} ions is only slightly less intense compared to the parent sample. Finally, the absorption at 2122 cm^{-1} is much more narrow and intense than the one observed for the CuO/SiO_2 sample and appears at lower wavenumbers. In order to better appreciate the difference of the spectra recorded for the two samples, a direct comparison is reported in Figure 6.8.

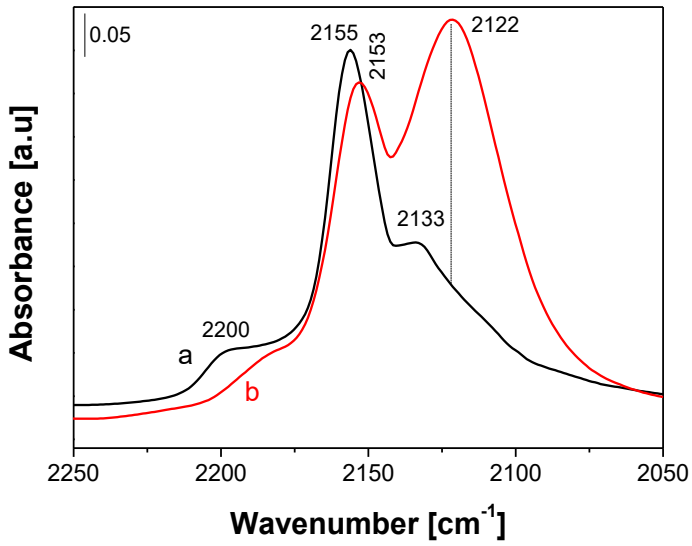

Figure 6.8. Difference FT-IR Spectra of 65 mbar of CO at 77K adsorbed on CuO/SiO_2 (curve a) and CuO/A_SiO_2 sample (curve b).

Considering the importance of the presence of Cu^0 in the catalysts for the hydrogenation reaction and the difficulties in the attribution of the band located at 2122 cm^{-1}, also FT-IR analysis of CO adsorbed at room temperature was performed. Difference spectra of CO adsorbed on CuO/A_SiO_2 at RT are shown in the Figure 6.9.

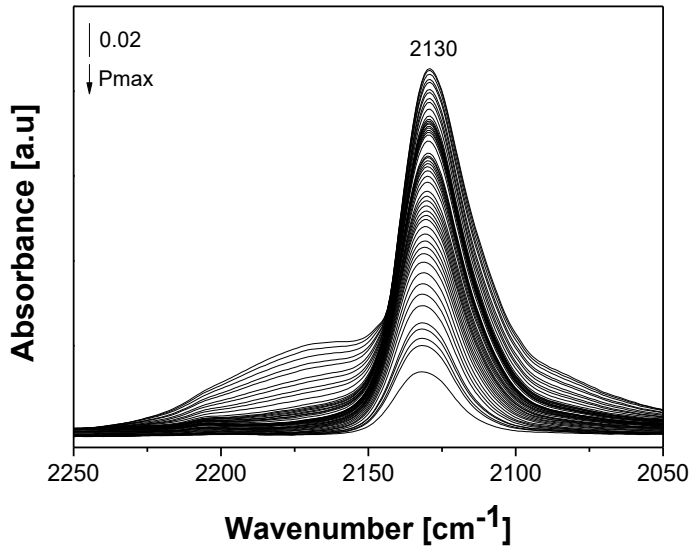

Figure 6.9. Difference FT-IR Spectra of 65 mbar of CO at RT adsorbed on CuO/A_SiO_2 sample. The arrows indicate a decreasing of CO pressure until vacuum.

After the admission of CO at room temperature, two main adsorptions are observable. The intense band at 2130 cm^{-1} is attribute to Cu^0. The intensity of this band drops substantially after evacuation but the band does not disappear completely.[12]

In addition, an adsorption between 2250 and 2150 cm^{-1} that vanish rapidly after evacuation is observable. This band can be attributed to carbonyls formed with Cu^{2+} cations, that continue to exist despite the reduction. [37]

6.5 CO_2 Hydrogenation: Experimental Results

The hydrogenation reaction has been tested using sodium hydrogen carbonate as CO_2 precursor. In a typical hydrogenation test, the pre-reduced catalyst (250 mg) and $NaHCO_3$ (4g) was stirred at 725 rpm in a glass reaction vessel under hydrogen (pressure: 50 bar) at 120°C.

The reaction mixture were then analyzed after 22 hours by HPLC and HNMR. A calibration line was performed in order to evaluate the amount of formic acid and in the case of HNMR using CH_3CN as internal standard.

Data obtained from the catalytic test, performed by researchers of CNR-INSTM Centre of Milan, are reported in Table 6.3.

Catalyst	Amount of Catalyst [mg]	$T_{treatment}$ [°C]	Selectivity [%]	Y [%]
CuO/SiO_2	250	200	100	3.5
CuO/A_SiO_2	250	200	100	5.1
CuO/SiO_2	250	270	100	8.4
CuO/SiO_2	500	270	100	19.0

Table 6.3. Selectivity and yield of CuO/SiO_2 and CuO/A_SiO_2 catalysts.

From data reported in Table 6.3 it can be seen that the hydrogenation reaction to formic acid occurs with a high selectivity (100% for both samples). Unfortunately, the obtained yields are low. In addition, the amino groups contained in CuO/A_SiO_2 sample seems to only slightly improve the performances of the catalyst (5.1%, compared to 3.5% of CuO/SiO_2 catalyst). A possible reason for such low yield can be found in the low catalyst reduction temperature (200°C). Unfortunately, a higher temperature can not be used for CuO/A_SiO_2 sample, as it contains amino groups that begin to degrade at 220 °C, as observed by thermogravimetric analysis (data not shown for sake of brevity).

Another reason could be related to the formation of a strong interaction between Cu and N that reduces the available active sites, besides having a negligible effect on the reaction.

Nevertheless, considering CuO/_SiO_2 sample, by increasing the temperature to 270 °C, the yield of the catalyst increases up to 8.4% for the test with 250 mg of catalyst and 19% for the optimized test (performed with 500 mg of catalyst). These results are promising and suggest that such catalysts should be more thoroughly studied in the future for the hydrogenation reaction of CO_2 to formic acid.

6.6 Conclusions

In this Chapter, the synthesis, characterization and catalytic activity of Cu-based catalyst supported on SiO_2 have been reported. The chemisorption-hydrolysis method was used to synthesize copper oxide dispersed on a silica matrix. This technique allowed the formation of nanosized CuO particle highly dispersed on the silica support, as it can be clearly seen from TEM analysis. The obtaining of such widely dispersed nanoparticles on the silica support is of great importance, because it increases the catalytic performances.

Furthermore, the oxidation state of copper in the supported catalysts has been investigated by using FT-IR spectroscopy with the adsorption of CO probe molecule. These analyses showed that, after the reduction procedure, Cu^0 has been formed, even if a small portion of unreduced Cu^{2+} is still observable. However, FT-IR analyzes showed that the reduction treatment is effective in the formation of copper in the oxidation state necessary for the catalytic hydrogenation of CO_2.

Finally, the catalytic activity of these samples for the hydrogenation reaction of carbon dioxide to formic acid has been tested. All catalysts showed a high selectivity (100%), even if the yield of the reaction is low: 3.5 and 5.1% for CuO/SiO_2 and CuO/A_SiO_2 sample, respectively. However, by optimizing the reaction conditions

(*i.e.* temperature of the treatment and amount of catalyst), by using CuO/SiO_2 catalyst a promising yield of 19% was also obtained.

Further studies will be required to increase the yield of this reaction using copper-based catalysts. It would be interesting to project a catalyst with different supports, characterized for example by higher specific surface area to favour an even higher dispersion of copper nanoparticles.

References

[1] A.Taheri, *Int. J. Energy Res*., **2013**, 37, 485-499.

[2] A. Boddien, B. Loges, F. Gartner, C. Torborg, K. Fumino, H. Junge, R. Ludwig and M. Beller, *J. Am. Chem. Soc*., **2010**, 132, 8924.

[3] S. Enthaler, J. von Langermann and T. Schmidt, *Energy Environ. Sci*., **2010**, 3, 1207–1217.

[4] B. Loges, A. Boddien, F. Gärtner, H. Junge and M. Beller, *Top. Catal*., **2010**, 53, 902.

[5] Y. Yang, M. G. White and P. Liu, *J. Phys. Chem. C*, **2012**, 116, 248.

[6] P. Upadhyay and Vivek Srivastava, *De Gruiter*, **2016**, 10, 2.

[7] N. N. Ezhova, N. V. Kolesnichenko, A. V. Bulygin, E. V. Slivinskii and S. Han, *Russ. Chem. Bull*., **2002**, 51, 2165-2169.

[8] Y. Gao, J. K. Kuncheria, H. A. Jenkins, R. J. Puddephatt and G. P. A. Yap, , *Dalton Trans*., **2000**, 3212–3217.

[9] C. Q. Yin, Z. T. Xu, S. Y. Yang, S. M. Ng, K. Y. Wong, Z. Y. Lin and C. P. Lau, *Organometallics*, **2001**, 20, 1216–1222.

[10] S. M. Ng, C. Q. Yin, C. H. Yeung, T. C. Chan and C. P. Lau, Eur. *J. Inorg. Chem.*, **2004**, 1788–1793.

[11] P. G. Jessop, Y. Hsiao, T. Ikariya and R. Noyori, *J. Am. Chem. Soc.*, **1996**, 118, 344–355.

[12 P. Munshi, A. D. Main, J. C. Linehan, C. C. Tai and P. G. Jessop, *J. Am. Chem. Soc.*, **2002**, 124, 7963–7971.

[13] T. T. Thai, B. Therrien and G. Suss-Fink, *J. Organomet. Chem.*, **2009**, 694, 3973–3981.

[14] S. Sanz, A. Azua and E. Peris, *Dalton Trans*., **2010**, 39, 6339–6343.

[15] R. Tanaka, M. Yamashita and K. Nozaki, *J. Am. Chem. Soc*., **2009**, 131, 14168–14169.

[16] C. C. Tai, T. Chang, B. Roller and P. G. Jessop, *Inorg. Chem*., **2003**, 42, 7340–7341.

[17] W. Wang, S. Wang, X. Ma X. and J. Gong, *Chem. Soc. Rev*., **2011**, 40, 3703–3727.

[18] M. W. Farlow and H. Adkins, *J. Am. Chem. Soc*., **1935**, 57, 2222– 2223.

[19] D. Preti, C. Resta, S. Squarcialupi and G. Fachinetti, *Angew. Chem., Int. Ed.*, **2011**, 50, 12551–12554.

[20] L. T. M. Nguyen, H. Park, M. Banu, J. Y. Kim, D. H. Youn, G. Magesh, W.Y. Kim and J. S. Lee, *RSC Adv*., **2015**, 5, 105560–105566.

[21] Z. Xu, N. D. McNamara, G. T. Neumann, W. F. Schneider and J. C. Hicks, *ChemCatChem*, **2013**, 5, 1769–1771.

[22] J. Toyir, P. R. de la Piscina, J. L. G. Fierro and N. Homs, *Appl. Catal., B*, **2001**, 29, 207–215.

[23] J. Toyir, P. Ramırez de la Piscina, J. L. G. Fierro and N. Homs, *Appl. Catal., B*, **2001**, 34, 255–266.

[24] J. Liu, J. Shi, D. He, Q. Zhang, X. Wu, Y. Liang and Q. Zhu, *Appl. Catal., A*, **2001**, 218, 113–119.

[25] X. M. Liu, G. Q. Lu and Z. F. Yan, *Appl. Catal., A*, **2005**, 279, 241–245.

[26] R. Raudaskoski, M. V. Niemela and R. L. Keiski, *Top. Catal*., **2007**, 45, 57–60.

[27] X. M. Guo, D. S. Mao, S. Wang, G. S. Wu and G. Z. Lu, *Catal. Commun*., **2009**, 10, 1661–1664.

[28] X. An, J. L. Li, Y. Z. Zuo, Q. Zhang, D. Z. Wang and J. F. Wang, *Catal. Lett*., **2007**, 118, 264–269.

[29] N. Scotti, D. Monticelli, F. Zaccheria, *Inorganica Chemica Acta*, **2012**, 380, 194-200.

[30] F. Zaccheria, N. Scotti, M. Marelli, R. Psaro, N. Ravasio, *Dalton Trans.*, **2013**, 42, 1319.

[31] N. Scotti, M. Dangate, A. Gervasini, C. Evangelisti, N. Ravasio, F. Zaccheria, *ACS Catal*., **2014,** 4, 2818-2826.

[32] M. Suleiman, M. Mousa, A.I.A. Hussein, 2015, *J. Mater. Environ. Sci*., **2015**, 6, 7, 1924-1937.

[33] F. Cucinotta, F.Carniato, G. Paul, S. Bracco, C. Bisio, S. Caldarelli, L. Marchese, *Chem. Mater*., **2011**, 23, 11, 2803-2809.

[34] L. Etgar, G. Schuchardt, D. Costenaro, F. Carniato, C. Bisio, S.M. Zakeeruddin, M.K. Nazeeruddin, L. Marchese, M. Graetzel, *J. Mater. Chem. A*, **2013**, 1, 10142-10147.

[35] G. J. Millar and C. H. Rochester, *J. Chem. Soc. Faraday Trans*., **1991**, 87, 9, 1467-1472.

[36] K. Hadjiivanov, T. Venkov and H. Knözinger, *Catalysis Letters*, **2001**, 75, 1–2.

[37] K. Hadjiivanov and G. N. Vayssilov, *Adv. Catal*., **2002**, 47, 307-511.

Chapter 7

General Conclusions

This PhD thesis was devoted to the preparation and characterization of hybrid organic inorganic materials to be used as solid sorbent for the CO_2 capture. Various families of solids with different structure, morphology, size and organic component were optimized to this purpose.

In the first part of the PhD, in order to give additional insights on the understanding of processes between organically modified silica surface and CO_2, SBA-15 silicas functionalized with silanes containing different amounts of amino groups (*i.e.* 3-aminopropyltriethoxysilane (APTS), 3-(2-aminoethyl)aminopropyltrimethoxysilane (EAPTS) and 3-[2-(2-aminoethyl)aminoethyl]aminopropyltrimethoxysilane (PAPTS)) were considered.

First of all, the obtained materials were characterized by using a multidisciplinary approach, in order to clarify their physico-chemical properties. In particular, the interactions between $–NH_2$ groups of the organic component and the surface silanols have been evaluated by analyzing the mobility of the chains. This is a relevant parameter that can strongly influence the CO_2 adsorption performances. For this purpose, a combination of experimental and computational approach were here adopted for the first time. ^{1}H Hahn echo MAS NMR spectroscopy revealed that in A-SBA-15 and P-SBA-15 samples similar amount of mobile and rigid components are present, while in E-SBA-15 sample only rigid components are visible. This behaviour suggests that probably in the EAPTS- grafted sample an interaction between the amino groups and the silanols more intensive with respect to A-SBA-15 and P-SBA-15 materials is present. This behaviour is explained by ab initio calculations, in which optimized models of the three organo-silanes on silica clusters

were analyzed. In these models, APTS chain interacts slightly with the surface and moves freely, as well as PAPTS chain when the density of the grafted silanes around it is high enough. On the contrary, EAPTS chain is stretched on the silica surface as it is involved in H-bond with the silanol groups that limit its mobility.

Afterwards, the carbon dioxide adsorption process on these materials was studied by using a multidisciplinary approach. Both qualitative (*i.e.* FT-IR and SS-NMR spectroscopies) and quantitative techniques (*i.e.* volumetric analysis and ZLC chromatography) were adopted. In particular, the CO_2 adsorption capacity values obtained by volumetric analysis are 0.18, 0.49 and 0.62 mol/kg, while those obtained with ZLC are 0.21, 0.44 and 0.53 mol/kg, respectively for A-SBA-15, E-SBA-15 and P-SBA-15. In both techniques, the same sequence of CO_2 adsorption is respected, following the order P-SBA-15 > E-SBA-15 > A-SBA-15. These results suggest that, by increasing the number of amino groups in the chain, the adsorption of carbon dioxide is favoured. This effect may be attribute to the occurrence, when more than one amino group is present, of intramolecular mechanism (in addition to the intermolecular one), which contributes to the increase of the amount of adsorbed CO_2.

After evaluating the effect of the organic chain in the hybrid materials, the influence of the siliceous support on the CO_2 adsorption process was studied. In this regard, silica-based materials with different morphology, structure and particle size were selected. Different aspects fundamental for the comprehension of the carbon dioxide adsorption process have been investigated.

As first, MCM-41-based materials with different particle size, passing from micrometric to nanometric scale, were considered, in order to assess the size effect of the support on the CO_2 adsorption. This is the first time in which MCM-41 silica with nanometric size is used as solid support for carbon dioxide capture.

After a physico-chemical characterization of the materials, aimed to the determination of the morphological, structural and surface properties of the samples, the study of the carbon dioxide adsorption process was performed. Firstly, this study

was focused on distinction between physisorption and chemisorption processes by coupling FT-IR and SS-NMR spectroscopies. The study of these two different adsorption processes is crucial in order to understand the operation of these hybrid organic-inorganic materials during the CO_2 adsorption. It was observed that higher amount of physisorbed CO_2 is present in nanometric sample with respect to the micrometric one. This effect is probably due to the higher pore accessibility, related to the higher pore volume, in the micrometric sample. Subsequently, the amount of adsorbed carbon dioxide on hybrid MCM-41 materials was determined by using three different techniques: TGA, ZLC and volumetric analysis. The obtained CO_2 adsorption capacity values are 0.79 and 0.58 mol/kg (TGA), 0.64 and 0.51 mol/kg (ZLC) and 0.79 and 0.62 mol/kg (volumetric analysis), respectively for P_MCM-41 nano and P_MCM-41 micro samples. These analyzes suggest that by reducing the size of MCM-41 silica, increases the amount of adsorbed carbon dioxide by the hybrid material. This effect can be explained by the huge contribution of physical adsorption in the nanosized sample, as already observed by qualitative techniques.

Moreover, the temperature dependence of MCM-41 based hybrid materials has been studied by analyzing the carbon dioxide adsorption process at different temperatures (from 20 °C to 90 °C). Only few papers concerning the evaluation of the temperature dependence of hybrid siliceous materials are present in literature, and they have never been thoroughly investigated by using a multidisciplinary approach. In this thesis it was observed that, for both MCM-41 based samples, the amount of adsorbed carbon dioxide decreases if the temperature is increased. This effect can be attribute to the fact that the products resulting from the reaction between CO_2 and $–NH_2$ groups (*i.e.* carbamate and carbamic acid) are thermally unstable, and thus release CO_2 if heated. However, such products are more stable in the micrometric sample with respect to those in the nanosized one. This effect should be due to a greater protection effect caused by the pores.

Afterwards, it was decided to select the Stöber silica as support, characterised by a low porosity degree, essentially due to aggregation phenomena. This is the first time

in which a non porous siliceous material has been investigated as solid sorbent for the CO_2 capture. The use of this type of silica is, however, interesting for real technological applications due to economic factors: during the synthesis of Stöber silica, in fact, no expensive templates are used, and therefore the final cost is lower compared to the widely used mesoporous silica. The carbon dioxide adsorption properties of the organo-modified Stöber silica sample were analyzed by the use of different techniques. First of all, FTIR and SS-NMR spectroscopies were used to study both physisorption and chemisorption processes occurring by contacting CO_2 and the functionalized sample. These analyzes showed that a huge amount of physisorbed carbon dioxide is present in the Stöber-based hybrid material, whereas a close to zero amount of physisorbed CO_2 is observable for the bare Stöber sample. Such behaviour indicates that is the aggregation porosity modified by the presence of PAPTS that is the responsible of the high amount of physisorbed CO_2.

Moreover, a comparison between the organo-modified Stöber sample with an ordered porous material (based on MCM-41 silica) allowed to evaluate the effect of the support porosity on the CO_2 adsorption properties.

From this comparison, obtained by coupling FTIR and SS-NMR spectroscopies, it was highlighted that a greater amount of physisorbed CO_2 is observable for the Stöber-based material with respect to the MCM-41-based one, probably due to the higher pore accessibility. Viceversa, the chemisorbed component is present in greater amount in the ordered mesoporous sample, probably due to the highest amount of PAPTS chains grafted in this material.

Furthermore, in order to verify which material adsorbs higher amount of CO_2, quantitative TGA and ZLC techniques were performed. The obtained CO_2 adsorption capacity values are 0.49 and 0.58 mol/kg (TGA) and 0.40 and 0.51 mol/kg (ZLC), respectively for P_ Stöber and P_MCM-41 samples. These data revealed that, as expected, the MCM-41 based material is more efficient compared to the Stöber-based one. However, since the difference in the adsorption capacity is not large, and

that the Stöber-based sample is considerably cheaper, the non-porous sample should be considered an interesting adsorbent material for the carbon dioxide capture.

Concluding this section, the material that was proved to be the best adsorbent is P_MCM-41 nano, with a CO_2 adsorption capacity value of 0.79 mol/kg at 35°C and 0.96 mol/kg at 20°C (data obtained by using TGA analysis). These values are promising for potential applications in CCS field. Furthermore, in this sample the amount of CO_2 irreversibly bonded after the evacuation is low (9.3% at 35°C), and is easily removed after heating. Even this parameter is fundamental for potential real applications, as it suggests that this material is easily regenerable for a new adsorption cycle.

Moreover, from the comparison between TGA, ZLC and volumetric analysis it emerged that these techniques provide consistent and comparable results. In particular, it has been proved that the ZLC analysis is a reliable system comparable to the most common used techniques (such as volumetry), with the advantages of shorter times of analysis and the use of smaller amount of sample.

After the study of some solid adsorbents usable in the CO_2 capture phase, the attention was shifted on a subsequent phase of CCS process that is the use of carbon dioxide for the synthesis of more useful products. In particular, heterogeneous copper-based silica materials were studied as catalysts for the hydrogenation reaction of carbon dioxide to formic acid. The catalysts mainly used for the hydrogenation-dehydrogenation reactions reported in literature are expensive homogeneous catalysts (Ru, Ir complexes) and heterogeneous catalyst based on noble metals (Pd, Au, Ag). However, the use of catalysts based on non-noble metals such as copper, preferable for economic factors, are rarely reported in literature.

The characterization of the copper-based catalysts was addressed in particular to the determination the copper dispersion on the silica matrix and the revelation of the copper oxidation state. More in detail, TEM anlaysis revealed that the oxidic phase is nanosized and is highly dispersed on the silica support. Furthermore, FT-IR spectroscopy with the adsorption of CO probe molecule allowed the determination

of the copper oxidation state in the catalysts. These analyses showed that in the catalyst, after the reduction treatment, copper is present in the oxidation state proper for the catalytic CO_2 hydrogenation (*i.e.* Cu^0).

Finally, the catalytic activity of these samples for the hydrogenation reaction of CO_2 to formic acid has been tested. After an optimization of the reaction conditions (*i.e.* treatment temperature and amount of catalyst), CuO/SiO_2 catalyst showed a promising yield of 19% (and 100% of selectivity).

List of Publications

1. Chiara Vittoni, Vittoria Sacchetto, Daniele Costenaro, Simone Mastroianni, Andreas Hinsch, Leonardo Marchese and Chiara Bisio, *"Gelation of solvent-free electrolyte using siliceous materials with different size and porosity for applications in dye sensitized solar cells"*, Solar Energy, 124 (2016), 101-113.

2. Giorgio Gatti, Daniele Costenaro, Chiara Vittoni, Geo Paul, Valentina Crocellà, Enzo Mangano, Stefano Brandani, Silvia Bordiga, Maurizio Cossi, Chiara Bisio and Leonardo Marchese, "*CO_2 adsorption on different organo-modified SBA-15 silicas: a multidisciplinary study on the effects of basic surface groups*", PCCP, 19 (2017), 14114-14128.

3. Giorgio Gatti, Chiara Vittoni, Daniele Costenaro, Geo Paul, Enzo Mangano, Stefano Brandani, Leonardo Marchese and Chiara Bisio, *"The influence of particle size of amino-functionalized MCM-41 silicas on CO_2 adsorption"*, PCCP, 19 (2017), 29449 – 29460.

Acknowledgements

As always at the end of a stage of life, many episodes come to mind, and with them all the people involved in. I would like to thank here the most important for me.

I would like to start with my Supervisor, *Prof. Leonardo Marchese*, who gave me the opportunity to work on this challenging project, and especially my co-Supervisor, *Dr. Chiara Bisio*, who has always followed me step by step all these years, well before the beginning of this PhD period. Your advices and encouragements were (and are) really important for me.

I would also like to thank all the (current and past) members of the Physical Chemistry group: *Dr. Giorgio Gatti, Dr. Geo Paul, Dr. Fabio Carniato, Dr. Vittoria Sacchetto, Dr. Mina Errahali, Ms. Diana Francia Olivas Olivera, Prof. Enrica Gianotti, Dr. Ivana Miletto, Miss. Chiara Ivaldi, Mr. Federico Begni, Mr. Stefano Marchesi, Dr. Marta Corno, Prof. Maurizio Cossi, Dr. Alberto Fraccarollo* and *Dr. Lorenzo Canti*; all of you have taught me something, and I am very grateful. In particular, how to forget *Dr. Daniele Costenaro*, with whom I worked side by side for a long time: I will bring all your teachings and advices (working and not only…) always with me. Or *Dr. Bianca Martins Estevao*, with which a friendship that crosses the ocean was born. Finally, to complete this group, I would like to thank *Miss. Chiara Zaccone*, and *Miss. Marta Rivello*, that worked with me on this project.

I would also like to thank *Dr. Enzo Mangano, Prof. Stefano Brandani, Dr. Arran Gibson, Dr. Maria-Chiara Ferrari* and *all the members of Carbon Capture group* from University of Edinburgh's School of Engineering. Thank you very much for your hospitality and the precious teachings.

Thanks also to all my office colleagues, and in particular to *Miss. Valentina Toson*, with whom I share the achievement of this important goal (we have done it!).

To conclude the "working" section I would like to thank the PRIN project that financed this work and the people I have worked with: *Prof. Silvia Bordiga*, *Dr. Valentina Crocellà*, *Dr. Nicoletta Ravasio* and *Dr. Nicola Scotti*.

I would like to thank *my Family* and *my Parents*, who have always supported me in all my choices. Without you I would not have achieved this goal.

And last, but obviously not least, I would like to thank *Lorenzo*, to which this thesis is devoted. Two lines will never be able to explain the encouragement, support, and love that you give me every single day. But I wish you know that without all this I would never be here. In my master degree thesis I wrote "I know that together we will be able to realize all of our dreams". We just realized some of them, now we have to proceed on the road together.

Appendix

Instrumental Parameters

1. *X-Rays Diffraction (XRD) Analysis*

   X-ray diffractrograms (XRD) were collected on unoriented ground powders using a Thermo ARL 'XTRA-048 diffractometer with a CuKα (λ = 1.54 Å) radiation.

   Diffractograms of SBA-15 and related hybrid samples were recorded at r.t between 2° and 65° 2θ degrees with a step size of 0.02° and a rate of 1° 2θ/min.

   Diffractograms of MCM-41 silica and related hybrid samples were recorded at r.t. between 1.5° and 7° 2θ degrees with a step size of 0.02° and a rate of 1° 2θ/min.

   Diffractograms of copper based silica catalysts were recorded at r.t. between 10° and 70° 2θ degrees with a rate of 0.2° 2θ/min.

2. *High-Resolution Transmission Electron Microscopy (HRTEM)*

   HRTEM micrographs of adsorbent materials were recorded on a JEOL 3010-UHR microscope, operating at 300 kV. Before the analysis, samples were ultrasonically dispersed in isopropanol and a drop of the suspension was deposited on a copper grid covered with a lacey carbon film.

   HRTEM analysis of copper catalyst was operated at 200 kV with a LIBRA 200FE analytical transmission electron microscope, equipped with FEG source and purchased from Zeiss. Samples were deposited on holeycarbon-coated grids from alcohol suspensions. Samples, in the form of powders, were ultrasonically

dispersed in isopropyl alcohol, and a drop of the suspension was deposited on a holeycarbon film grid (300 mesh).

3. *N_2 Physisorption Analysis*

   Nitrogen measurements were carried out at 77 K in the relative pressure range from 10^{-7} to $1p/p_0$ by using a Quantachrome Autosorb iQ2 instrument. Before the analysis, the samples were outgassed at 150 °C for 3 h (residual pressure $p_0 10^{-6}$ Torr). Specific surface area values were determined by using the Brunauer-Emmett-Teller equation, in the residual pressure range from 0.01 to $0.1p/p_0$. Pore size distributions were obtained by applying the Non Localized Density Functional Theory (NLDFT) method (N_2 silica kernel based on a cylindrical pore model).

4. *Elemental Analysis*

   C–H–N elemental contents were determined using an EA 3000 elemental analyser (EuroVector). Helium and oxygen at 120 and 35 kPa pressures were used, respectively. For each material, three measurements were done.

5. *Inductively Coupled Plasma (ICP) Analysis*

   Copper metal loadings were determined by ICP-OES (ICAP6300 Duo purchased from Thermo Fisher Scientific) and an external calibration methodology, after microwave digestion of the samples (*ca.* 10 mg of catalyst) in 3 mL of aqua regia and dilution with highly deionized water (Milli-Q Academic, Millipore) to a final weight of 100 g.

6. *Thermogravimetric analysis (TGA)*

   For the determination of the silanol concentration a Setaram Setsys instrument was used. A sample of about 10-15 mg was packed in an alumina crucible, which was counterbalanced by an identical empty crucible.

The measurements were done under Argon flow (20 ml min^{-1}) from 20 to 1100 °C (1 °C min^{-1} heating rate).

CO_2 adsorption measurements were carried out on a Setaram Sensys Evo TG/DSC apparatus. Typically, for these experiments, a sample mass of ca. 20–30 mg was packed in a platinum crucible, which was counterbalanced by an identical platinum crucible packed with an equivalent mass of lead beads. Prior the measurements the sample was pretreated at 135 °C for 3 h (2 °C min^{-1} heating rate) under Helium flow (50 ml min^{-1}). The sample was then cooled to the desired temperature of the experiment (20, 35, 50, 70 and 90 °C) and the adsorption was performed by exposing the sample to a mixture of 10 vol% of CO_2 in He at a constant total flow rate of 50 ml min^{-1} for 2 h.

At the end of the adsorption step the inlet flow is then switched to pure He at the same flow rate for 2 h to allow the desorption of CO_2.

7. *Infrared Spectroscopy*

Infrared spectra were collected on a Thermo Electron Corporation FT Nicolet 5700 Spectrometer (resolution 4 cm^{-1}) and on an Equinox 55 Spectrometer (Bruker) (resolution 4 cm^{-1}). Self-supporting pellets were placed into a homemade IR cell with KBr windows permanently attached to vacuum line (residual pressure o $1\text{-}10^{-4}$ mbar), allowing all treatments and adsorption–desorption experiments to be carried out *in situ*. The cell is also equipped with a heating system that allows the sample to be kept at a specific temperature during analysis.

Before the CO_2 adsorption tests, the silica samples were outgassed at 135 °C with a heating ramp of 5 °C min^{-1} for 3 h; an oil-free apparatus and a grease-free vacuum line were used. The samples were cooled at room temperature for the collection of IR spectra upon CO_2 adsorption.

The study of the copper oxidation state in the catalysts was performed through the adsorption of carbon monoxide as a probe molecule on the sample, followed

by FT-IR Spectroscopy. Before the experiment, the reducing treatment is simulated as follows. Firstly, the sample is put under vacuum and is heated until 200 °C for 30 min (heating ramp: 10°C/min). After, 100 mbar of H_2 is sent to the sample and kept in contact for 2 min. Following, the gas is evacuated, the sample is kept in vacuum for 2 min, and the H_2-vacuum cycle is repeated for 3 times. During the last cycle, after the sending of the hydrogen, the sample is cooled to 150 °C (heating ramp 5 °C/min). Finally the sample is put under vacuum and cooled to room temperature. In order to maximize the interaction between the CO molecule and the surface, the experiment is carried out at low temperature. For this reason, the sample is further cooled with liquid nitrogen, and kept at 77 K for all the experiment.

All the spectra were normalized by dividing the density of the self-standing pellets, obtained by dividing the sample mass for the area of the pellets. In addition, the proper normalization of the IR spectra was verified taking as reference the intensity of the overtones and combination modes of the silica framework (bands in the 2200-1600 cm^{-1} range). As a consequence of the normalization, the absorbance values are reported as the arbitrary unit (a.u.).

8. Solid state NMR (SS-NMR) Spectroscopy

SS-NMR spectra were acquired on a Bruker Avance III 500 spectrometer and a wide bore 11.7 Tesla magnet with operational frequencies for ^{1}H, ^{29}Si and ^{13}C of 500.13, 99.35 and 125.77 MHz, respectively. A 4 mm triple resonance probe with MAS was employed in all the experiments. The samples were packed on a Zirconia rotor and spun at a MAS rate in the 0-15 kHz range. The magnitudes of radio frequency fields, υ_{rf}, were 62.5 and 33.3 kHz for ^{13}C and ^{29}Si, respectively. The relaxation delays, d1, between accumulations were 2.5, 100 and 180 s for ^{1}H, ^{13}C and ^{29}Si MAS NMR, respectively. For the $^{13}C\{^{1}H\}$ CPMAS experiments, the radio frequency fields υ_{rfH} of 55 and 28 kHz were used for initial excitation and decoupling, respectively. During the CP period the ^{1}H RF field υ_{rfH} was

ramped using 100 increments, whereas the ^{13}C RF field υ_{rfC} was maintained at a constant level. During the acquisition, the protons are decoupled from the carbons by using a TPPM decoupling scheme. A moderate ramped RF field υ_{rfH} of 62 kHz was used for spin locking, while the carbon RF field υ_{rfC} was matched to obtain the optimal signal and the CP contact time of 2 ms was used. The rotor synchronized Hahn echo sequence (p/2–t–p–t–acquisition) was also applied to record the ^{1}H NMR spectra with a t delay time of 6700 ms and a 901 pulse length of 2.5 ms. All chemical shifts are reported using the d scale and are externally referenced to TMS at 0 ppm. Before the gas adsorption tests, the silica samples were outgassed at 135 °C with a heating ramp of 5 °C min^{-1} for 3 h; an oil-free apparatus and a grease-free vacuum line were used. The samples were cooled at room temperature and 60 mbar of $^{13}CO_2$ was placed in contact with the samples and then kept at that atmosphere for at least 2 days. After that the rotor was packed in a glove box and submitted for solid state NMR experiments. The label $^{13}CO_2$ was used in order to increase the signal intensity.

9. *The Zero Length Column (ZLC) chromatography*

The Zero Length Column consists of a 1/800 Swagelok union in which a very small amount of sample (10–15 mg) is placed as monolayers between two sister discs. The experiment is based on following the desorption curve of a sample previously equilibrated with a known mixture at a constant flow rate. For the characterization of adsorbents for post-combustion capture the feed mixture is composed of 10% CO_2 in He. Once the equilibrium is reached the inlet flow to the ZLC is switched to pure He (carrier) and the desorption starts. The system is equipped with drying columns to ensure the removal of any traces of water from the gases entering the system. The concentration of the gas phase is monitored using a Dycor Ametek Benchtop quadrupole mass spectrometer connected to the outlet of the ZLC. Prior to each experiment the samples were regenerated overnight at 150 °C under He flow. Each experiment was carried out at two

different flow rates, 2 and 2.7 mL min^{-1}, to check if the samples are in equilibrium or kinetically controlled. To ensure that complete equilibrium was achieved the ZLC experiment was repeated at increasing adsorption times. The system was considered to be in equilibrium when the CO_2 uptake did not change any more with the adsorption time.

10. Theoretical Calculations

Theoretical calculations have been performed using the Gaussian09 program at the Density Functional Theory (DFT) level, with the hybrid functional B3LYP29–31 using Dunning's correlation-consistent cc-PVDZ basis set on light atoms, and LANL2DZ effective core potentials and the basis set for silicon. The atom–atom pairwise algorithm proposed by Grimme35 and implemented in Gaussian09 was used to estimate the contribution from dispersion (van der Waals) forces to energies and geometrical structures.

The silica surface was simulated by two cluster models, with Si39O112H68 (I) and Si52O152H92 (II) stoichiometry: the models have a surface of approximately 2.5 and 4 nm^2, respectively; hydrogen atoms were added to saturate the oxygen valences at the cluster border and on the ''external'' surface. These clusters were extracted from the large model of amorphous silica optimized in the literature, dealing with MCM-14 modeling: though MCM-14 and SBA-15 differ for the mesoscopic structure (*i.e.* mesopore size and channel topology) at this scale the atomistic structures of their inner surfaces are fully comparable. The silanol concentration on the model surfaces, a crucial parameter to describe the interactions with the attached molecules, was set to 5 SiOH nm^{-2}, to reproduce the experimental measures described below. To simulate the functionalized surfaces, one to three molecules of APTS, EAPTS and PAPTS were grafted to cluster I and II surfaces by eliminating three water molecules from silanol groups, and thus forming three Si–O–Si bonds per chain; when more

than one molecule was added, a homogeneous distribution of chains attached to the surface was assumed.

UNIVERSITÀ DEL PIEMONTE ORIENTALE

DIPARTIMENTO DI
SCIENZE ED INNOVAZIONE TECNOLOGICA

Viale Teresa Michel, 11 – 15121 Alessandria AL

DECLARATION AND AUTHORISATION
TO ANTIPLAGIARISM DETECTION

The undersigned Vittoni Chiara student of Chemistry&Biology Ph.D. course (XXX Cicle)

declares:

- to be aware that the University has adopted a web-based service to detect plagiarism through a software system called "Turnitin"
- his/her Ph.D. thesis was submitted to Turnitin scan and reasonably it resulted an original document, which correctly cites the literature

acknowledges:

- his/her Ph.D. thesis can be verified by his/her Ph.D. tutor and/or Ph.D Coordinator in order to confirm its originality.

Date: 14/11/2017 Signature: Chiara Vittoni